UCLA
UCLA Electronic Theses and Dissertations

Title
Catalyst Mediated Growth and Optical Properties of Group III-V Nanowires: Au catalyzed GaAs and Self-catalyzed InP

Permalink
https://escholarship.org/uc/item/6q76k7k0

Author
Park, Jeung Hun

Publication Date
2013

Peer reviewed|Thesis/dissertation

eScholarship.org Powered by the California Digital Library
University of California

UNIVERSITY OF CALIFORNIA

Los Angeles

Catalyst Mediated Growth and Optical Properties of Group III-V Nanowires: Au catalyzed GaAs and Self-catalyzed InP

A dissertation submitted in partial satisfaction of the

requirements for the degree Doctor of Philosophy

in Materials Science and Engineering

by

Jeung Hun Park

2013

© Copyright by

Jeung Hun Park

2013

ABSTRACT OF THE DISSERTATION

Catalyst Mediated Growth and Optical Properties of

Group III-V Nanowires: Au catalyzed GaAs and Self-catalyzed InP

by

Jeung Hun Park

Doctor of Philosophy in Materials Science and Engineering

University of California, Los Angeles, 2013

Professor Suneel K. Kodambaka, Committee Chair

In this work, the first half will cover gold catalyzed gallium arsenide nanowire growth *via* vapor-liquid-solid (VLS) process using molecular beam epitaxy (MBE). And, the second half will discuss self-catalytic growth of indium phosphide nanostructures *via* either VLS or vapor epitaxy process using metal organic vapor phase epitxay (MOVPE).

Part I: Au Catalyzed Growth of GaAs Nanowires

The correlation between prepatterned catalyst films and GaAs nanowire growth was studied, using Au/GaAs as a model system, for the identification of the initial growth conditions on nanowire densities. GaAs nanowires are preferentially grown at 490 ^{o}C using solid-source molecular beam epitaxy *via* VLS process with e-beam patterned Au dots as catalysts. The

resulting nanowire morphologies and the fractional surface densities are determined as a function of the electron beam dose, dot size, and inter-dot spacing using scanning electron microscopy. We report the micro Raman studies of Au catalyzed GaAs nanowire bundles. Strong dependence of Raman spectra shift on the nanowire bundles are attributed to structural defects, residual stress, aspect ratio, spatial density and random growth orientation, resulting from variations of catalyst thickness and pattern size. The surface optical phonon modes of GaAs nanowires are also systematically investigated using micro Raman spectroscopy as a function of the fill factor and average diameter.

Part II: Self-Catalyzed Growth of InP Nanostructures

We report the effect of morphology of nanostructures on optical properties. Self-catalyzed InP nanostructures (nanocones, nanopillars) were grown on both indium phosphide (111)B and silicon (100), (111) single crystal substrates using MOVPE. Micro Raman scattering experiment was employed to understand the effect of morphology and substrate on the optical properties of as-grown structures. Due to crystal symmetry breaking in one-dimensional nanostructures, three phonon vibration modes (LO, TO, SO) were clearly resolved. Their broadening and downshift of Raman spectra were found to be morphology dependent (*i.e.* surface-to-volume ratio and crystal plane size). The LO phonon was found to depend on surface-to-volume ratio of nanostructures, implying that high scattering volume and surface electric fields with defect density leads to enhancing LO phonon excitation in InP nanocones.

The dissertation of Jeung Hun Park is approved.

____

King-Ning Tu

____

Kang L. Wang

____

Suneel K. Kodambaka, Committee Chair

University of California, Los Angeles

2013

This dissertation is dedicated to my wife and family.

TABLE OF CONTENTS

List of Figures		vii
List of Tables		xiv
Acknowledgments		xv
Vita		xvii
CHAPTER 1	Introduction	1
	References	8
CHAPTER 2	Experimental Methods	12
	References	35
CHAPTER 3	Effect of Electron Beam Lithography Pattering Parameters on the Au-Catalyzed Growth of GaAs Nanowire on GaAs(111)B Substrate	37
	References	52
CHAPTER 4	Raman Spectroscopic Studies on Semiconductor GaAs Nanowire Bundles	55
	References	66
CHAPTER 5	Density and Diameter Dependent Surface Optical Phonon Mode Changes in GaAs Nanowire Arrays	69
	References	82
CHAPTER 6	Raman Scattering in Self-Catalyzed InP Nanostructure: Morphology and Substrate Effects	84
	References	105
CHAPTER 7	Multi Phonon Raman Scattering in Self-Catalyzed InP/InAs/InAs Nanopillars and Nanocones	108
	References	122
CHAPTER 8	Summary and Future Work	125

LIST OF FIGURES

Figure 1.1	A schematic drawing of Vapor-Liquid-Solid process.	7
Figure 1.2	A schematic drawing of self-catalyzed nanowire growth.	7
Figure 2.1	A schematic of the experimental apparatus.	25
Figure 2.2	Top: A schematic drawing of a generic MBE system, Bottom: Veeco GEN II MBE, installed at the Northrop Grumman Space Technology, Redondo Beach, CA.	26
Figure 2.3	Pictures of the Emcore D125 MOVPE system installed at UCLA. Top: The front of the system showing the reactor chamber and loadlock chamber; Bottom: the back of the system showing the metalorganic sources (in constant temperature baths) and the gas flow manifold.	27
Figure 2.4	The Raman Scattering Process and corresponding Feynman's diagram.	28
Figure 2.5	Raman effect in the energy level. In Stokes processes, the final state is above (left), in anti-Stokes process it is below the initial state (right).	28
Figure 2.6	(a) Phonon dispersion at the Brillouin zone center of ZB GaAs, (b) Schematic representation of phonon dispersion of WZ GaAs as a result of the one folding of the ZB dispersion relation along $\Gamma \rightarrow L$, (c) Phonon dispersion of ZB InP, (d) Schematic representation of phonon dispersion of WZ InP as a result of phonon folding from ZB along [111] to the WZ along [0001] phase.	29

Figure 2.7	A schematic illustration of absorption and radiative and non-radiative emission from an electronically excited atom.	30
Figure 2.8	An illustration of photoluminescence (a) in a bulk semiconductor and (b) in a quantum well. A single PL peak is expected for the bulk material, whereas satellite peaks are expected for the quantum well.	31
Figure 2.9	Schematic of electron scattering process, showing emission of secondary electrons, backscattered electrons, characteristic x-rays, and cathodoluminescence.	32
Figure 2.10	A schematic diagram showing the point where the electron beam strikes the sample. The three major electron beam parameters are probe diameter, d_{probe}, probe current, i_{probe}, and probe convergence, $\alpha_{probe.}$	32
Figure 2.11	Pictures of a Hitachi S4700 Scanning Electron Microscope (left) and FEI Nova 600 SEM/FIB (right).	33
Figure 2.12	Transmission Electron Microscope - FEI Titan S/TEM (left) and JEOL 1200EX (right).	33
Figure 3.1	Schematic overview of patterns on GaAs(111)B wafer. Each of the 31 patterns labeled alphabetically from A to AE consists of 6 rectangular regions made up of 250 × 150 ordered arrays of a given dot-size *D* (= 100 and 150 nm) and inter-dot spacing *S* (= 100, 150, and 250 nm).	45
Figure 3.2	Effect of electron beam dose *Q* on the patterned dot profiles. Top-view field-emission SEM images acquired from a GaAs(111)B wafer patterned using EBL with dots of size *D* = 100 nm and inter-dot spacing *S* = 150 nm as a function of *Q* = a) 220 μC/cm^2,	46

b) 295 μC/cm^2, c) 460 μC/cm^2, and d) 535 μC/cm^2. Scale bar in all the images is 500 nm. The plot shows spatial variations in the SEM image intensities of the patterns in a)-d) normalized with respect to the back ground intensity. Each of the curves is an average of over 128 line profiles acquired from the patterned regions.

Figure 3.3 3 (a) 30°-tilted SEM image of a GaAs nanowire grown in the area containing Au dots of size D = 150 nm, and spacing S = 150 nm patterned using Q = 505 μC/cm^2. (b) Top view SEM image of the same nanowire. (c) Bright-field TEM image of a GaAs nanowire grown in the area prepared using Q = 525 μC/cm^2, D = 150 nm, and S = 150 nm. Inset is a selected area electron diffraction pattern acquired along the [112] zone axis from the region highlighted in the image. The diffraction data indicates that the wire is zinc blende in structure and the growth direction is ⟨111⟩. (d,e) Higher resolution TEM images of the catalyst tip-wire interface and GaAs nanowire, respectively. 48

Figure 3.4 Top-view SEM image obtained from the patterned GaAs(111)B wafer after the growth of GaAs nanowires. a) Low-magnification SEM image of the region containing the pattern prepared using Q = 355 μC/cm^2, highlighted by red square. The scale bar is 0.5 mm. (b) Higher magnification SEM image of the red rectangular region in (a). (c,d) SEM images of the areas patterned using Q = (c) 400 μC/cm^2 and (d) 520 μC/cm^2. In the images (b)-(d), scale bar is 50 μm. All the dots in a given row have the same size D = 150 nm (top row) and 100 nm (bottom row), while S is 100 nm, 150, and 250 nm in the left, center, and the right patterns, respectively. 49

Figure 3.5 SEM images of a GaAs(111)B wafer with GaAs nanowires grown in the areas patterned with Au dots of size D = 100 nm. The 50

vertical and horizontal axes show patterns obtained using different Q and S values, respectively. Scale bars in the images are 4 μm.

Figure 3.6 The fractional surface density of nanowires plotted as a function of (a) Q and (b) D and S. Solid lines are a guide for the eye. 51

Figure 4.1 SEM images of the Au patterned GaAs (111)B substrates with e-beam dose (a) 220 μC/cm^2, (b) 295 μC/cm^2, and (c) 535 μC/cm^2. 61

Figure 4.2 (a) Surface coverage and (b) average base diameter changes of GaAs nanowire bundles as a function of electron beam dose. 62

Figure 4.3 Transmission Electron Microscope - FEI Titan S/TEM (left) and JEOL 1200EX (right). 63

Figure 4.4 Raman spectra of GaAs nanowire bundles as a function of electron beam dose for the pattering size of (a) 100 nm and (b) 150 nm. 64

Figure 4.5 Intensity changes of (a) transverse optical and (b) longitudinal optical phonon modes as a function of electron-beam dose for 100 nm & 150 nm patterns. 65

Figure 5.1 Figure 5.1 SEM micrographs of the GaAs nanowire samples as a function of electron beam dose. 75

Figure 5.2 Variation of the fill factor of GaAs nanowires as a function of e-beam dose. 76

Figure 5.3 Raman spectra for different e-beam doses from 175 μC/cm^2 to 565 μC/cm^2. 77

Figure 5.4 Frequency of the SO mode as a function of nanowire diameter for various surrounding media (i.e. $\varepsilon_m^{air} = 1$). The full red squares 78

correspond to the experimental SO mode observation.

Figure 5.5	Frequency of the different phonon modes obtained within the effective dielectric function approximation with the experiment results. Full red squares correspond to the SO mode.	79
Figure 5.S1	Au catalyst layer patterning condition on GaAs(111)B wafer	80
Figure 5.S2	Surface Phonon Frequency as a function of electron beam dose.	80
Figure 5.S3	SO phonon calculation of GaAs nanowires using Dielectric Continuum Model.	81
Figure 6.1	Scanning Electron Micrographs of self-catalyzed InP nanostructures grown on InP(111)B substrate. Top view: (a) InP nanopillar on InP(111)B, (b) InP nanocone on InP(111)B. Tilted view with 40 degree: (c) InP nanopillar on InP(111)B, (d) InP nanocone on InP(111)B.	95
Figure 6.2	Raman spectra of InP nanostructures grown on InP(111)B substrate. The laser with wavelength of 513.6 nm excitation was used as the excitation source.	96
Figure 6.3	Scanning Electron Micrographs of self-catalyzed InP nanostructures grown on silicon single crystal substrate. Top view: (a) InP nanopillar on Si(111), (b) InP nanocone on Si(111), (c) InP nanocone on Si(100). Tilted view with 40 degree: (d) InP nanopillar on Si(111), (e) InP nanocone on Si(111), (f) InP nanocone on Si(100).	97
Figure 6.4	Raman spectra of self-catalyzed InP nanostructures grown on Si(111) and Si(100) substrates.	98
Figure 6.5	Raman spectra of (a) InP(111)B single crystal substrate, (b) self-	99

catalyzed InP nanopillars grown on InP(111)B, (c) self-catalyzed InP nanocones grown on InP(111)B.

Figure 6.6 Raman spectra of (a) InP(111)B single crystal substrate, (b) self-catalyzed InP nanopillars grown on Si(111), (c) self-catalyzed InP nanocones grown on Si(111). 100

Figure 6.7 Raman scattering spectra of InP nanocones on Si(111) substrate as a function of laser out-put power. 101

Figure 6.S1 High temperature deposition of InP nanostructure, exhibiting preferred lateral growth to vertical growth. 102

Figure 6.S2 (a) Bright field image of homogeneous InP nanocones grown on InP(111)B with electron diffraction pattern of the wire viewed along the $[\bar{1}12]$ axis. (b) High resolution transmission electron micrograph of InP nanocones with electron diffraction pattern viewed along $[011]_{WZ}$ and $[2\bar{1}\bar{1}0]_{ZB}$ axis. 103

Figure 6.S3 (a) SEM image of randomly oriented InP nanowires grown on Si(100) substrate, (b) the corresponding a Raman spectrum. 104

Figure 7.1 SEM images of top view (upper row) and 45 degree tilted view (lower row) of InP nanopillars, InP/InAs/InP nanopillars, and InP/InAs/InP nanocones grown on (111)B oriented InP single crystal wafer. 116

Figure 7.2 Raman spectra of (a) InP(111)B crystal, (b) InAs(111)B crystal, (c) InP nanopillar, (d) InP/InAs/InP nanopillar, and (e) InP/InAs/InP nanocones. The green dot lines are corresponded to InAs E_1(TO, ZB), InAs A_1(TO, WZ), InAs E_1(LO, ZB), InP E_1(TO, ZB), InP E_1(LO, ZB), InP E_1(2TO, ZB), InP E_1(TO+LO, 117

ZB), and InP E_1(2LO, ZB) in sequence. ZB and WZ denote zinc blende and wurtzite crystal structure, respectively.

Figure 7.3 Effect of substrate tilting on Raman spectra of InP/InAs/InP nanocones. 118

Figure 7.4 An excitation power dependence on Raman spectra of InP 1TO and InP 1LO peaks for different substrate tilts; (a) InP/InAs/InP nanopillars, (b) InP/InAs/In nanocones. (c) Integrated intensity ratio of InP 1TO over InP 1LO excitations 119

Figure 7.S1 S1 Power spectral density dependence of (a) InP/InAs/InP nanopillar, (b) the nanopillar with 30 degree tilt, (c) InP/InAs/InP nanocone, and (d) the nanocone with 30 degree tilt. 121

LIST OF TABLES

Table 2.I Raman active phonon modes for GaAs and InP Nanowires in this work 34

Table 6.I Summary of average InP nanostructure dimensions. Note: Length of InP NCs grown on Si (100) sample is only measured for 15 individual wires due to geometrical limitation with random orientations. 94

Table 6.II Raman vibration modes of InP nanostructures and Si bulk substrate 94

Table 7.I Raman vibration modes of InP and InAs nanowire in the literature 112

ACKNOWLEDGEMENTS

First of all, I would like to give my sincere gratitude to my advisor, Professor Suneel Kodambaka, for his guidance and supervision. He did support me not only on my research but also support me to explore many opportunities. As my advisor and colleague, I was able to learn plethora of valuables assets from him on attitudes as a scientist and a positive view of life during my stay in Ph.D. program. I also gratefully acknowledge Professors King N. Tu and Kang L. Wang for being member of my final dissertation committee and Professor Yu Huang for being my prospectus committee member.

I would like to express my special thanks to Drs. Marta Pozuelo and Sergey Prikhodko for TEM training, Dr. Robyn L. Woo for MOCVD training, Drs. Richard S. Kim, Choong-heui Chung and Vincent Gambin for their valuable discussions on spectroscopic measurement, and Dr. KyeongSik Shin for training electron beam lithography and nanodevice fabrication. I am thankful to Ms. Bunga Setiawan and Chilan Ngo for their helps in InP nanowire growth. Special thanks should go to Dr. Frances Ross for her support and enthusiasm for research and wealth of knowledge during my stay in IBM T.J. Watson Research Center. I am also grateful to Drs. Daechul Choi, Jung Kyu Han, and Yi-Chia Chou and Mr. Hyungsuk Kim for spending many years with their extensive supports and comments in my life at UCLA and IBM. Above all, I would like to thank to my family. Without their continuous support and unlimited love, I could not finish this long journey over 6 years. The completion of this document and the research therein would not have been possible without their support.

Finally, I would like to acknowledge financial supports for the works presented in this dissertation were provided by from the UC Discovery - Northrop Grumman Space Technology,

the NSF through the grant CMMI-0926412, Samsung Electronics Global Research Outreach Program, and LG Display Co. Ltd.

VITA

EDUCATION AND TRAINING

Pusan National University, Korea	Physics	B. S.	2003
Pusan National University, Korea	Physics	M.S. Program	2004

RESEARCH AND PROFESSIONAL EXPERIENCE

2011-Present Visiting Research Scientist at
IBM T.J. Watson Research Center, Yorktown Heights, NY, USA

2011-2012 Staff Research Associate at University of California – Los Angeles,
Los Angeles, CA, USA

2006-2011 Graduate Research Assistant at University of California – Los Angeles,
Los Angeles, CA, USA

2004-2006 Research Scientist at Crystal Bank (SRC), Busan, and
Pohang Accelerator Laboratory, Pohang, Republic of Korea

2004-2007 Research Scientist at Optoelectronics Research Laboratory,
Pusan National University, Busan, Republic of Korea

2001-2002 Visiting Research Student at Academia Sinica, Taipei, Republic of China

1999-2001 System Programmer, Military Service – HQ, 3rd Army, Republic of Korea

CHAPTER 1

INTRODUCTION

1.1 Overview

Nanowires are typically crystalline, one-dimensional (1D) high aspect ratio structures. In the recent years, nanowires of semiconducting materials have gained interest owing to their potential for applications in nanoelectronics, optoelectronics, and sensors [1,2,3]. Many research groups have demonstrated the fabrication of single nanowire based devices and their applicability. Large-scale integration of these single devices is a challenging task which involves precise control over synthesis and placement of individual nanowires with desired shape, structure, and orientation. One of the promising approaches to achieve this goal and in designing more complex structures, such as branched [4,5] or compositionally modulated [6] wires, is via 'bottom-up' approach, *i.e.* by self-organized assembly of atoms and molecules into desired nanostructures. Progress in this area requires a clear understanding of the mechanisms governing nucleation and growth of nanowires.

1.2 Vapor-Liquid-Solid Process

Nanowires are most commonly grown via the vapor-liquid-solid (VLS) process [7]. The schematics of the VLS growth mechanism are shown in Fig. 1.1. VLS process, first proposed in the early 1960s, involves a metal particle which forms a low-melting eutectic alloy with the material deposited from the vapor. This liquid alloy acts as a catalyst for preferential incorporation of the material. Under conditions where the incoming material gets deposited at the liquid-solid interface, 1D growth occurs in the form of cylindrical pillars or 'nanowires' with

wire diameter and length determined by the droplet size and deposition rate, respectively. Despite 40 years of research on the growth and characterization of nanowires, very little is known concerning the processes controlling the nanostructural and morphological evolution, even for relatively simple elemental materials such as Si [8] and Ge [9]. For more complex compounds such as group III-V semiconducting nanowires, most of the growth-related issues are not well understood.

1.3. Au Assisted Group III-V Nanowires Growth

III-V nanowires, such as GaAs, InAs, GaP, and InP, owing to their high carrier mobilities and low band gaps, form an important class of materials with potential applications in nanoelectronics and optoelectronics [10,11,12]. Most of the existing literature on III-V nanowires indicates that the as-grown materials are inherently defective due to the presence of twins or stacking faults perpendicular to the growth direction [13,14,15,16]. Controlling the growth orientation and defect density is crucial for better device performance, for example in vertical field effect transistors. However, this is a difficult task and has not yet been achieved.

Metal-organic chemical vapor deposition (MOCVD), metal-organic vapor phase epitaxy (MOVPE), and chemical beam epitaxy (CBE) are the most common techniques employed to grow III-V wires. Relatively fewer studies have used solid source molecular beam epitaxy (MBE) to grow these wires [17,18]. In most of the experiments, Au is used as the catalyst for nanowire growth. However, nanowire growth has also been observed in the absence of Au catalyst either due to the catalytic action of the group III metal [19,20] or due to the presence of a thin film of SiO_x [21,22]. In this work, the studies of the crystal structure and optical properties of GaAs nanowires will be presented throughout the Chapters 3-5.

1.4 Self-Catalyzed Group III-V Nanowire Growth

Indium phosphide and its related alloys are important materials for wireless communications, high-speed electronics, opto-electronics, and solid-state lasers [16-19]. For InP nanostructure growth, gold was dominant catalyst in VLS growth mechanism but it has serious disadvantages. Gold traps electrons and holes in nanowires and poses a serious contamination problem for nanoelectronic devices [23]. Despite of existing literatures of non-gold catalyst assisted growth [24,25,26], either the growth requires high growth temperature or the catalyst are not compatible with the conventional Si processing technology [23].

The alternative method for growing nanowire is the self-catalyst VLS growth mechanism where the group III metal acts as a self catalyzed deposition. Typically, the self-catalyst method is significant for vertical and uniform growth nanowire [27]. Taking into consideration of technological compatibility, much more attractive catalyst materials would be low-melting metals such as In or Ga. In this work, indium phosphide nanowires are synthesized by an In-assisted VLS growth process using MOVPE. A schematic growth process of self-catalyzed nanowire is shown in Fig. 1.2. Indium nanodroplets form by diffusion and coarsening of In adatoms on the surface of InP(111)B substrate or silicon substrate. By gathering P from the vapor phase these droplets acts as the seeds of the InP nanowire nucleation and growth. The axial growth rate of InP nanowires can be controlled by the partial pressure of TBP and TMIn as well as substrate temperature.

The performance of devices based on these materials, i.e. InAsP/InP, is affected in a major way by interface sharpness [28]. The interface sharpness, in turn, is determined by the surface roughness of the epitaxial layer during MOVPE. The most important factors influencing

surface roughness is the transport of the precursors through the boundary layer coupled with the heterogeneous chemical reactions [29]. The homo- or hetero-epitaxial growth of defect-free indium phosphide nanowires in the MOVPE environment requires close attention from the beginning to the end of the process. The substrate orientation, surface cleanliness, thermal treatment prior to the growth, and the growth conditions are key factors in achieving defect-free InP nanowires growth. Ex-situ and noninvasive characterizations of the wires are necessary in improving the growth process to obtain defect-free materials. Among the different characterization techniques, the structural, morphological characterization by electron microscopy technique, and optoelectronic responses measured by micro Raman spectroscopy have been chosen as the best characterization tools to determine the quality of the wires. In Chapter 6-8, a study is presented of the crystal structure and optical properties of InP nanowires.

1.5 Challenges of group III-V nanowire growth

Catalyst assisted III-V wire growth using gas precursors has been relatively well studied and the growth mechanisms are fairly well understood [30,31,32,33,34,35]. There are, however, several aspects of wire growth that are not yet clear. For example,

1) Au-catalyzed III-V wire growth does not occur above the bulk eutectic temperature. Best wire morphologies are achieved at low growth temperatures [14,32,33,34,35,36]. Here, the state of the catalyst is not known and the topic is controversial with speculations including both growth in presence of a liquid catalyst stabilized by nanoscale size effects and via vapor-solid-solid (VSS) process using a solid catalyst [37].

2) Majority of the nanowires are observed to grow along 111-B and are composed of rotational twins or stacking faults. (In III-V materials, 111 orientation is polar and the notation A and B

denote group III- and V-terminated surfaces, respectively.) Crystal structure of nanowires is found to be material-dependent. GaAs and InAs nanowires exhibit hexagonal wurtzite structure while GaP and InP nanowires are cubic zinc blende [38]. The origin of these defects is not known and hence large-scale control of the defect density or fabrication of defect-free structures has not yet been achieved.

3) Wires that grow along other orientations (111-A, 110, and 100) are defect free [19,30,39,40,41,42]. However, the number density of these wires is very low and/or procedures that yield these orientations are not well understood. For example, InP nanowires grow along 111 on pre-annealed Au-covered InP(001) substrates, while they grow along 100 on substrates that were not annealed [30,31]. Since the mechanisms underlying this behavior are not clear, further progress in optimizing the growth conditions for large-scale synthesis of high quality wires is lacking.

4) In majority of the Au-catalyzed nanowire growth experiments, Au is deposited either in the form of a thin film or as nanoclusters onto a substrate and air-transferred to the growth system. The exact composition of the substrates (Si, III-Vs) prior to growth is not well characterized. Hence the effects of oxygen, hydrogen, and other species on the nucleation and growth of nanowires are not known.

5) The free-standing III-V nanowires were grown by epitaxial techniques [17,18,35,39,42,40]. If the dimension of the nanowire is smaller than the mean free path of an electron, the electron may travel across the nanowire without scattering, resulting in ballistic transport of electrons [43]. Moreover, if the diameter of the nanowire can be reduced to a value comparable to the electron wavelength, quantum sub-bands should form [44]. A change in the band structure will affect the wavelength of the emitted light, suggesting that one may tune the wavelength by changing the

diameter of the wire. However, the effects of the size, shape, and crystal structure of these materials on their electrical and optical properties are not well characterized.

1.6 The Scope and Objectives

The objectives of the dissertation are grouped into the two main categories: the growth of GaAs and InP nanostructures, and electro-optical characterization of as-grown nanostructures. In the first part, it concerns about the catalyst effects (Au and In) on group III-V nanostructure growth (GaAs, InP) using solid state molecular beam epitaxy technique and metal-organic vapor phase epitaxy. Afterwards, the main focus is put on the characterization of group III-V nanostructures by micro Raman spectroscopy in order to gain a deeper understanding of the growth parameter effects on electro-optical properties of the nanostructure growth during the vapor-liquid-solid process.

This thesis is organized in the following way. In the first chapter, theoretical and practical backgrounds for this work are reviewed with a special attention for the growth of nanowires. The second chapter is dedicated to the experimental setup for nanowire growth and characterization. The third chapter focuses on the growth of GaAs nanowire and its density control using SS-MBE via the VLS process. The fourth chapter focuses on electro-optical properties in MBE grown GaAs nanowires. In the fifth chapter, the identification of surface phonon modes in GaAs nanowires and the energy dispersion relation are studied. Throughout chapter 6-7, self catalyzed InP and InP/InAs core-shell nanostructures using MOVPE are discussed. The morphological characterization and optical phonon modes in self catalyzed InP nanostructures are given in the chapter 6. The similar observations are extended to InP/InAs core-shell nanostructures in chapter 7.

Figures

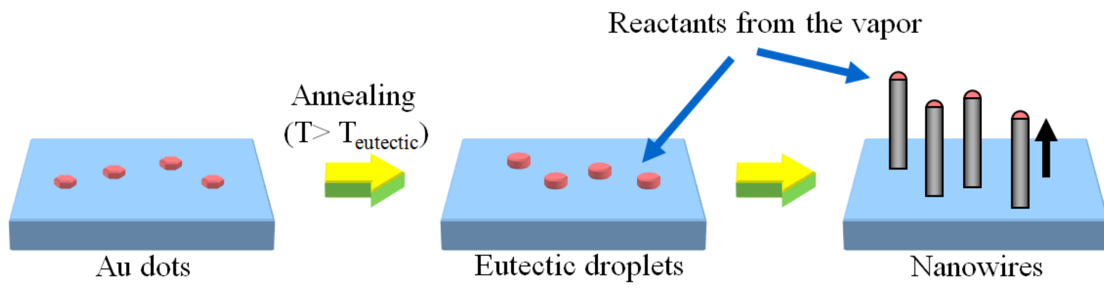

Figure 1.1 A schematic drawing of Vapor-Liquid-Solid process.

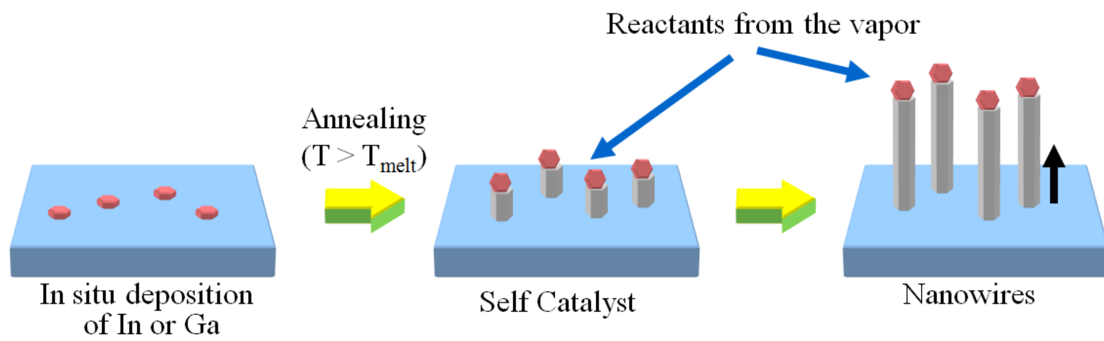

Figure 1.2 A schematic drawing of self-catalyzed nanowire growth.

References

[1] K. Haraguchi, T. Katsuyama, K. Hiruma, and K. Ogawa, Appl. Phys. Lett. 60, 745 (1992).

[2] J. Hu, T. W. Odom, and C. M. Lieber, Acc. Chem. Res. 32, 435 (1999).

[3] H. J. Fan, P. Werner, and M. Zacharias, Small 2, 700 (2006).

[4] K. A. Dick, K. Deppert, T. Mårtensson, W. Seifert, and L. Samuelson, J. Crystal Growth 272, 131 (2004).

[5] K. A. Dick, Zs. Geretovszky, J. N. Andersen, L. S. Karlsson, E. Lundgren, J.-O. Malm, A. Mikkelsen, L. Samuelson, W. Seifert, B. A. Wacaser, and K. Deppert, Nanotechnology 17, 1344 (2006).

[6] M. A. Verheijen, G. Immink,T. de Smet, M. T. Borgström, and E. P. A. M. Bakkers, J. Am. Chem. Soc. 128, 1358 (2006).

[7] R. S. Wagner and W. C. Ellis, Appl. Phys. Lett. 4, 89 (1964).

[8] S. Kodambaka, J. Tersoff, M. C. Reuter, and F. M. Ross, Phys. Rev. Lett. 96, 096105 (2006).

[9] S. Kodambaka, J. Tersoff, M. C. Reuter, F. M. Ross, Science 316, 729 (2007).

[10] M. T. Bjork, B. J. Ohlsson, C. Thelander, A. I. Persson, K. Deppert, L. R. Wallenberg, and L. Samuelson, Appl. Phys. Lett. 81, 4458 (2002).

[11] M. T. Bjork, C. Thelander, A. E. Hansen, L. E. Jensen, M. W. Larsson, L. R. Wallenberg, and L. Samuelson, Nano Lett. 4, 1621 (2004).

[12] E. P. A. M. Bakkers, M. T. Borgström, and M. A. Verheijen, MRS Bulletin 32, 117 (2007).

[13] M. Yazawa, M. Koguchi, A. Muto, M. Ozawa, and K. Hiruma, Appl. Phys. Lett. 61, 2051 (1992).

[14] K. Hiruma, M. Yazawa, T. Katsuyama, K. Ogawa, K. Haraguchi, M. Koguchi, and H. Kakibayashi, J. Appl. Phys. 77, 447 (1995).

[15] Q. Xiong, J. Wang, and P. C. Eklund, Nano Lett. 6, 2736 (2006).

[16] J. Johansson, L. S. Karlsson, C. P. T. Svensson, T. Martensson, B. A. Wacaser, K. Deppert, L. Samuelson, and W. Seifert, Nature Materials 5, 574 (2006).

[17] S.-G. Ihn, J.-I. Song, T.-W. Kim, D.-S. Leem, T. Lee, S.-G. Lee, E. K. Koh, and K. Song, Nano Lett. 7, 39 (2007).

[18] S.-G. Ihn, J.-I. Song, Y.-H. Kim, and J. Y. Lee, Appl. Phys. Lett. 89, 053106 (2006).

[19] M. He, M. M. E. Fahmi, S. N. Mohammed, R. N. Jacobs, L. Salamanca-Riba, F. Felt, M. Jah, A. Sharma, and D. Lakins, Appl. Phys. Lett. 82, 3749 (2003).

[20] M. Mattila, T. Hakkarainen, H. Lipsanen, H. Jiang, E. I. Kauppinenb, Appl. Phys. Lett. 89, 063119 (2006).

[21] J. Motohisa, J. Noborisaka, J. Takeda, M. Inari, T. Fukui, J. Crystal Growth 272, 180 (2004).

[22] B. Mandl, J. Stangl, T. Mårtensson, A. Mikkelsen, J. Eriksson, L. S. Karlsson, G. Bauer, L. Samuelson, and W. Seifert, Nano Lett. 6, 1817 (2006).

[23] Y. Wang, V. Schmidt, S. Senz, and U. Gösele, Nature Nanotechnol. 1, 186 (2006).

[24] A. M. Morales and C. M. Lieber, Science 279, 208 (1998).

[25] J. Weyher, J. Cryst. Growth 43, 235 (1978).

[26] E. I. Givargizov, Highly Anistropic Crystals, Terra Scientific Publishing Company, Tokyo, Japan (1987).

[27] L. Gao, R. L. Woo, B. Liang, M. Pozuelo, S. Prikhodko, M. Jackson, N. Goel, M. K. Hudait, D. L. Huffaker, M. S. Goorsky, S. Kodambaka, and R. F. Hicks, Nano Lett.9, 2223 (2009).

[28] A. Freundlich, A.H. Bensaoula, and A. Bensaoula, J. Cryst. Growth 127, 246 (1993).

[29] R. L. Woo, L. Gao, N. Goel, M. K. Hudait, K. L. Wang, S. Kodambaka and R. F. Hicks, Nano Lett. 9, 2207 (2009).

[30] W. Seifert, M. Borgström, K. Deppert, K. A. Dick, J. Johansson, M. W. Larsson, T. Mårtensson, N. Sköld, C. P. T. Svensson, B. A. Wacaser, L. R. Wallenberg, and L. Samuelson, J. Crystal Growth 272, 211 (2004).

[31] K. A. Dick, K. Deppert, L. Samuelson, and W. Seifert, J. Crystal Growth 297, 326 (2006).

[32] A. I. Persson, M. W. Larsson, S. Stenström, B. J. Ohlsson, L. Samuelson, and L. R. Wallenberg, Nature Materials 3, 677 (2004).

[33] S. A. Dayeh, E. T. Yu, and D. Wang, Nano Lett. 7, 2486 (2007).

[34] S. A. Dayeh, E. T. Yu, and D. Wang, J. Phys. Chem. C 111, 13331 (2007).

[35] S. A. Dayeh, E. T. Yu, D. Wang, Small 3, 1683 (2007).

[36] K. A. Dick, K. Deppert, T. Mårtensson, B. Mandl, L. Samuelson, and W. Seifert, Nano Lett. 5, 761 (2005).

[37] J. C. Harmand, G. Patriarche, N. Péré-Laperne, M-N. Mérat-Combes, L. Travers, and F. Glas, Appl. Phys. Lett. 87, 203101 (2005).

[38] J. Johansson, B. A. Wacaser, K. A. Dick, and W. Seifert, Nanotechnology 17, S355 (2006).

[39] U. Krishnamachari, M. Borgstrom, B. J. Ohlsson, N. Panev, L. Samuelson, W. Seifert, M. W. Larsson, and L. R. Wallenberg, Appl. Phys. Lett. 85, 2077 (2004).

[40] Z. H. Wu, X. Mei, D. Kim, M. Blumin, and H. E. Ruda, J. Q. Liu, and K. L. Kavanagh, Appl. Phys. Lett. 83, 3368 (2003).

[41] B. A. Wacaser, K. Deppert, L. S. Karlsson, L. Samuelson, and W. Seifert, J. Crystal Growth 287, 584 (2006).

[42] H. D. Park, S. M. Prokes, and R. C. Cammarata, Appl. Phys. Lett. 87, 063110 (2005).

[43] A. R. Adams and E. P. O'Reily, Materials for Optoelectronics, Academic Press, Boston (1996).

[44] R. W. Kelsall, I. W. Hamley, and M. Geoghegan, Nanoscale Science and Technology, John Wiley & Sons, Hoboken, New Jersey (2005).

CHAPTER 2

EXPERIMENTAL METHODS

2.1 Overview

Au catalyzed GaAs and self-catalyzed InP(As) nanostructure are grown via VLS growth mechanism using Molecular Beam Epitaxy (MBE) and Metal-Organic Vapor Phase Epitaxy (MOVPE). Figure 2.1 shows a schematic of experimental apparatus for InP nanostructure growth. It consists of a Veeco Discovery TurboDisc 125 MOVPE reactor that is directly connected to an ultrahigh-vacuum (UHV) analytical cluster. The UHV analytical cluster includes a main chamber, an STM chamber, an RDS chamber, an interface chamber, and a rotary sample exchange system (R2P2). This arrangement enables *in-situ* investigation of the structures grown in the MOVPE reactor without exposure to air.

The main chamber contains a Princeton Instrumentation low energy electron diffractometer (LEED), a Leybold-Inficon Transpector 300 amu mass spectrometer (MS), a Physical Electronics X-ray photoelectron spectrometer (XPS), and a BioRad FTS-40A infrared spectrometer (IR). The three characterization chambers have a base pressure of ~ 2×10^{-10} Torr, and all of them are connected to the R2P2. The R2P2 and interface chambers are held at ~ 1×10^{-9} Torr and have built-in areas for sample storage. The sample stages have a tungsten filament that is capable of heating the samples up to 550 °C.

Custom-made molybdenum sample sleds are used to hold the GaAs, InP, and Si substrates while they are transferred in and out of the MOVPE reactor and the analytical cluster. After growth, the sample is taken out from the reactor and placed in the loadlock chamber held at 1×10^{-7} Torr. The molybdenum sled is then transferred to the interface chamber by loading it onto

a wheel attached to a second pneumatic arm. From here, wobble sticks are used to move the sample to the rest of the analytical chambers.

In addition to surface characterization, the compound semiconductor materials were characterized *ex-situ* by photoluminescence spectroscopy (PL), scanning electron microscopy (SEM), and transmission electron microscopy (TEM). Raman Spectroscopy and Photoluminescence (PL) were measured on a Horiba LabRAM ARAMIS Spectrometer, courtesy of Dr. Vincent Gambin at Northrop Grumman Space Technology. Scanning electron microscopy (SEM) was performed on a Hitachi S4700 field emission SEM and a FEI NOVA 600 Dual Beam FIB/SEM at UCLA. Transmission electron microscopy (TEM) was carried out on FEI Titan S/TEM and a JOEL 1200EX, located at Electron Imaging Center for NanoMachines, California Nano-Systems Institute.

2.2 Growth Methods of III-V Compound Nanostructure

2.2.1 Solid State Molecular Beam Epitaxy

The Veeco GEN II Molecular Beam Epitaxy (MBE) equipped with solid Ga and As sources is used exclusively for the deposition of III-V compound semiconductor. MBE is an ultra high vacuum technique for the epitaxial or lay-by-lay deposition of thin films. This growth technique enables us to make compound semiconductor materials with great precision (< 0.01 nanometer) and purity (>99.99999%). These materials are layered one on top of the other to form semiconductor devices such as transistors and lasers, which are devices being used in such applications as fiber-optics, cellular phones, satellites, radar systems, solar cells, and display devices. MBE growth produces most complex structures of varying layers which are further processed to produce a range of electronic and optoelectronic devices, including high speed

transistors, light-emitting diodes, high-efficiency solar cells, and solid state lasers. Therefore, MBE is a powerful technique both for research into new materials and layer structures, and for producing high-performance semiconductor devices.

The supplying of high-quality low-dimensional semiconductor materials is one of the key limiting factors of semiconductor materials and devices in Northrop Grumman Space Technology. The picture of the NGST GEN II MBE is drawn in Fig. 2.2. The new NGST MBE facility has very special source arrangements with the combination of Arsenic, Antimony and Phosphorus crackers with Gallium, Aluminum, and Indium solid sources, which are unique in California and enable to produce to grow very complex III-V epitaxial structures. The sample size can be regular 2", 3", or 4" up to 12" wafers.

2.2.2 Metal-Organic Chemical Vapor Epitaxy

The Veeco Discovery TurboDisc 125 MOVPE reactor is used exclusively for the deposition of III-V compound semiconductors. The ultra high purity hydrogen gas (99.999% purity) purchased from Airgas is purified further in the SAES system before it enters the MOVPE reactor. The purified hydrogen (99.9999999% purity) is bubbled through the metalorganic precursors and carries some vapor with it to the reactor. The carrier gas is then drawn to the heated substrate by the pumping action of the rotating wafer platter at 1000 RPM. After processing, the sample is taken out of the reactor for characterization.

Pictures of the MOVPE system are shown in Fig. 2.3. The Turbo-Disc™ reactor and a loadlock chamber are located in the front as shown in Fig. 2.3a. The gas dilution networks are located in the back along with eleven chemical sources as shown in Fig. 2.3b. The eleven chemicals are trimethylindium (TMIn), trimethylgallium (TMGa), trimethylaluminum (TMAl),

tertiarybutylphosphine (TBP), tertiarybutylarsine (TBAs), trimethylantimony (TMSb), diethylzinc (DEZn), disilane (Si_2H_6), silane (SiH_4), nitrogen trifluoride (NF_3), and carbon tetrabromide (CBr_4). The metalorganic sources are placed in the temperature bath for control of the partial pressures of the precursors. The reactor is equipped with a Real-Temp™ optical monitoring system for accurate measurements of wafer temperature and film growth rate. It is also equipped with thermocouples that measure the temperature of the heating filaments.

The reactor is fully integrated with an Emcore Epiview™ 5926 software package for precision control of the growth process. Before growth, all conditions and process flow details are written as instructions in the software. The samples are prepared and placed on a 5" molybdenum platter. The sample size can be pieces as small as 1×1 cm^2 to 1×4 cm^2, or they can be 2", 3", or 4" wafers. The platter is loaded into the MOVPE reactor using a pneumatic linear transfer arm. Once ready to grow samples, the growth "recipe" is started by pressing "run." The reactor operates automatically and notifies the operator when the growth process is finished.

2.3 Raman Characterization of Semiconducting Materials

Raman spectroscopy is an important probing technique in characterizing nanostructure semiconducting materials because of its non-invasive nature and high spatial resolution. Raman scattering by intrinsic phonon modes is known to be sensitive to internal and external perturbations. It gives useful information on the composition, phase, crystallinity, or crystal orientation of semiconductors. Inelastic Raman scattering also provides further insight into the physical properties of electron or hole in doped materials [1]. Moreover, Raman scattering by electronic or vibronic excitations enables us to measure quantitative assessment for impurity and

dopant incorporation [1]. Furthermore, Raman scattering provides quantitative measurements on lattice dynamics with electron-phonon coupling and spin dynamics with magnetic order [2].

2.3.1 Raman Scattering Process

Raman scattering is an inelastic light scattering with momentum and energy transfer between photons and the scattering medium [2]. Figure 2.4 shows the Raman scattering process. The incident photon is described as its energy $E = \hbar\omega$ and momentum $\vec{p} = \hbar\vec{k}$. The incoming photon will be reflected at the sample surface or penetrated into the sample. It may experience in elastic or inelastic scattering processes with the elementary excitation of the medium and leave the medium as the scattered photon. If there is the energy difference between the incoming photon and the scattered photon, an energy transfer to the sample occurs in the scattering process. The Raman scattering depends on three single processes in which all events within the time are limited by the Heisenberg uncertainty principle [2]. Firstly, an incoming photon with wave vector $\vec{k_I}$ and frequency ω_I is absorbed, and the absorbing material is excited from its initial state i into intermediate virtual state ν. Secondly, an elementary excitation with wave vector $\vec{q}$ and frequency ω is created that is known as Stokes process or annihilated that is known as Anti-Stokes process. Finally, the material undergoes a transition from the intermediate state ν to the final state f. The process is accompanied with the emission of the scattered photon with $(\vec{k}_s, \omega_s)$. This one photon process follows the following conservation laws [2]:

$$\hbar\omega_I = \hbar\omega_s + \hbar\omega$$

$$\hbar\vec{k}_I = \hbar\vec{k}_s + \hbar\vec{q}$$

There are two types of energy transfer mechanisms in the scattering process. If the final state is higher than the initial state, the energy transfer $\hbar\omega$ from the photon to the system is positive

(Stokes process). If the final state is lower than the initial state, the system transferred energy to the photon is negative (Anti-Stokes process). The Stokes and Anti-Stokes processes were shown in Fig. 2.5. In most scattering processes, the energy transfer is much smaller than the energy of the incoming photons, $\hbar\omega \ll \hbar\omega_I$. The momentum transfer can be described as the following equation [2]:

$$\hbar\vec{q} \cong \frac{2n\hbar\omega_I}{c} \cdot \sin\frac{\phi}{2}$$

with n the refractive index of medium, c the velocity of light, and ϕ the angle between the direction of the incident and the scattered photon. The maximum momentum transfer is given by $\hbar\vec{q}^{max} = 2n\hbar\omega_I/c$ at $\phi = 180°$. For Raman experiments in solid medium, $\vec{q}^{max}$ is the order of 10^{-3} Å. This value is 1000 times smaller than both the characteristics wave vectors for most atomic lattice vibrations (phonons) and the highest momentum of the conduction electrons in the crystal. Therefore, the Raman scattering can detect excitations within the limit $\vec{q} \rightarrow 0$ [2].

2.3.2 Lattice Dynamics in Semiconducting Nanowire

Due to zinc-blende (ZB) crystal structure, InP and GaAs have a crystal structure of cubic lattice with $T_d^2(F\bar{4}3m)$ symmetry [3]. The ZB structure is composed of two cubic close packed sublattices of anion and cation atoms in a way that atoms of one sublattice occupy tetrahedral interstitial sites of the second sublattice. Face-centered cubic with a two-atom basis is the Bravis lattice of ZB structure. The phonon dispersions of ZB GaAs and InP are shown in Fig. 2.6. Since two atoms are located in the unit cell, six phonon branches exist which are ultimately split into three acoustic and three optical branches. The optical phonon modes at the Γ point are comprised of one longitudinal optical (LO) and two degenerate transverse optical (TO) modes. The LO-TO phonon splitting results in a slightly higher energy of the LO mode due to the long range electric

fields associated with long-wave LO [3].

In the nanostructure, GaAs and InP may also have a crystal structure of the hexagonal wurtzite (WZ) lattice with $C_{6v}^{4}(p6_3mc)$ symmetry in which all atoms occupy C_{3v} sites. Since four atoms are located in the unit cell, nine optical modes exist in the WZ compound semiconductors. From Group theory, the following phonon modes are predictable [4]: an A_1 mode polarized in the *z* direction (the *z* direction corresponds to the hexagonal *c*-axis), an E_1 branch with the phonon polarized in the *xy* plane, two E_2 branches called E_2^l (l for low) and E_2^h (h for high), and two silent B_1 modes. The first-order Raman active modes are the polar A_1 and E_1 modes as well as the unpolar E_2 modes. Due to the polar nature of A_1 and E_1 modes, two modes are split into LO and TO components. Due to the anisotropic short-range order of the hexagonal WZ structure, the polar modes exhibit both an LO-TO splitting and an $A_1 - E_1$ modes splitting. However, the $A_1 - E_1$ splitting is known to be very weak and negligible in the case of WZ [5]. Since the extent of the Brillouin zone in the WZ phase along the [0001] direction is only half of that in the ZB phase in [111] direction, the folding of the ZB dispersion relation along Γ → L with the result that the L-point in ZB is observable at the Γ point in WZ [6]. The identified peak positions of Raman spectra for GaAs and InP for this work are summarized in Table 2.I. The detailed investigation of lattice dynamics of GaAs, InP, InPAs nanostructures can be found in the Chapters 4, 6, and 7, respectively.

2.3.3 Surface Phonon Modes

Comparing to Raman scattering of bulk materials, nanostructured materials exhibited their unique vibration modes that the positions of TO and LO modes are changed with scaling down of the dimensionality [7]. In addition to the shift and broadening, new Raman mode can be

observed because of significant shape effect [8]. The existence of new boundary conditions and crystal symmetry breaking at the nanoscale give rise to electric and polarization forces. The surface represents new mechanical boundaries, since the surface atoms are not tightly bounded and formed a different local electric field from the bulk. Thus, the propagation of an optical phonon mediated by dipole-dipole interaction shows the activation in Raman spectra of inactive modes at the Brillion zone center (Γ point) [8,9].

Moreover, the surface optical phonons and breathing modes can occur at nanoscale [8]. The surface optical phonons are generated at the interface between different materials with different dielectric functions and propagate along the interface. The atoms involved in their propagation are those close to the surface, so that the amplitude of the oscillations decays exponentially with the distance from the surface. This mode is activated by a breaking of the translational symmetry of the surface potential, which in the case of the nanowire can be addressed to the presence of roughness, sawtooth faceting on the nanowire sidewall or to a diamter oscillation along the nanowire length.

Distinctive of SO modes allow a reliable assignment of the mode: the dependence of the position (1) on the dielectric constant of the medium surrounding the wires and (2) on the diameter of the wires [8]. Furthermore, the frequency of the SO modes at $\Gamma = 0$ is located between those of the TO and the LO. The detail study of SO mode dispersion at the interface between a semiconductor and a dielectric material can be found in the Chapter 5.

2.4 X-ray Photoelectron Spectroscopy

X-ray photoelectron spectroscopy (XPS), also known as electron spectroscopy for chemical analysis (ESCA), is widely used to analyze the composition of surfaces. In this

technique, x-rays strike the surface and remove electrons from the inner core-shells of atoms. By measuring the kinetic energy and number of photoelectrons emitted, the identity and chemical state of the elements within the sample can be determined.

The kinetic energy, E_k, of photoelectrons is related to their binding energy by:

$$E_k = h\nu - E_B - \phi_s,$$

where $h\nu$ is the energy of the photon (x-ray), E_B is the electron binding energy, and ϕ_s is the spectrometer work function, between 4.0 and 5.0 eV [10]. Since each core-level electron has a characteristic binding energy and a known probability of being ejected, the spectrum obtained by XPS gives specific information regarding the surface composition.

In our Physical Electronics 3057 x-ray photoelectron spectrometer, there are three major components: the x-ray generator, electron analyzer, and data acquisition system. X-rays are generated by applying 15 kV bias on the source anode while exposing it to a 300 W irradiating filament. Electrons emitted from the filament strike the anode, generating x-rays via fluorescence. The anodes installed in this instrument are aluminum and magnesium, which are cooled by circulating de-ionized water. The electron analyzer operates as an energy “window”, accepting only those electrons having energy within the selected voltage range, referred to as the pass energy. Electrons of a fixed kinetic energy are detected. The data acquisition system processes the number of photoelectrons emitted at each kinetic energy and generates the photoemission spectrum. This information is then used to identify the surface composition.

2.5 Photoluminescence Spectroscopy

Photoluminescence spectroscopy (PL) is a non-destructive method of probing the electronic structure of materials. In this technique, intense laser light is directed onto the surface.

The absorption of the light excites the electrons in the material into excited states. When the electrons return to the ground state, luminescence of the excess energy occurs. By measuring the wavelength and intensity of the photoluminescence spectrum, one can determine the bandgap (for direct bandgap semiconductors), defect levels, layer thickness (for quantum wells), and impurity levels [11,12].

Photo-excitation causes electrons within the material to move into excited states. When they return to their ground states, the excess energy is released via a radiative process or a non-radiative process as shown in Fig. 2.7. A radiative process yields emission of light whereas a non-radiative process results in lattice vibrations or heat release. The energy of the emitted light relates to the difference in energy levels between the excited state and the ground state. The most common radiative transition in bulk semiconductors is between the bottom of the conduction band and top of the valence band as shown in Fig. 2.8a. In quantum wells, radiative transitions between subbands (due to quantum confinement) of the conduction and valence bands occur as shown in Fig. 2.8b. In this case, the PL spectrum exhibits multiple peaks at higher energies than the main transition. The quantity of the emitted light from each level is related to the individual contributions to the radiative process.

In the PL system, there are three major components: the light source, the detector, and the data acquisition system. An argon laser with 488 nm emission line is used as the photo-excitation source. Silicon or indium gallium arsenide detectors are used to measure the photoluminescence intensity between 300 and 900 nm or between 900 and 1800 nm, respectively. The PL data are acquired and processed, and then plotted as a spectrum of intensity versus wavelength.

2.6 Scanning Electron Microscopy

Scanning electron microscopy (SEM) is a widely used surface imaging technique. In this work, SEMs are fully employed to study morphologies, crystal shapes and real-time electrostatic interaction of as-grown nanostructures. Unlike an optical microscope, SEM uses electrons that have five to six orders of magnitude shorter wavelength, thus providing high-resolution images of the sample surface [13]. In this technique, a beam of electrons strikes the surface of a sample and scatters within the sample at or near the surface. The electron scattering process results in emission of secondary electrons, characteristic X-rays, backscattered electrons, and cathodoluminescence as shown in Fig. 2.9. Detection of these signals provides information on surface morphology, chemical composition, and crystallographic structure of the sample.

Secondary electrons are of low energy and originate from the first few nanometers from the surface. Detection of these electrons produces high-resolution images of the surface, revealing structures 1 to 5 nm across. Characteristic x-rays are produced when the electron beam removes the inner shell electron, causing an outer shell electron to fill in and give up the difference in energy. These x-rays are then used to identify the chemical composition of the surface. This technique is also known as energy dispersive x-ray analysis (EDX). Backscattered electrons are high-energy electrons originated in the electron beam, which are reflected or backscattered by the sample. The image of BSE provides contrast in regions with different elemental composition, especially when the variation in atomic numbers is significant. Cathodoluminescence is the emission of light from electronically excited atoms that are returning to their ground state. The emitted wavelengths can be plotted in a spectrum and can be used to identify the elements.

The quality of an SEM image depends on the electron beam, which is characterized by the brightness equation. This equation incorporates the current density and the angular spread of electrons:

$$Brightness = \frac{J_{probe}}{\pi \alpha_{probe}^{2}} = \frac{4 i_{probe}}{\pi^{2} d_{probe}^{2} \alpha_{probe}^{2}}$$

where J_{probe} is the electron probe current density, i_{probe} is the electron probe current, d_{probe} is the electron probe diameter, and α_{probe} is the electron probe convergence. Figure 2.10 is a schematic of the electron beam striking the sample, specifying the three major parameters: probe current i_{probe}, probe diameter d_{probe}, and probe convergence α_{probe}. These three parameters cannot be tuned independently since they are interrelated by the above equation. For example, smaller probe diameters provide better resolution, but give smaller probe current and a less intense signal from secondary effects. Nevertheless, these parameters can be optimized by carefully designing the instrument. In addition, the operator must pay careful attention to achieve optimal surface imaging.

A Hitachi S4700 Field Emission SEM and FEI Nova 600 Dual Beam FIB/SEM are used for all of the SEM work described in this thesis. The instrument consists of the field emission electron gun, condenser lenses, objective lenses, EDX analyzer, detectors, sample chamber, and loadlock chamber as shown in Fig. 2.11. The electrons are generated from a cold field emission source with a tungsten tip. The electrons are extracted and accelerated by an applied voltage of >1kV. The stream of electrons is tuned by a magnetic electron-optic system, which consists of a condenser lens, objective lens, aperture, astigmatism correction coil, and scanning coil. The electron beam strikes the sample and generates secondary electrons, backscattered electrons, x-

rays, and cathodoluminescence. These signals are detected and amplified by the instrument and displayed on the computer monitor.

2.7 Transmission Electron Microscopy

Transmission electron microscopy is a powerful technique for characterization of nanostructures. Due to continued efforts in electron optics, the lateral resolution of electron microscopes has now dropped below 0.1 nm [14]. Additionally, the ability of forming strongly focused electron probes [15] offers electron microscopes with the capability to provide analytical techniques with high lateral resolution. The combination of high-resolution imaging and analytical analysis offers valuable structural and chemical information to nanostructure growers, allowing them to optimize the crystallinity, morphology, and chemistry of nanostructures.

In this study, TEM observations were carried out in scanning transmission electron microscope (STEM) FEI Titan (See Fig. 2.12) at California NanoSystems Institute, University of California Los Angeles. Titan equipped with a 300 keV field emission gun and Cs corrector allows us to obtain high resolution and analytical TEM/STEM with a 1.2 nm spherical aberration coefficient and 0.24 nm Scherzer resolution. This TEM allows the possibility to get routinely atomic resolution images and EDX spectra from nanostructures using both heating (1300˚C) and cooling (liquid N_2) holders for controlled-temperature studies. It is also equipped with annular dark-field detectors for STEM imaging and post-column Gatan Imaging Filter (GIF) for energy-filtered diffraction, imaging and EDX analysis. Low and high magnification images and digital videos with 15 frames per second time resolution are recorded using a Gatan Orius 600SC camera.

Figures

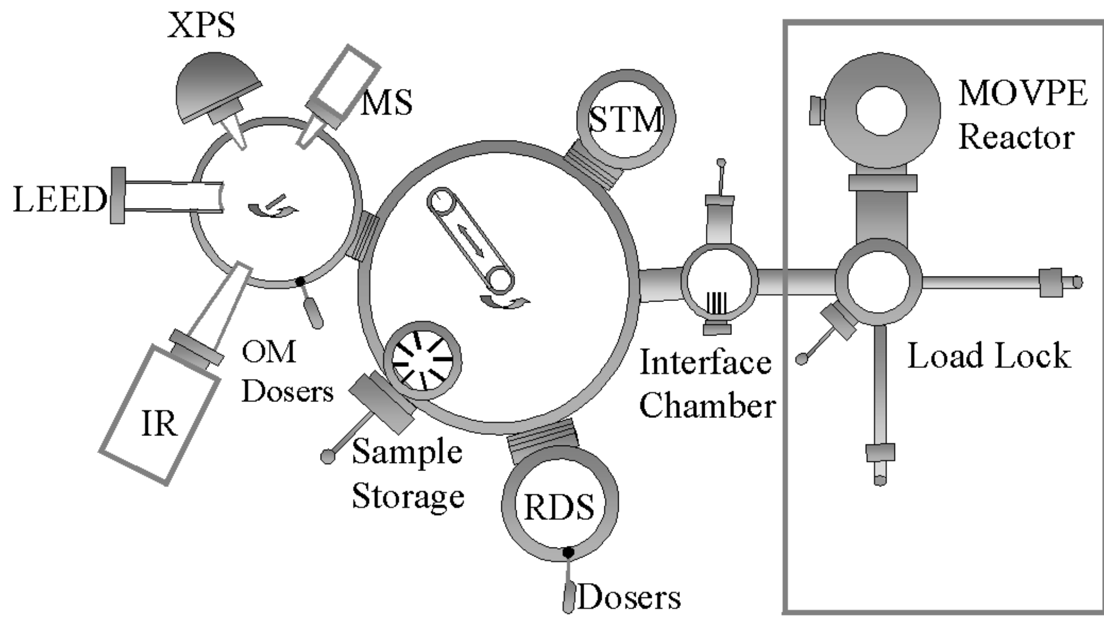

Figure 2.1 A schematic of the experimental apparatus (Adapted from [16], [17]).

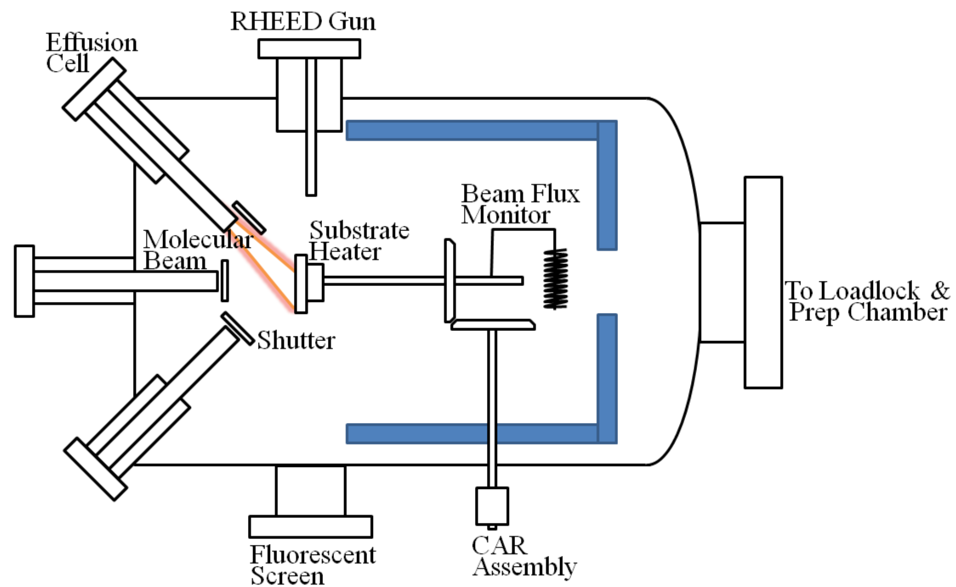

Figure 2.2 Top: A schematic drawing of a generic MBE system, Bottom: Veeco GEN II MBE, installed at the Northrop Grumman Space Technology, Redondo Beach, CA.

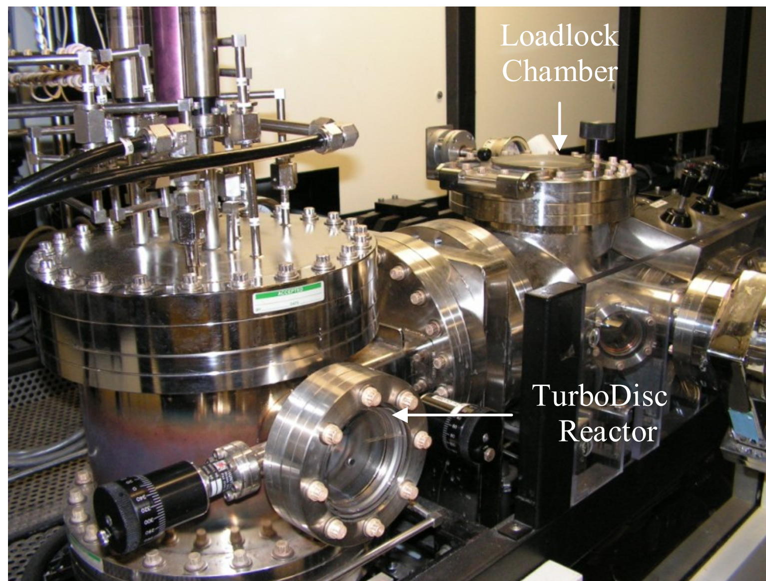

Figure 2.3 Pictures of the Emcore D125 MOVPE system installed at UCLA. Top: The front of the system showing the reactor chamber and loadlock chamber; Bottom: the back of the system showing the metalorganic sources (in constant temperature baths) and the gas flow manifold (Adapted from [18]).

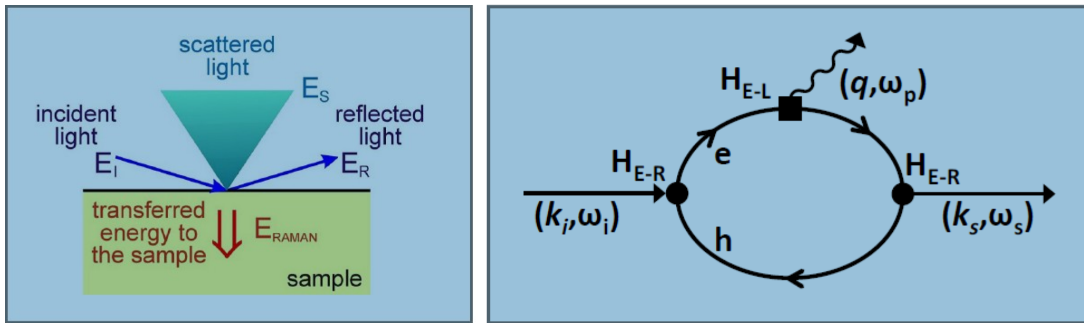

Figure 2.4 The Raman Scattering Process and corresponding Feynman's diagram (Images reproduced from Ref. [2,3]).

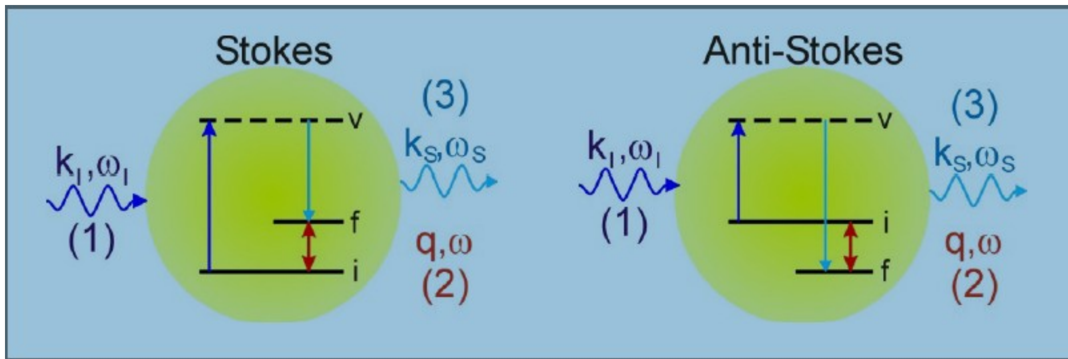

Figure 2.5 Raman effect in the energy level. In Stokes processes, the final state is above (left), in anti-Stokes process it is below the initial state (right) (Reproduced from [2]).

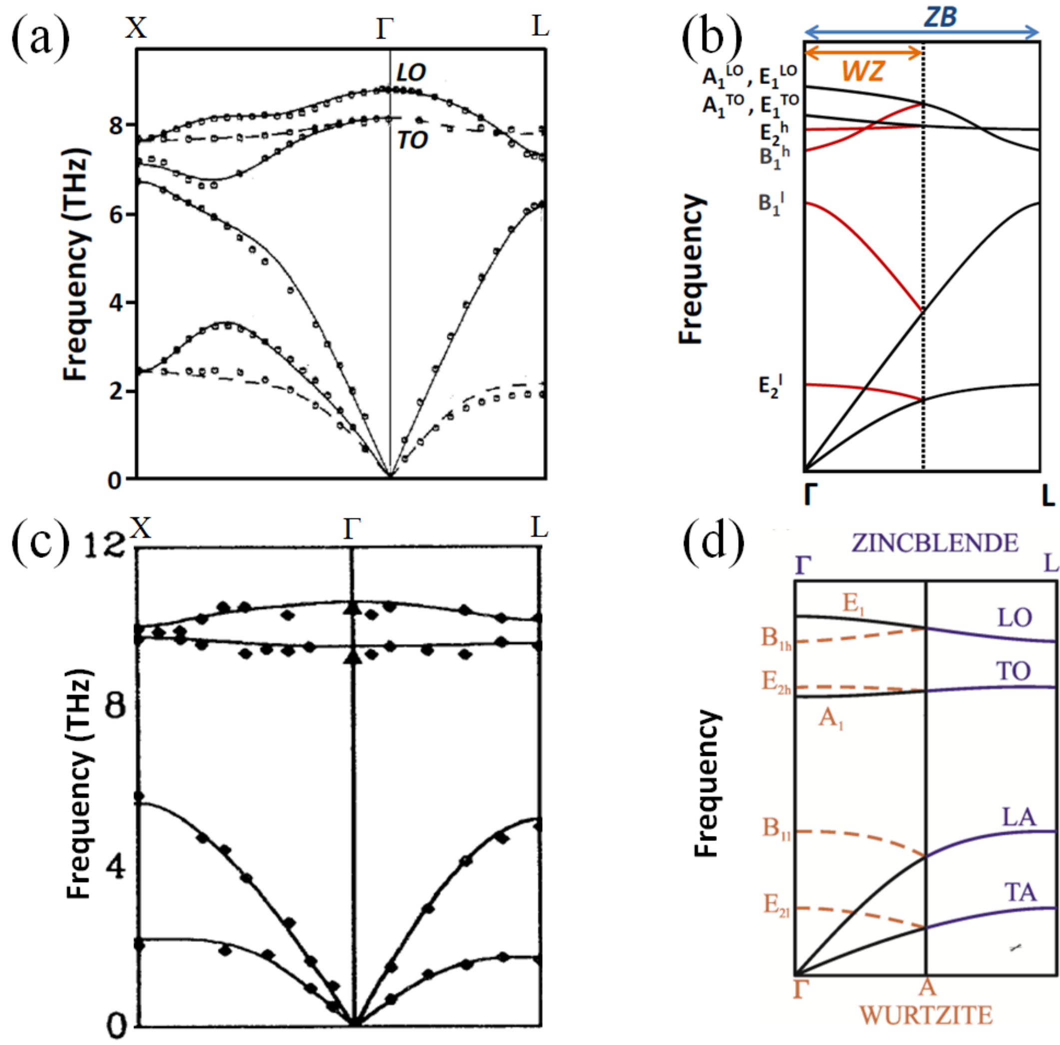

Figure 2.6 (a) Phonon Dispersion at the Brillouin zone center of ZB GaAs (Reproduced from [19]), (b) Schematic representation of phonon dispersion of WZ GaAs as a result of the one folding of the ZB dispersion relation along $\Gamma \rightarrow L$ (Reproduced from [20]), (c) Phonon dispersion of ZB InP (Reproduced from [21]), (d) Schematic representation of phonon dispersion of WZ InP as a result of phonon folding from ZB along [111] to the WZ along [0001] phase (Adapted from [20]).

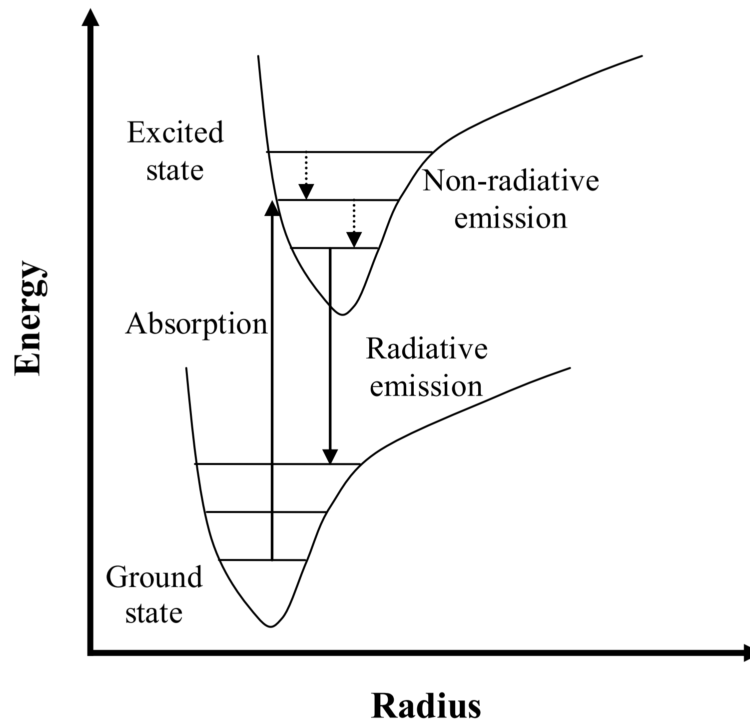

Figure 2.7 A schematic illustration of absorption and radiative and non-radiative emission from an electronically excited atom (Reproduced from [18]).

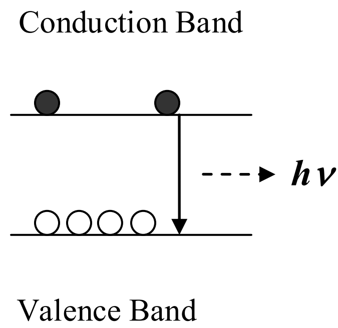

(a)

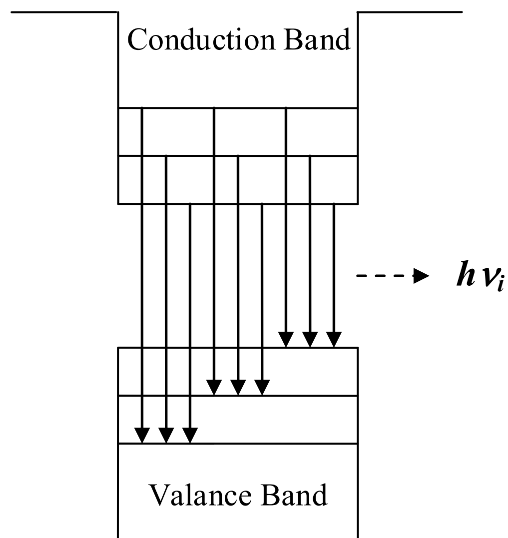

(b)

Figure 2.8 An illustration of photoluminescence (a) in a bulk semiconductor and (b) in a quantum well (Reproduced from [18]). A single PL peak is expected for the bulk material, whereas satellite peaks are expected for the quantum well.

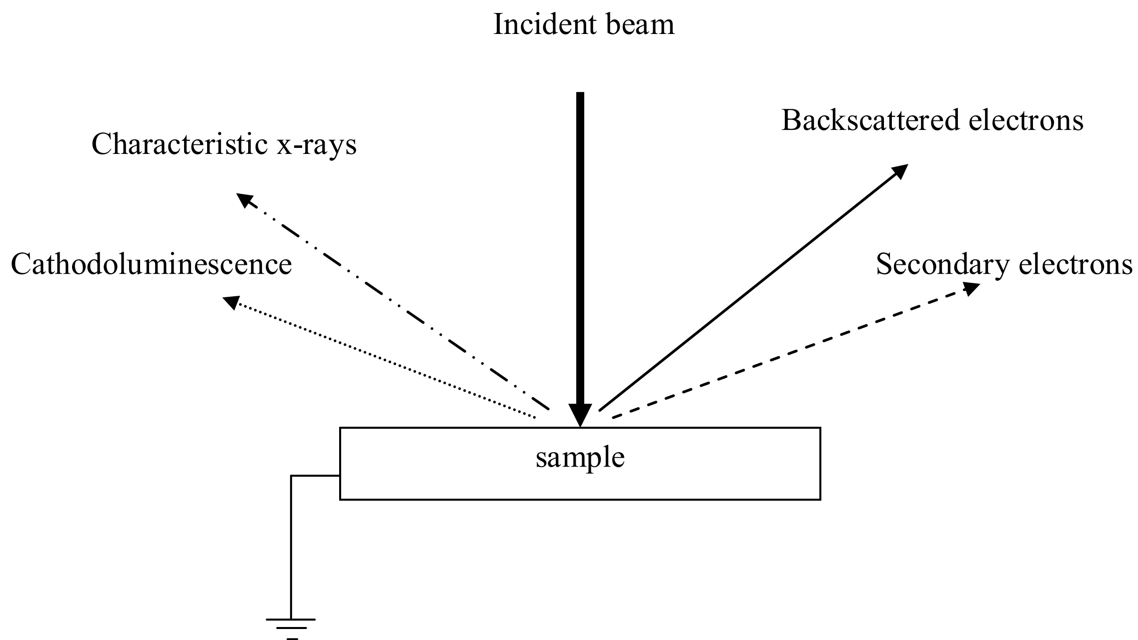

Figure 2.9 Schematic of electron scattering process, showing emission of secondary electrons, backscattered electrons, characteristic x-rays, and cathodoluminescence [13].

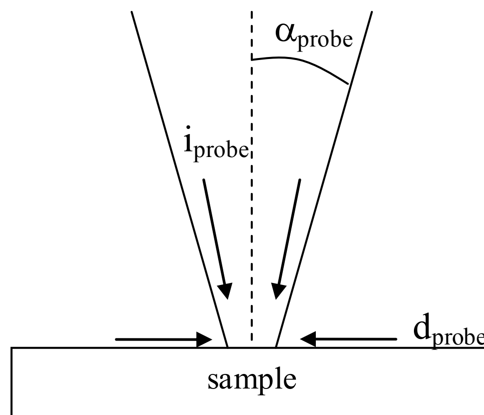

Figure 2.10 A schematic diagram showing the point where the electron beam strikes the sample. The three major electron beam parameters are probe diameter, d_{probe}, probe current, i_{probe}, and probe convergence, α_{probe} [13].

Figure 2.11 Pictures of a Hitachi S4700 Scanning Electron Microscope (left) and FEI Nova 600 SEM/FIB (right).

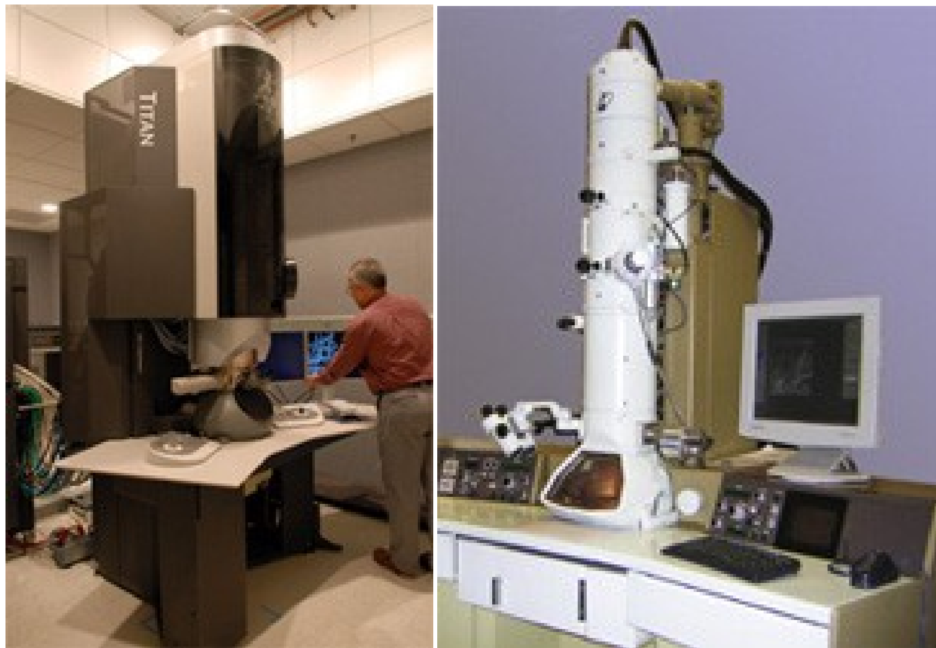

Figure 2.12 Transmission Electron Microscope - FEI Titan S/TEM (left) and JEOL 1200EX (right).

STRUCTURE	MODE	POSITION (cm^{-1})	
		GaAs	InP
ZB	TO	267	305.0
	LO	291	345
WZ	A_1(TO)	267	305.0
	A_1(LO)	291	336
	E_1(TO)	267	305.0
	E_1(LO)	291	341
	E_2^h	259	254
	E_2^l	N/A	N/A

Table 2.I Raman active phonon modes for GaAs and InP Nanowires in this work

References

[1] B. Prévot and J. Wagner, Prog. Cryst. Growth Charact. Mater. 22, 245 (1991).

[2] M. Opel and F. Venturini, Raman Scattering in Solid, Will be published in the European Pharmaceutical Review.

[3] P. Y. Yu and M. Cardona, Fundamentals of Semiconductors. Springer Berlin / Heidelberg, 2010.

[4] C. A. Arguello, D. L. Rousseau, and S. P. S. Porto, Phys. Rev. 181, 1351 (1969).

[5] S. Crankshaw, L. C. Chuang, M.Moewe, and C. Chang-Hasnain, Phys. Rev. B 81, 233303 (2010).

[6] I. Zardo, S. Conesa-Boj, F. Peiro, J. R. Morante, J. Arbiol, E. Uccelli, G. Abstreiter, and A. Fontcuberta iMorral, Phys. Rev. B 80, 245324 (2009).

[7] G. D. Mahan, R. Gupta, Q. Xiong, C. K. Adu, and P. C. Eklund, Phys. Rev. B 68,073402 (2003).

[8] I. Zardo, G. Abstreiter, and A. Fontcuberta i Morral, "Raman Spectroscopy on Semiconductor Nanowires" in Nanowires, Edited by P. Prete. ISBN 978-953-7619-78-4.

[9] H. M. Lin et al., Nano Lett 3, 4 (2003).

[10] A. B. Christie, "X-RayPhotoelectron Spectroscopy" in Methods of Surface Analysis, Edited by J. M. Wallas, Cambridge University Press, New York, NY, 1987.

[11] K.D. Mielenz, Optical radiation measurements: measurement of photoluminescence, vol. 3, Academic Press, New York, 1982.

[12] D.A. McQuarrie and J.D. Simon, Physical chemistry: a molecular approach, University Science Books, Sausalito, 1997.

[13] P.J. Goodhew, J. Humphreys, and R. Beanland, Electron microscopy and analysis, 3rd edition, Taylor & Francis, New York, 2001.

[14] M. Haider, H. Rose, S. Uhlemann, S. Kabius, and K. Urban, J. Electron Microscopy 47, 396 (1998).

[15] O. L. Krivanek, N. Deelby, and A. R. Lupini, Ultramicroscopy 78, 1 (1999).

[16] D.M. Joseph, Hydrogen adsorption on gallium arsenide (100): an infrared study, M.S. dissertation, UCLA, 1988.

[17] P.E. Gee, The infrared spectroscopy of adsorbed hydrogen and organometallic molecules on gallium arsenide (100), Ph.D. dissertation, UCLA, 1994.

[18] R. L. Woo, Crystal Growth and Properties of Indium Phosphide Nanowires, Ph.D. dissertation, UCLA, 2008.

[19] D. Strauch and B. Dorner, J. Phys.: Condens. Matter 2, 1457 (1990).

[20] E. G. Gadret, T. Chiaramonte, M. A. Cotta, F. Iikawa1, M. M. de Lima, Jr., A. Cantarero, and J. R. Madureira, arXiv:1212.1491v1 (2012).

[21] J. Fritsch, P. Pavone, and U. Schröder, Phys. Rev. B 52, 11326 (1995).

CHAPTER 3

EFFECT OF ELECTRON BEAM LITHOGRAPHY PATTERNING PARAMETERS ON THE Au-CATALYZED GROWTH OF GaAs NANOWIRE ON GaAs(111)B SUBSTRATE

3. 1 Introduction

Semiconducting group III-V nanowires, such as GaAs, InAs, and InP, owing to their high carrier mobilities and low band gaps, form an important class of materials with potential applications in nanoelectronics and optoelectronics, as chemical and biological sensors, and in energy harvesting devices [1,2,3]. To-date, nanowires have been grown using a variety of growth techniques such as self-catalyzed [4], oxide-templated [5] dislocation-assisted growth [6] among which the vapor-liquid-solid (VLS) [7] process is probably the most widely adapted method. And, considerable progress has been made over the past decade in developing methods to control the nanowire morphology, structure, and composition [8,9]. Wafer-scale growth of highly-ordered arrays of nanowires with nearly identical morphology, structure, composition has been demonstrated using lithographically-patterned substrates as templates [10,11,12]. However, relatively little is known concerning the role of catalyst patterning parameters on the growth of nanowires. The properties of these nanowires were found to critically depend on the thickness and the linear dimension of the catalyst pattern elements.

In this chapter, we present results from a detailed investigation of the influence of electron-beam dose during electron-beam lithography (EBL), pattern size, and spacing on the fractional surface density of nanowires. Au dots of two different sizes and three different inter-

dot spacings are patterned via EBL on a 4" GaAs(111)B wafer. Several arrays of such patterns are prepared by applying a range of electron beam doses. In a single growth experiment, solid-source Ga and As precursors are used to grow GaAs nanowires on these patterned wafers. We measured the fractional surface densities of the resulting nanowires as a function of electron beam dose, Au dot size, and inter-dot spacing.

3.2 Experimental Details

All of our experiments are carried out on a 4" GaAs(111)B wafer. First, 200-nm-thick film of poly-methylmethacrylate (PMMA) is spin-coated on the wafer. Using EBL at 50 keV, we prepared 31 rows (labeled A to AE) of 11 identical patterns, as shown in Fig. 3.1. Each pattern consists of 6 rectangular regions that are made up of 250 × 150 ordered arrays of dots of nominal size D (= 100 nm and 150 nm) separated by inter-dot spacing S (= 100 nm, 150 nm, and 250 nm). Each of the rows is patterned using a different electron beam dose Q with increasing doses from Q = 145 $\mu C/cm^2$ for the Ath row to 595 $\mu C/cm^2$ for the AE^{th} row. The patterned wafer is developed at room temperature by dipping for 30 s in a liquid solvent composed of a mixture of isopropyl alcohol (IPA) and methyl isobutyl ketone (MIBK) with the ratio of 3:1. Au films, 1-nm-thick, are then sputter-deposited on the patterned wafer and the wafer air-transferred to an ultra-high vacuum (UHV, base pressure < 5.5×10^{-10} Torr) molecular beam epitaxy (MBE) system equipped with solid Ga and As sources for GaAs deposition. In the growth chamber, the wafer is cleaned of any surface oxides by heating at 480 ^oC for 600 s in the presence of As vapor maintained at a pressure of 1.05×10^{-5} Torr. The sample is subsequently annealed at 485 ^oC for 120 sec in UHV to generate Au-Ga alloy droplets. Finally, nanowires are grown at 490 ^oC for 2400 s using a Ga beam pressure of 3.04×10^{-7} Torr and a thermally cracked As_2 pressure of

1.05×10^{-5} Torr. The as-grown samples are characterized using FEI Nova 600 field-emission scanning electron microscopy (SEM) and FEI Titan 300 keV high resolution transmission electron microscopy (TEM). For TEM, individual nanowires are mechanically exfoliated from the wafer and drop cast onto a 3 mm Cu grid. SEM images are processed using Image J software [13] to measure the image intensities of the patterns. From the SEM images of the dot patterns, we measured the dot sizes D to be 106 ± 5 nm and 144 ± 5 nm and the inter-dot spacings S to be 104 ± 5 nm, 156 ± 4 nm, and 258 ± 4 nm. Please note that in the following sections, we use the nominal D (= 100 and 150 nm) and S (= 100, 150, and 250 nm) values for convenience. The fractional surface density of nanowires in a given pattern is determined [14].

3.3 Results and Discussion

Figure 3.1 shows representative secondary electron SEM images acquired from a Au covered GaAs(111)B sample with circular dot patterns created using EBL with Q = a) 220 $\mu C/cm^2$, b) 295 $\mu C/cm^2$, c) 460 $\mu C/cm^2$, and d) 535 $\mu C/cm^2$. In the patterns created using low electron beam doses, for example Q = 220 $\mu C/cm^2$, the dots are barely visible. With increasing Q, we obtain well-defined dots with sharp boundaries. The plot in Fig 3.2 shows spatial variations in normalized intensities of the SEM images in Figs. 3.2a–d. Here we define normalized intensity as the ratio of intensity at a given pixel with respect to average intensity of the image [15, 16]. We find that the intensities of the dots increase with increasing Q. This trend follows clearing dose [17]. As a result, the residual thickness of the polymer film decreases with increasing dose [18,19,20].

Fig. 3.3a is a typical SEM image of an individual GaAs nanowire grown in the Yth row pattern (D = 150 nm, S = 150 nm, Q = 505 $\mu C/cm^2$). The nanowire is 2.5 μm long and is strongly

tapered with a base diameter of ~ 192 nm and a tip diameter of ~ 28 nm. The top-view SEM image of the wire in Fig. 3.3b shows that the wire is facetted with a hexagonal cross-section. From SEM images of over 50 nanowires acquired from the same pattern, we determine the average length and base diameters of nanowires as 3.0 ± 0.5 μm and 170 ± 60 nm, respectively. However, nanowires are observable up to 10 μm in length. Overall nanowire morphology shows random orientation respect to substrate and broad size distribution of base diameter of nanowire, indicating none Au catalyzed nanowire growth that surface migration of Ga adatom with a mean length of 3 μm may induce nanowire growth [21]. Random orientation of GaAs nanowires results in the large variations in Au-Ga catalyst [22], catalyst migration of Au [23,24] or Ga [25,26], and relatively lower growth temperature [27]. We note that the base diameters of the wires are larger than the Au dot size D, which is likely due to the non-catalyzed deposition along the sidewalls during the catalyst-assisted growth process [28]. These results are also typical of all the nanowires grown in other patterns, irrespective of D, S, and Q.

In order to determine the crystallinity of the GaAs nanowires, we obtained TEM images and diffraction patterns of individual nanowires exfoliated from the wafer. Figure 3.3c is a bright-field TEM image of one such wire. The relatively uniform contrast along the wire is suggestive of spatially homogeneous structure and composition in the wire. The darker contrast at the wire tip is likely due to the presence of a Au catalyst, expected for the vapor-solid-solid and VLS growth of nanowires. The fact that the wire is highly tapered along with a smaller catalyst at the top is indicative of Au diffusion away from the tip during growth [24]. The inset in Fig. 3.3c is a selected area electron diffraction (SAED) pattern, viewed along the [112] axis, from the region highlighted in the TEM image. From the SAED data, we determined the crystal structure of nanowire as zinc blende (cubic) and the wire growth direction as $\langle 111 \rangle$. Figures 3.3d

and 3.3e show high-resolution TEM images of the tip-wire interface and a portion of the wire, respectively. The smooth curved shape of the tip, clearly visible in Fig. 3.3d, is commonly observed during the VLS growth of nanowires and suggests the presence of a liquid catalyst during growth [29,30]. From the lattice-resolved images in Figs. 3.3d and 3.3e, we measured interplanar spacings of 0.23 nm and 0.33 nm for the tip and wire, respectively corresponding to ⟨111⟩ planes in Au and GaAs [31]. We obtained similar results for randomly selected 30 wires extracted by mechanical exfoliation from other patterned regions of the wires. That is, nanowire morphologies and crystal structures are independent of the electron beam patterning parameters *D, S,* and *Q*.

In the following sections, we focus on understanding the effect of *D, S,* and *Q* on the fractional surface density of nanowires. Figures 4.4a-d are top-view SEM images of the patterned areas created using different *Q*. Figure 4.4a is a low-magnification SEM image of the region containing two patterns $Q = 340\ \mu C/cm^2$ and $355\ \mu C/cm^2$. The brighter contrast in the red rectangle is due to the presence of nanowires (see higher magnification image in Fig. 4b. The absence of any such contrast within the image is attributed to the lack of nanowires in that region. From a series of SEM images acquired from all the patterns, we find that regions patterned using $Q < 355\ \mu C/cm^2$ did not yield any nanowires. In Fig. 4b, we find nanowires in three out of the six patterns, which contain Au dots with $D = 150$ nm separated by distances $S = 100$ nm, 150 nm, and 250 nm from left to right in the image. The other three patterns invisible in the image due to the lack of any nanowires contain smaller dots of size $D = 100$ nm. We observed similar behavior in all the patterns prepared using doses $Q < 400\ \mu C/cm^2$. At higher doses, for example $Q = 400\ \mu C/cm^2$, nanowires are observed to grow in five out of the six patterns (see Fig. 3.4c). And, at $Q > 400\ \mu C/cm^2$, nanowires are found in all the six patterns as shown in Fig. 3.4d.

The effects of electron beam dose Q and inter-dot spacing S on the fractional surface density of nanowires grown using Au dots of size D = 100 nm are pictorially illustrated in Fig. 3.5. For a given D and S, the density of nanowires in the patterns increase with increasing Q. The density is also found to increase with decreasing S. In our experiment, this behavior is consistently observed from all the patterns fabricated using a range of Q values. From the images of the patterns, we measured the fractional surface density of nanowires as a function of Q, D, and S. Figure 3.6a is a plot of the fractional surface density as a function of Q for all the six different combinations of D and S. For $Q \leq 350$ μC/cm^2, nanowires are not observed in any of the patterns, irrespective of D and S. For $Q \geq 475$ μC/cm^2, nanowire yield is maximum (the nanowire density is ~ 80%) in all of the patterns and is independent of Q. In the patterns prepared using intermediate Q values between 350 μC/cm^2 and 475 μC/cm^2, the nanowire coverage increases linearly with Q. The observed effect of Q can be understood as follows: at low electron beam doses, the pattern is underexposed and does not be completely developed. Consequently, Au is not deposited in the patterns and nanowires do not grow. At the intermediate electron beam dose but below the critical dose, only a fraction of the polymer chains in the PMMA film breaks up and the extent of damage increases linearly with Q [17,18] Therefore, some amount of Au is deposited in the patterns. While nanowires can grow out of these patterns, their base diameters are likely to be narrower and their lengths shorter owing to smaller sized catalysts at the tips which diffuse away during growth. A net effect is the reduced nanowire density in the patterns created using lower Q. At electron beam doses above the critical dose (for example, $Q \geq 490$ μC/cm^2), the pattern film is completely developed. Hence, the amount of Au deposited and the nanowire yield are maximized in these patterns. This observation is consistent to GaP nanowire [8].

Interestingly, nanowire yield is also found to vary with the parameters *D* and *S*. This effect is more pronounced in the patterns obtained using intermediate *Q* values, i.e. between 350 μC/cm^2 and 475 μC/cm^2. From Fig. 3.6a data, we find that the minimum dose *Q* to yield nanowires is ~ 350 μC/cm^2 in the patterns with dots *D* = 150 nm. In contrast, higher doses ($Q >$ 380 μC/cm^2) are required to yield nanowires in the patterns with smaller dots *D* = 100 nm. Figure 3.6b shows the effect of inter-dot spacing *S* on nanowire yield. We find that nanowire yield is higher in the patterns with smaller inter-dot spacing. That is, for a given Q, larger D and smaller S promote nanowire growth. In order to explain these results, we assume that a minimum concentration of Au, which varies with growth temperature and flux, is necessary for the nucleation and growth of nanowires. During EBL, electron beam broadening and multiple scattering events can lead to the proximity effect [18,32]. Such effects are likely to be more pronounced in the patterns with smaller S because the fractional surface density of dots is higher. Similarly, the extent of damage to the polymer film around the intended dot scales with dot size and hence is higher around dots with larger D. Hence, those patterns with larger D and smaller S receive more amounts of Au per unit area, which result in higher density of nanowires.

3.4 Conclusion

In conclusion, we investigated the correlation between predeposited catalyst layers and nanowire density, varying electron beam dose, patterned dot size, and inter-dot spacing on the electron-beam lithographically patterned substrate. Au catalyzed GaAs nanowires were successfully synthesized on 4 inch GaAs(111)B wafer via the VLS growth process using solid Ga and As sources. Using scanning and transmission electron microscopy, we determined the as-grown nanowire morphologies and crystal structures. We find that the GaAs wires are highly

tapered with facetted cross-sections, exhibit zinc blende structure, and grow along $\langle 111 \rangle$. The presence of Au at the wire tips is suggestive of the operation of VLS process. From the measurements of the fraction surface coverage of nanowire in the patterns, we find that higher electron beam doses, larger dot sizes, and shorter inter-dot spacings promote nanowire growth. Our results help identify the key electron beam lithography parameters that are desirable for large-scale, high-density, growth of nanowires. We expect that our experimental approach is general and applicable to other materials systems.

Figures

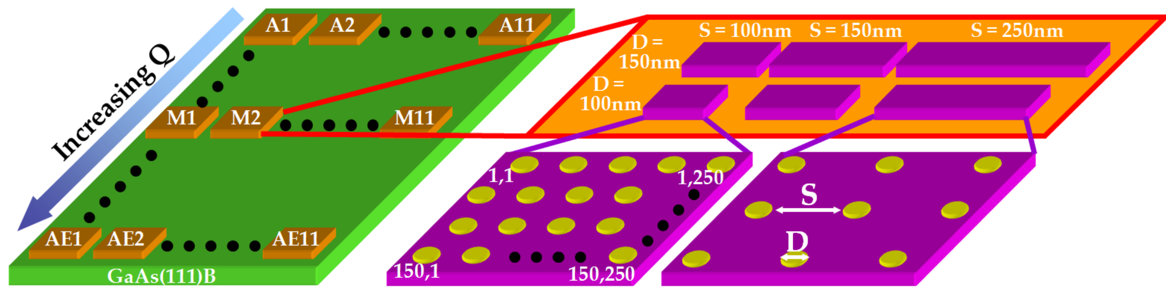

Figure 3.1 Schematic overview of patterns on GaAs(111)B wafer. Each of the 31 patterns labeled alphabetically from A to AE consists of 6 rectangular regions made up of 250 × 150 ordered arrays of a given dot-size *D* (= 100 and 150 nm) and inter-dot spacing *S* (= 100, 150, and 250 nm).

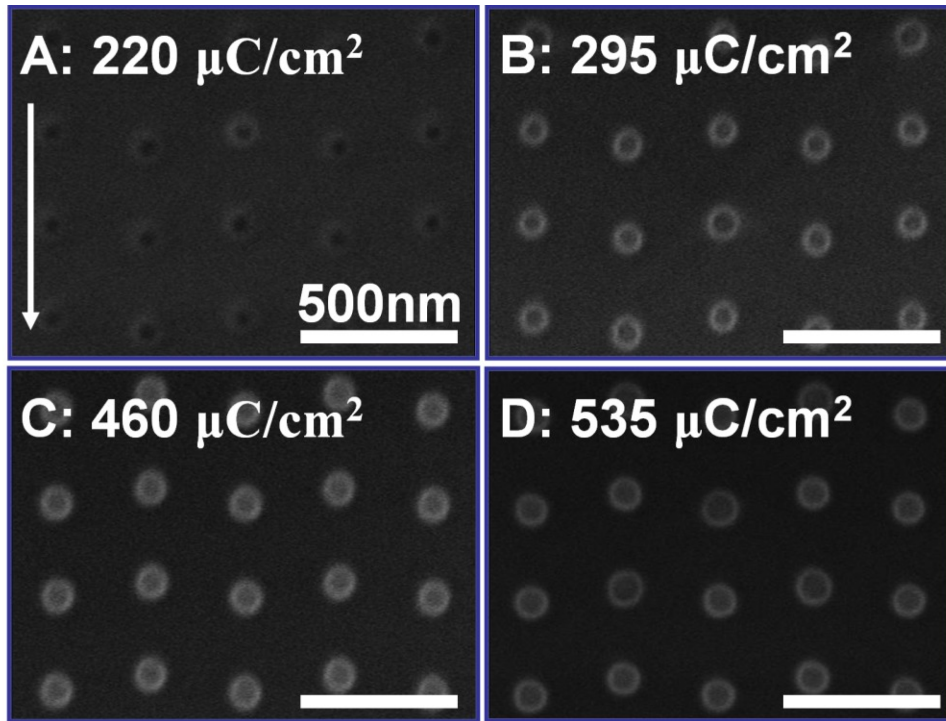

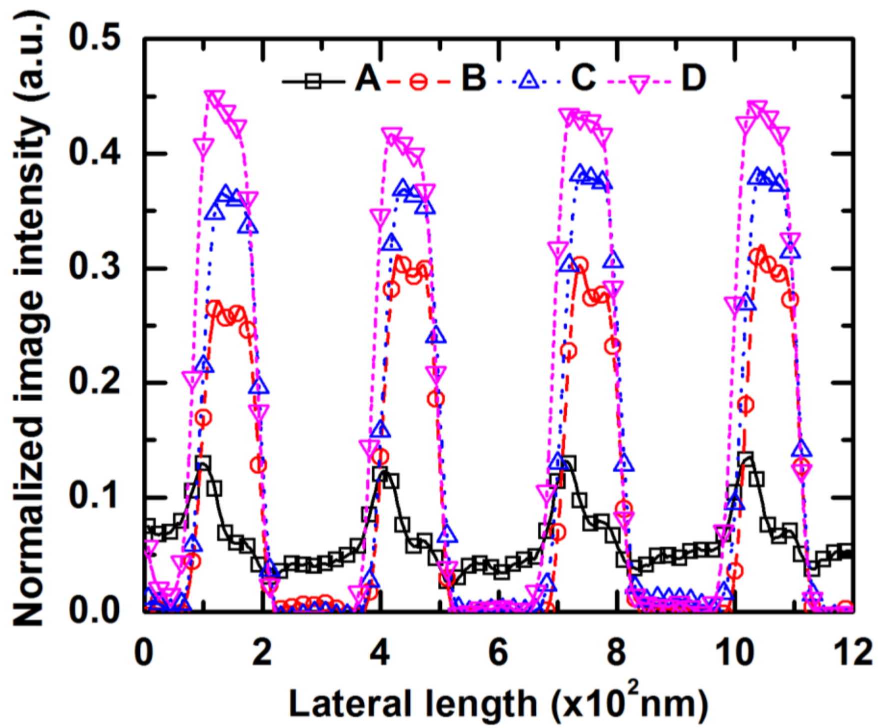

Figure 3.2 Effect of electron beam dose Q on the patterned dot profiles. Top-view field-emission SEM images acquired from a GaAs(111)B wafer patterned using EBL with dots of size D = 100

nm and inter-dot spacing S = 150 nm as a function of Q = a) 220 μC/cm^2, b) 295 μC/cm^2, c) 460 μC/cm^2, and d) 535 μC/cm^2. Scale bar in all the images is 500 nm. The plot shows spatial variations in the SEM image intensities of the patterns in a)-d) normalized with respect to the back ground intensity. Each of the curves is an average of over 128 line profiles acquired from the patterned regions.

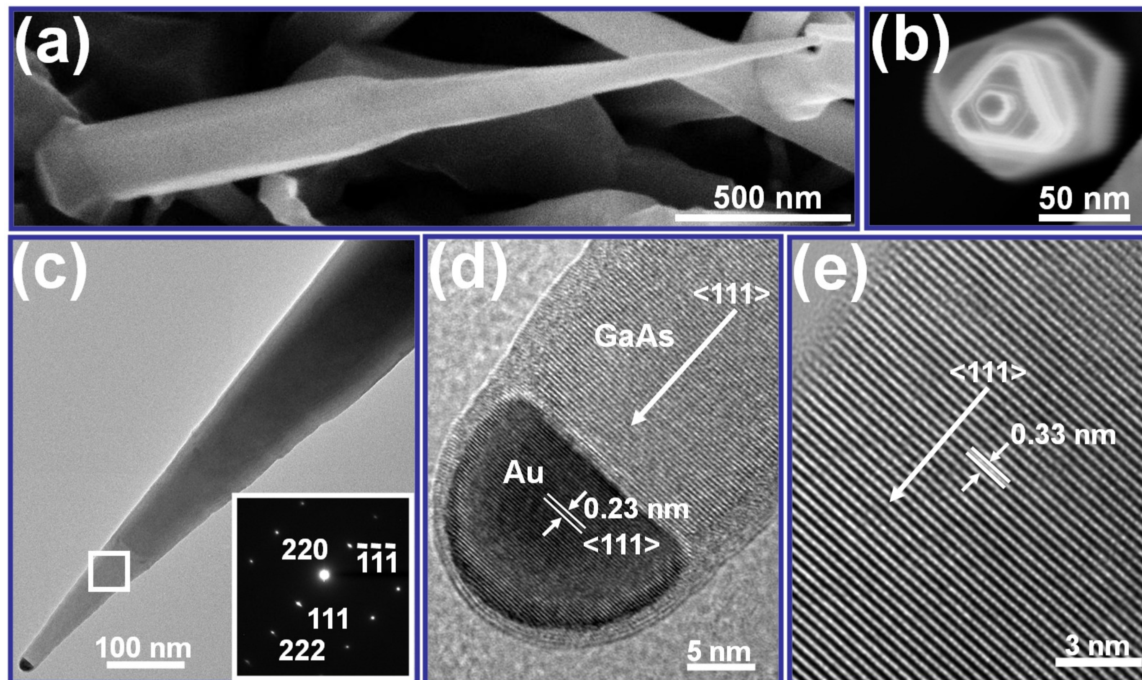

Figure 3.3 (a) 30°-tilted SEM image of a GaAs nanowire grown in the area containing Au dots of size D = 150 nm, and spacing S = 150 nm patterned using Q = 505 μC/cm^2. (b) Top view SEM image of the same nanowire. (c) Bright-field TEM image of a GaAs nanowire grown in the area prepared using Q = 525 μC/cm^2, D = 150 nm, and S = 150 nm. Inset is a selected area electron diffraction pattern acquired along the [112] zone axis from the region highlighted in the image. The diffraction data indicates that the wire is zinc blende in structure and the growth direction is ⟨111⟩. (d,e) Higher resolution TEM images of the catalyst tip-wire interface and GaAs nanowire, respectively.

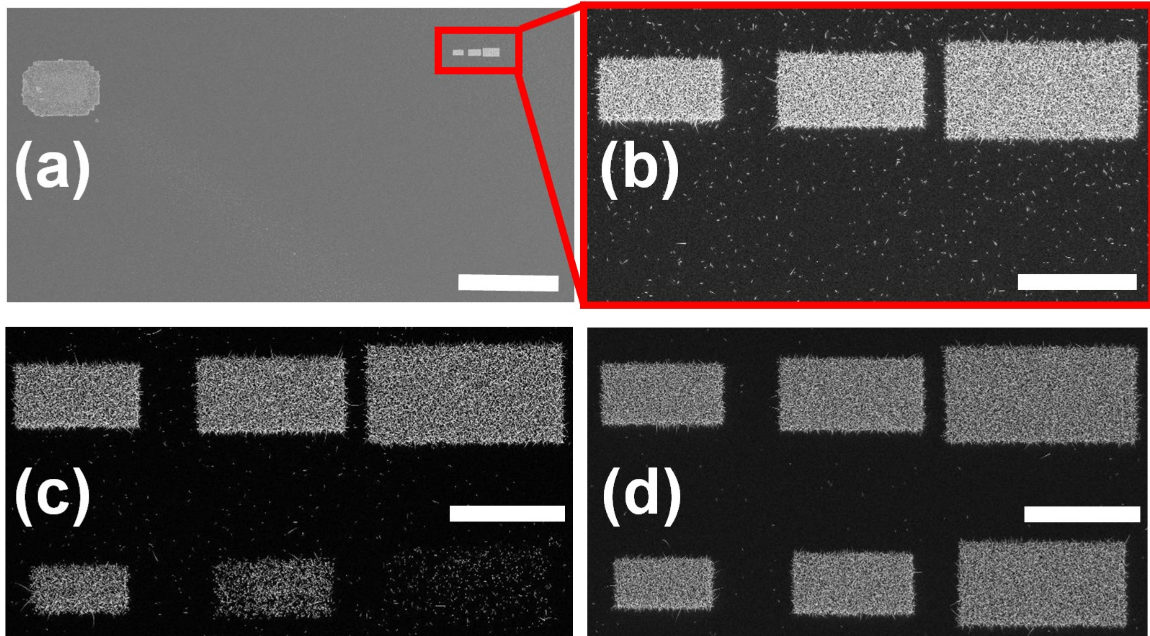

Figure 3.4 Top-view SEM image obtained from the patterned GaAs(111)B wafer after the growth of GaAs nanowires. a) Low-magnification SEM image of the region containing the pattern prepared using Q = 355 μC/cm^2, highlighted by red square. The scale bar is 0.5 mm. (b) Higher magnification SEM image of the red rectangular region in (a). (c,d) SEM images of the areas patterned using Q = (c) 400 μC/cm^2 and (d) 520 μC/cm^2. In the images (b)-(d), scale bar is 50 μm. All the dots in a given row have the same size D = 150 nm (top row) and 100 nm (bottom row), while S is 100 nm, 150, and 250 nm in the left, center, and the right patterns, respectively.

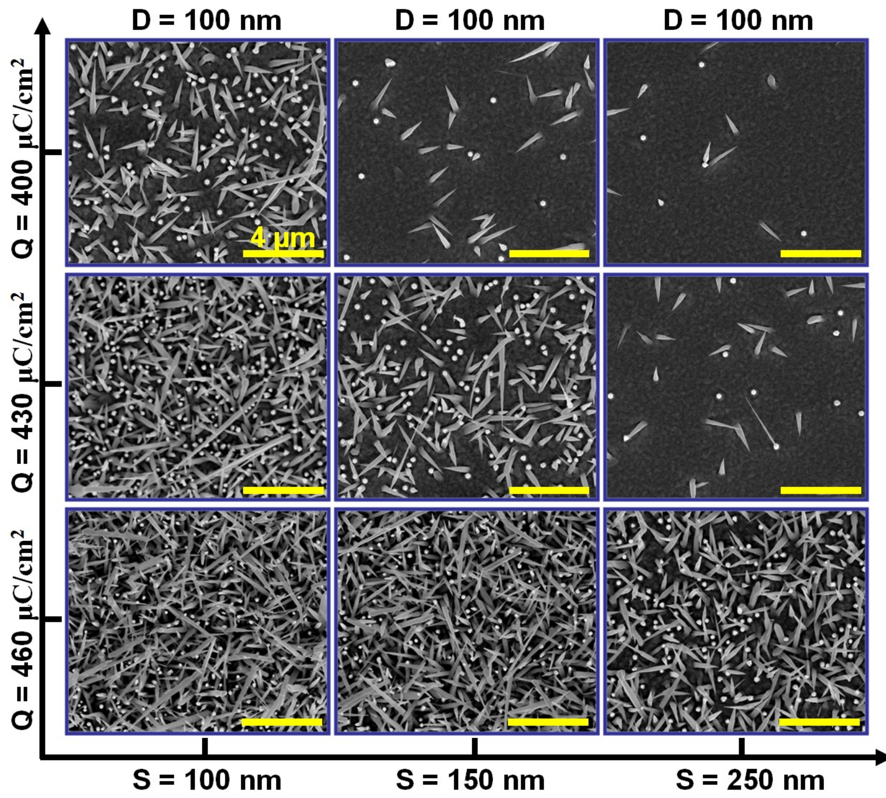

Figure 3.5 SEM images of a GaAs(111)B wafer with GaAs nanowires grown in the areas patterned with Au dots of size D = 100 nm. The vertical and horizontal axes show patterns obtained using different Q and S values, respectively. Scale bars in the images are 4 μm.

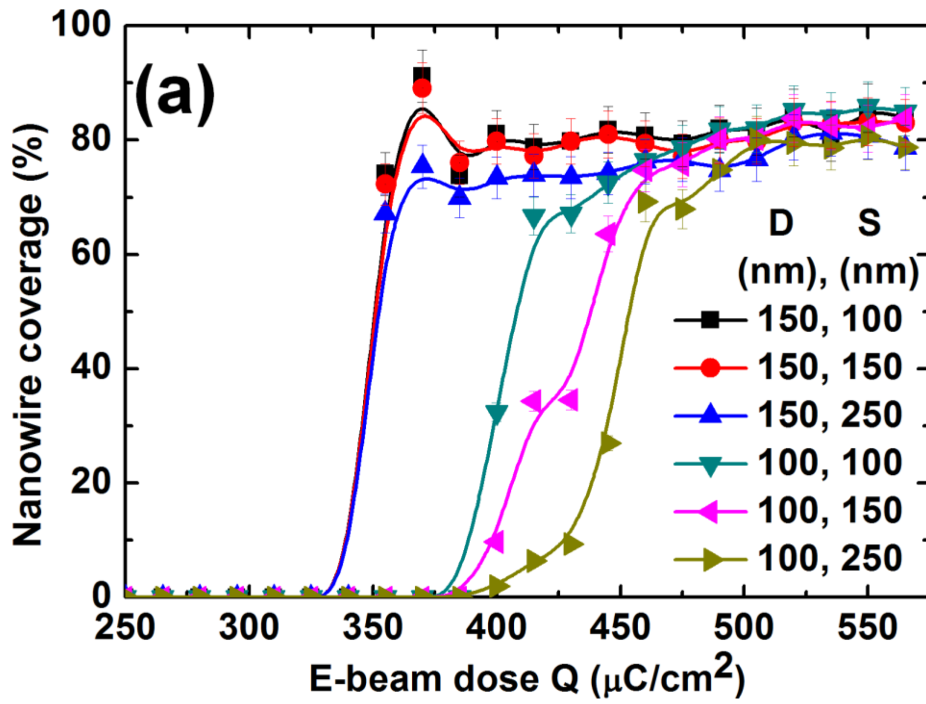

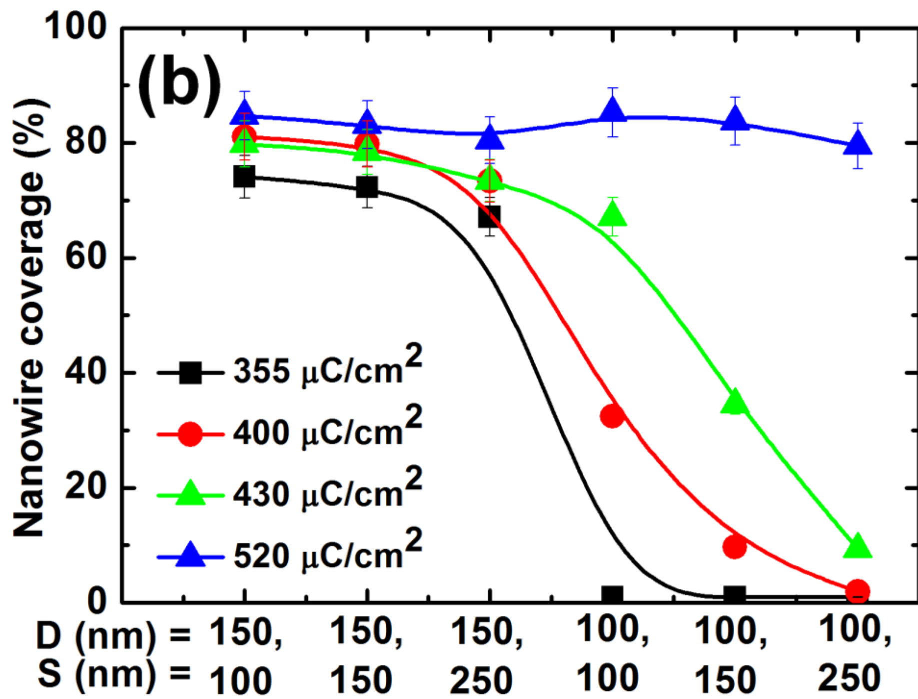

Figure 3.6 The fractional surface density of nanowires plotted as a function of (a) Q and (b) D and S. Solid lines are a guide for the eye.

References

[1] M. T. Bjork, C. Thelander, A. E. Hansen, L. E. Jensen, M. W. Larsson, L. R. Wallenberg, and L. Samuelson, Nano Lett. 4, 1621 (2004).

[2] E. P. A. M. Bakkers, M. T. Borgström, and M. A. Verheijen, MRS Bulletin 32, 117 (2007).

[3] X. Y. Bao, C. Soci, D. Susac, J. Bratvold, D. Aplin, W. Wei, C. Y. Chen, S. Dayeh, K. Kavanagh, and D. Wang, Nano Lett.. 8, 3755 (2008).

[4] L. Gao, R. L. Woo, B. Liang, M. Pozuelo, S. Prikhodko, M. Jackson, N. Goel, M. K. Hudait, D. L. Huffaker, M. S. Goorsky, S. Kodambaka, and R. F. Hicks, Nano Lett. 9, 2223 (2009).

[5] Z. H. Wu, X. Y. Mei, D. Kim, M. Blumin, H. E. Ruda, Appl. Phys. Lett. 81, 5177 (2002).

[6] M. J. Bierman, Y. K. A. Lau, A. V. Kvit, A. L. Schmitt, and S. Jin, Science 320, 1060 (2008).

[7] R. S. Wagner, W. C. Ellis, Appl. Phys. Lett. 4, 89 (1964).

[8] M. T. Borgström, G. Immink, B. Ketelaars, R. Algra and E. P.A.M. Bakkers, Nature Nanotechnology 2, 541 (2007).

[9] Z. Fan, J. C. Ho, Z. A. Jacobson, R. Yerushalmi, R. L. Alley, H. Razavi, and A. Javey, Nano Lett. 8, 20 (2008).

[10] K. Tomioka, J. Motohisa, S. Hara, and T. Fukui, Nano Lett. 8, 3475 (2008).

[11] Y. Wei, W. Wu, R. Guo, D. Yuan, S. Das, and Z. L. Wang, Nano Lett. 10, 3414 (2010).

[12] L. E. Jensen, M. T. Björk, S. Jeppesen, A. I. Persson, B. J. Ohlsson, and L. Samuelson, Nano Lett. 4, 1961 (2004).

[13] M. D. Abramoff, P. J. Magelhaes, and S. J. Ram, Biophotonics International 11, 36 (2004).

[14] Y. Du, S. Han, W. Jin, C. Zhou, and A. F. J. Levi, Appl. Phys. Lett. 83, 996 (2003).

[15] S. Babin, K. Bay, and J. J. Hwu, J. Vac. Sci. Technol. B, 28, C6H1 (2010).

[16] Y. Kita, Y. Kasai, S. Hashimoto, K. Iiyama, and S. Takamiya, Jpn. J. Appl. Phys. 40, 5861 (2001).

[17] S. Yasin, M. N. Khalid, D. G. Hasko, S. Sarfraz, Microelectron. Eng. 78/79, 484 (2005).

[18] J. Kretz, L. Dreeskornfeld, G. Ilicali, T. Lutz, and W. Weber, Microelectron. Eng. 78/79, 479 (2005).

[19] F.P. Gibbons, J. Manyam, S. Diegoli, M. Manickam, J.A. Preece, R.E. Palmer, and A.P.G. Robinso, Microelectron. Eng. 85, 764 (2008).

[20] A. E. Grigorescu and C. W. Hagen, Nanotechnology 20, 292001 (2009).

[21] J. C. Harmand, G. Patriarche, Péré-Laperne, M-N. Mérat-Combes, L. Travers, and F. Glas, Appl. Phys. Lett. 87, 203101 (2005).

[22] S. O. Mariager, S. L. Lauridsen, C. B. Sørensen, A. Dohn, P. R. Willmott, J. Nygård, and Robert Feidenhans'l, Nanotechnology 21, 115603 (2010).

[23] A. A. Bonapasta and F. Buda, Phys. Rev. B 65, 045308 (2002).

[24] J. B. Hannon, S. Kodambaka, F.M. Ross, and R. M. Tromp, Nature 440, 69 (2006).

[25] J. Tersoff, D. E. Jesson, and W. X. Tang, Science 324, 236 (2009).

[26] T.A. Bryantseva, D.V. Lioubtchenko, and V.V. Lopatin, Appl. Surf. Sci. 100/101, 169 (1996).

[27] M. Tchernycheva, J. C. Harmand, G. Patriarche, L. Travers, and G. E. Cirlin, Nanotechnology 17, 4025 (2006).

[28] V. G. Dubrovskii, I. P. Soshnikov, G. E. Cirlin, A. A. Tonkikh, Yu. B. Samsonenko, N. V. Sibirev, and V. M. Ustinov, Phys. Status Solidi B 241, R30 (2004).

[29] S. Kodambaka, J. Tersoff, M. C. Reuter and F. M. Ross, Science 316, 729 (2007).

[30] A. I. Persson, M. W. Larsson, S. Stenström, B. J. Ohlsson, L. Samuelson, and L. R. Wallenberg, Nature Mater. 3, 677 (2004).

[31] ICDD-JCPDS Catalogue No. 32-0389.

[32] T. H. P. Chang, J. Vac. Sci. Technol. 12, 1271 (1975).

CHAPTER 4

RAMAN SPECTROSCOPIC STUDIES ON SEMICONDUCTOR GaAs NANOWIRE BUNDLES

4. 1 Introduction

Gallium Arsenide (GaAs) has been widely studied owing to a direct band gap semiconductor with high carrier mobility [1] and potential application of electro-optic devices [2]. The vapor-liquid-solid (VLS) growth method is the most commonly used technique in which a metal acts as a catalyst for preferential nucleation and growth of nanowires [3]. Since the optical and electrical performances of GaAs nanowire based devices are strongly affected by their crystal structures, sizes, and shapes [4], extensive detailed studies have been made to realize controlled VLS grown GaAs nanowires [5,6]. For instance, nanowire morphology dependent on Raman scattering effect such as phonon confinement [7], surface optical phonon mode [8], and aspect ratio of length over diameter [9] has been actively studied for single crystalline GaAs nanowires. However, most studies have been focused on optical characterization of individual nanowire, and very little is known concerning micro Raman spectroscopic studies of GaAs nanowire bundles. In this paper, the dependence of Raman scattering modes on the growth conditions and morphology of GaAs nanowire bundles has been studied.

4.2 Experimental Details

GaAs nanowires were synthesized via the VLS growth mechanism based on a solid-source molecular beam epitaxy technique. Detailed growth conditions were described in chapter 3 and elsewhere [10]. The nanowire morphologies were investigated by a scanning electron

microcopy (SEM, FEI Nova 600 FIB/SEM). Raman spectra were performed in a conventional backscattering geometry with Renishaw 1000 micro-Raman spectrometer using an argon laser (514 nm) as an excitation source. The laser output power was 5 mW with a spot size of 1 μm and a spatial resolution of 0.5 cm^{-1}. All spectra were collected in ambient conditions at room temperature, and are calibrated to the reference Si peak arising from a reference substrate (520.1 cm^{-1}).

4.3 Results and Discussion

Figure 4.1 shows SEM images of Au patterned GaAs(111)B substrate. There were thirty-one rows of nano-scale dots patterned by e-beam lithography at 50 keV. Each pattern was made up of 250 × 150 ordered arrays of dots which have identical nominal sizes of 100nm and 150nm with inter-dot spacings of 100 nm and 150 nm, respectively. As increasing the e-beam dose from 145 $\mu C/cm^2$ to 595 $\mu C/cm^2$, with which the rows are patterned, the Au disk boundaries of the nano-patterns gradually become clear in which more amount of Au is deposited into the GaAs(111)B substrate as a catalyst layer. In our experiment, it is noted that GaAs nanowires are randomly oriented rather than vertically aligned due to large variations in Au-Ga catalyst [11], catalyst migration of Au [12,13] or Ga [14,15], and relatively lower growth temperature [16].

Figure 4.2a shows the surface coverage changes of Au catalyzed GaAs nanowires, evaluated from 100 nm and 150 nm patterning conditions, respectively. Due to random growth orientation of GaAs nanowires, the fractional coverage of nanowires rather than the number density of nanowires were utilized [17]. As the e-beam dose increases, the surface coverage of GaAs nanowires for both given patterns rapidly increases, and it is saturated at a rate of ~ 80%. It is noted that such nanowires do not likely to grown with an e-beam dose of 355 $\mu C/cm^2$.

Furthermore, it is also clear that nanowires with smaller size (100 nm) require higher threshold dose, and nanowires with larger patterning size (150 nm) shows more stiff increase than smaller one (100 nm), implying that there is an optimum condition of the e-beam dose to enable the reliable growth of GaAs nanowires.

Figure 4.2b shows the average base diameter changes of as-grown nanowires that were measured from multiple SEM investigations. In this figure, the obtained data was fitted to a log-normal distribution [18], and then their average diameters were calculated from the fitted slope. In this experiment, it is believe that upon annealing samples at 480 ^{o}C for 10 min, deposited gold patterns form into a condition of Au-Ga eutectic droplets with a broad size distribution in which either Ga or Au adatom can migrate with a mean diffusion length of 3 μm [19]. It can be found that multiple nanowires grown from a single window results in an irregular shape [20]. It was also found that their shapes were highly tapered along with most of their length, and they have larger base diameters than the original pattern sizes i.e., 100 nm or 150 nm, indicating that the lateral growth should induce the increase of base diameter [19]. On the other hand, with increasing the e-beam dose, the nanowire base diameter decreases for both cases. As a result, the cross-over takes place at the e-beam dose of 480 μC/cm^2.

Figure 4.3 depicts the average aspect ratio for GaAs nanowires α, which is the nanowire length over base diameter, as a function of e-beam doses ranging from 250 μC/cm^2 to 600 μC/cm^2. More than N = 50 nanowires were investigated, and then α was estimated from each pattern condition using a formula, $\alpha = {}^{1}\!/_{N}\sum_{i=1}^{N}(L_i / D_i)$, where L, D, and N are the length, base diameter, and sampling numbers of nanowires, respectively. In the case of 150 nm pattern, the aspect ratio appeared to be independent when e-beam dose is above 300 μC/cm^2 and its values of the nanowires evaluated to be 22 ~ 26. However, the aspect ratio of the pattern condition of 100

nm was strongly dependent upon the e-beam dose. Interestingly, with the e-beam doses between 350 and 525 μC/cm^2, the average aspect ratio was linearly increased up to the value of about 25. This observation can be explained by critical catalyst size effect [21,22], and our results are consistent with the others [23].

We measured Raman spectra nanowires bundles to investigate the inelastic scattering of monochromatic radiation as shown in Fig. 4.4. The unpolarized Raman spectra from GaAs nanowire bundles for various e-beam exposures and pattern conditions were recorded. It is noted that the two measured Raman spectra from 175 μC/cm^2 in Fig. 4.4a and 250 μC/cm^2 in Fig. 4.4b, exhibit two clear peaks in which the peak position at 268.7 cm^{-1} is responsible for the transverse optical (TO) phonon and the one positioned at 292 cm^{-1} is due to scattering from the longitudinal optical (LO) phonon. It was identified that the peak positions obtained in this experiment are exactly matched to those of the TO and LO measured from a bulk GaAs(111)B substrate, implying that lower e-beam dose below 170 μC/cm^2 and 250 μC/cm^2 could not provide a condition for the growth of GaAs nanowires.

In the presence of GaAs nanowires, it is clear that both LO and TO bands are broadened and shifted considerably toward lower wave numbers relative to those of bulk crystalline GaAs. For e-beam doses of 355, 400, and 520 μC/cm^2, the TO and LO positions, measured with the presence of the nanowires, appear at near 265 cm^{-1} and 286 cm^{-1}, respectively as shown in Fig. 4.4. It was identified that the phonon peaks exhibit a considerable asymmetry as compared with the bulk phonons from the area at which nanowires does not exist, i.e. the bulk substrate. We believe that this red-shift in Raman scattering observation is mainly attributed to the size and shape effect of nanowire bundles [24]. Previously, Shi *et al.*[25] reported that a down-shift of GaAs nanowire is involved in structural defects or residual stress. Mahan *et al.* also observed

slightly down-shifted and high asymmetric Raman spectra from GaAs nanowire due to the very high aspect ratio of the nanowires which influences the long-range dipolar interaction [9]. Random alignment of GaAs nanowires could also be one of possible reasons that cause the broadening and asymmetric effects of Raman spectra [26]. Random orientation of nanowires in which the incident photons interact with various facets of nanowires can alter Raman spectra from those of bulk GaAs.

On the other hand, in the Raman spectra measurement, one additional peak appeared below the main peak centered at 258 cm^{-1}. It was identified that the appearance of this spectra could be due to the presence of arsenic anti-site defects [27], or the existence of twins in the structure of nanowires [8]. Arsenic anti-site peaks cause a reduction in the electric field associated with the LO phonon and is observable from low-temperature grown GaAs samples [28]. In addition, for nanowires with higher exposed e-beam doses, the Raman curve appeared as a small shoulder on the lower frequency side of the TO Peak. However, for nanowires with small e-beam doses, showing a smaller aspect ratio as shown in Fig. 4.3, the anti-site peak can be clearly distinguished and its intensity also increases. These Raman behaviors in the nanowires further prove that the Raman peak located at the shoulder of the TO are indeed attributed to scattering from either high twin density region in the nanowire or defect site.

Figure 4.5 shows the intensity variations of TO and LO phonon peaks as a function of electron beam dose for pattern condition of 100 nm and 150 nm, respectively. It is noted that the recorded spectra were deconvoluted using the combination of Gaussian and Lorentzian functions to deduce the Raman wave numbers, line-widths and intensities. As increasing the e-beam dose, two distinct behaviors of the TO and LO modes was identified that also depends on the choice of pattern conditions. In case of the pattern condition of 150 nm wide, it was noticed that the

measured absolute intensity variations in both the TO and LO phonon modes are found to be independent from the e-beam dose condition. In this case, the surface coverage and aspect ratio of nanowires are closely matched to the saturated values as shown in Fig. 4.2a. On the other hand, in the case of smaller pattern of 100 nm wide, it was also noticed that monotonic increase behavior of both the TO and LO phonon modes with increasing the e-beam dose are observed, in agreement with the surface coverage and aspect ratio changes of nanowires. In Fig. 4.5b, there is a cross-over point between 100 nm and 150 nm patterns that occurs with the e-beam dose of 475 $\mu C/cm^2$. This behavior is similar to the cross-over point of the base diameter change in Fig. 4.2b. As a result, we believe that this trend indicates the shape effect to be the dominant factor of those Raman bands [9,29].

4.4 Conclusion

In conclusion, we have experimentally shown that Raman spectra were dependent on initial pattern sizes (100 nm and 150 nm) and thickness of Au layers by varying e-beam dose. Our study reveals that ensembles of micron-size and single crystalline GaAs nanowires exhibit a downshifted and asymmetric broadening of the Raman first order TO and LO phonon peaks relative to bulk modes. Additionally, arsenic anti-site peaks were only found from GaAs nanowires, implying that causes a reduction in the electric field associated with the LO phonon. The initial catalyst thickness and pattering size are strongly related to overall nanowire morphology variations, i.e. base diameter, shapes, and densities, resulting in strong dependence of Raman spectra. The present understanding of the Raman spectroscopy on the nanowire bundles would benefit the design and development of GaAs nanoscale optoelectronic devices.

Figures

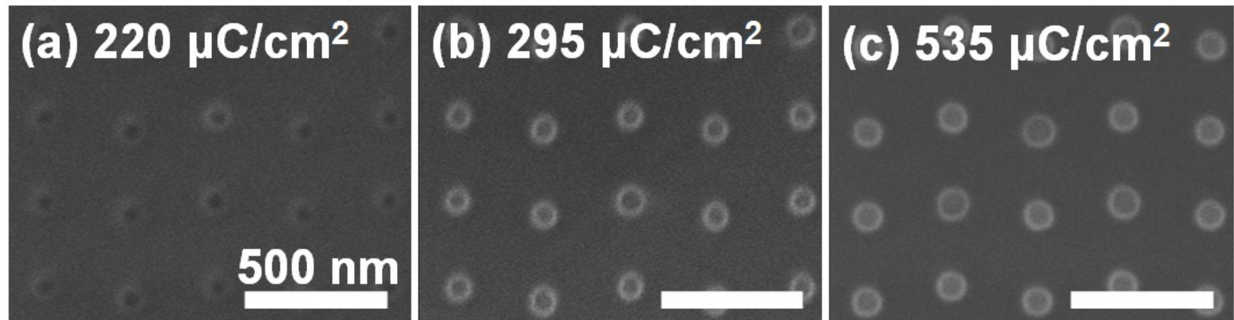

Figure 4.1 SEM images of the Au patterned GaAs (111)B substrates with e-beam dose (a) 220 $\mu C/cm^2$, (b) 295 $\mu C/cm^2$, and (c) 535 $\mu C/cm^2$.

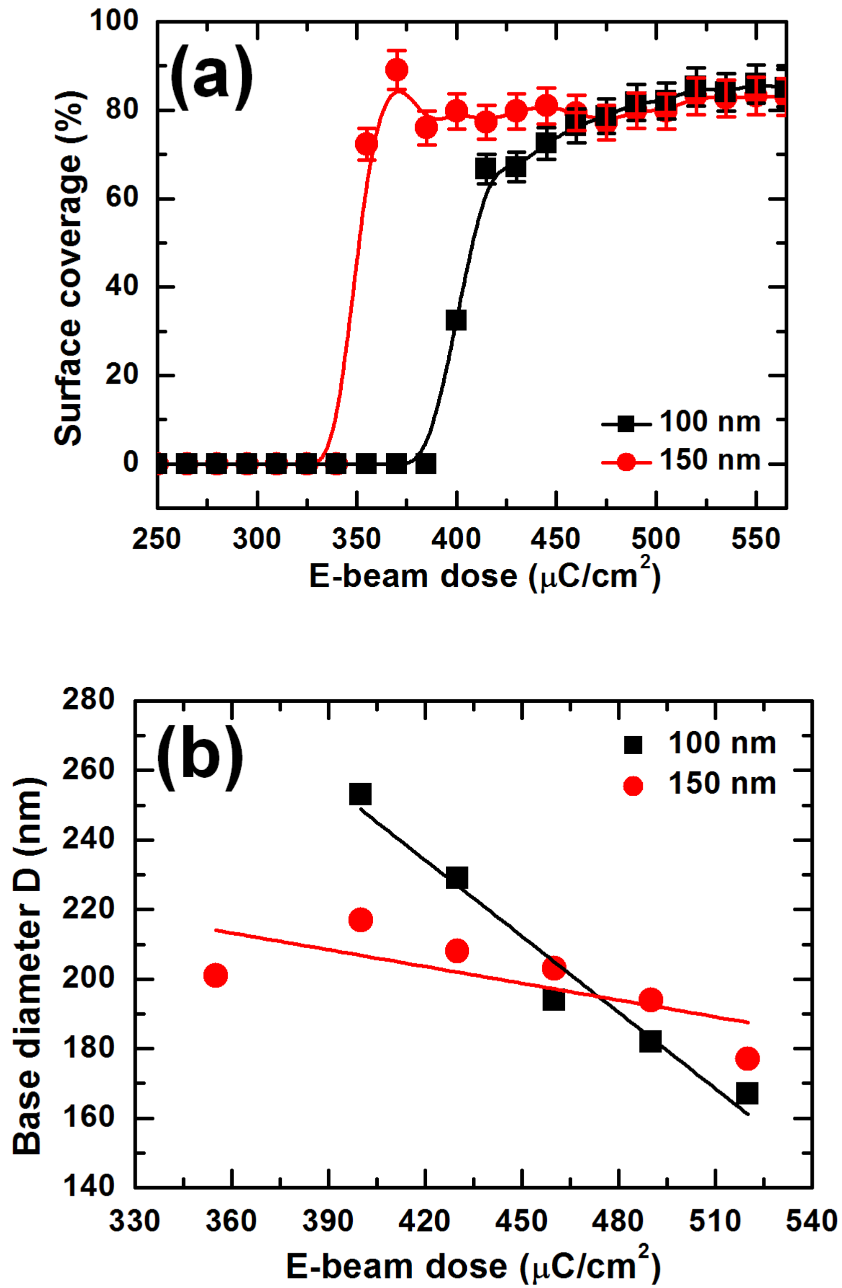

Figure 4.2 (a) Surface coverage and (b) average base diameter changes of GaAs nanowire bundles as a function of electron beam dose.

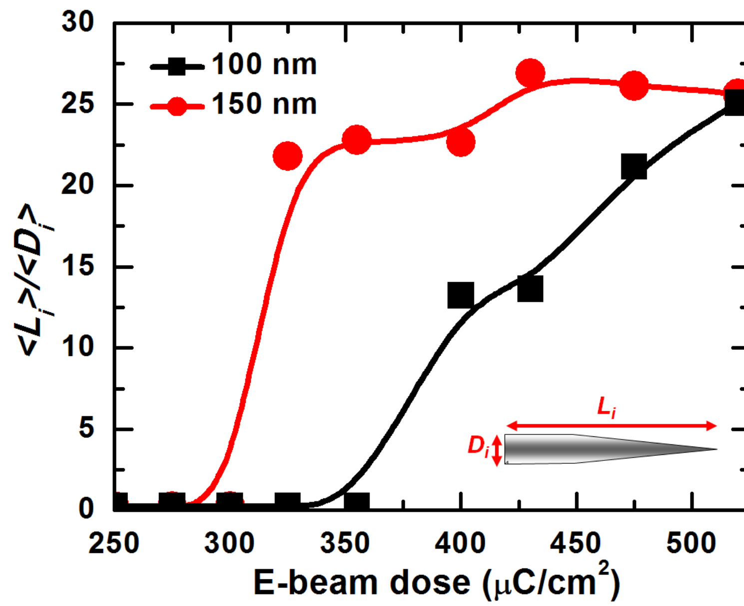

Figure 4.3 The aspect ratio of GaAs nanowires for different e-beam doses.

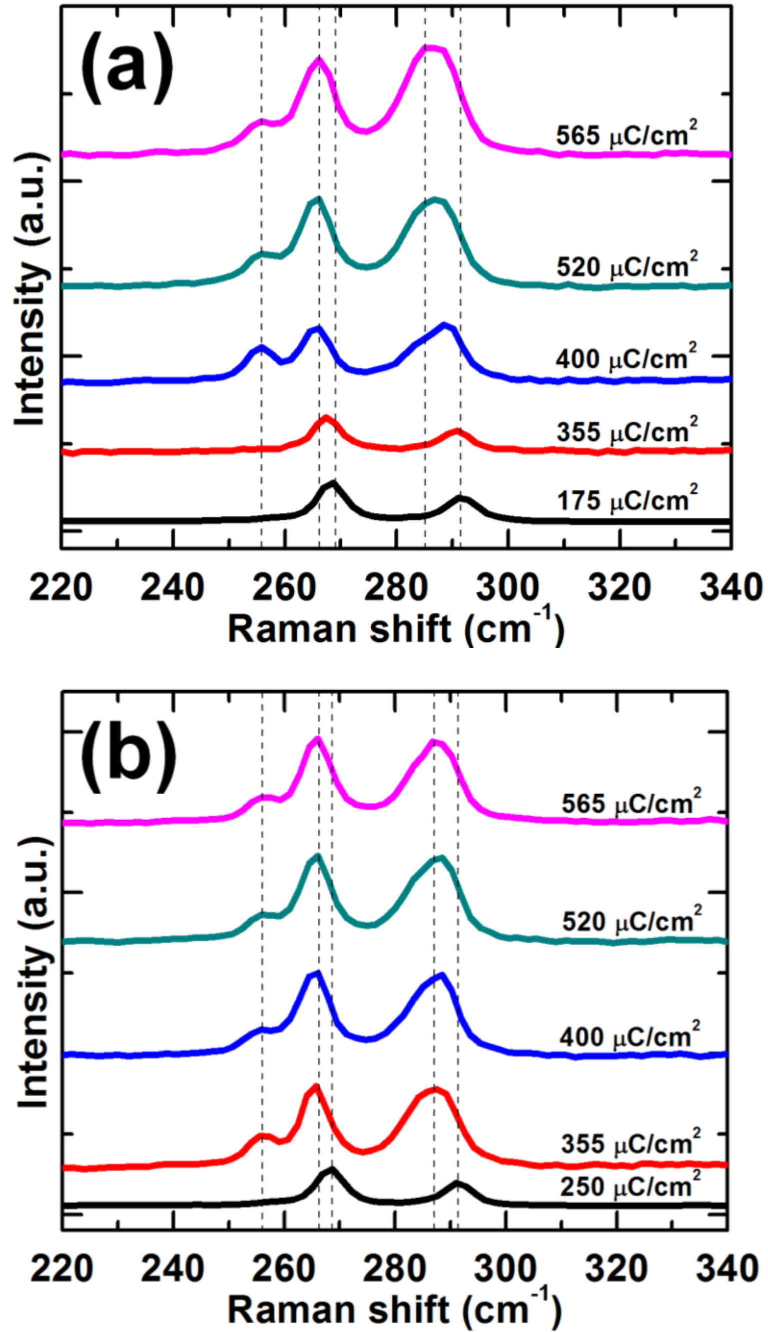

Figure 4.4 Raman spectra of GaAs nanowire bundles as a function of electron beam dose for the pattering size of (a) 100 nm and (b) 150 nm.

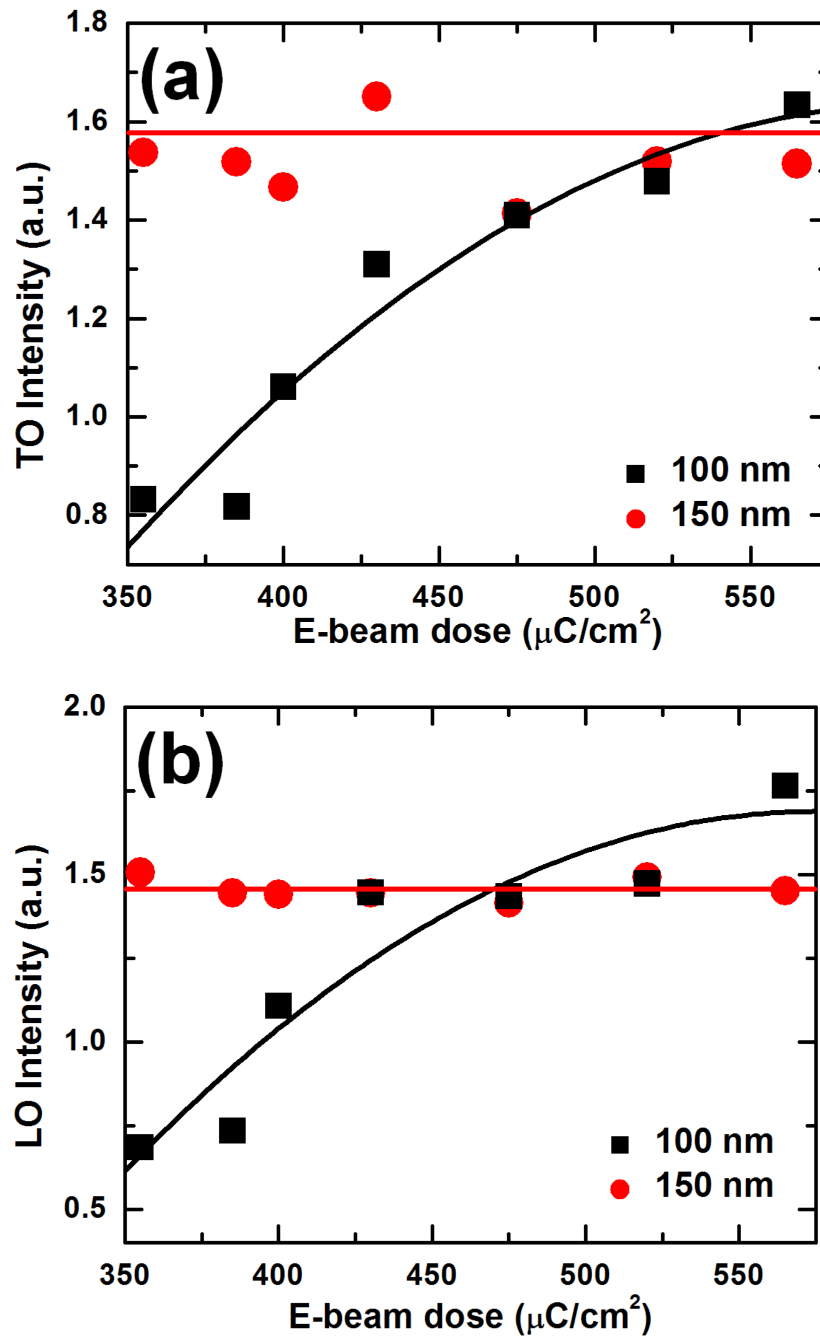

Figure 4.5 Intensity changes of (a) transverse optical and (b) longitudinal optical phonon modes as a function of electron-beam dose for 100 nm & 150 nm patterns.

References

[1] X. Duan, J. Wang, C. M. Lieber, Appl. Phys. Lett. 76, 1116 (2000).

[2] V. Schmidt, H. Riel, S. Senz, S. Karg, W. Riess, and U. Goesle, Small 2, 85 (2006).

[3] R. S. Wagner and W. C. Ellis, Appl. Phys. Lett. 4, 89 (1964).

[4] C. Soci, X.-Y. Bao, D. P. R. Aplin, and D. Wang, Nano Lett. 8, 4275 (2008).

[5] H. Shtrikman, R. Popovitz-Biro, A. Kretinin, and M. Heiblum, Nano Lett. 9, 215 (2009).

[6] K. A. Dick, P. Caroff, J. Bolinsson, M. E. Messing, J. Johansson, K. Deppert, L. R. Wallenberg, and L. Samuelson, Semicond. Sci. Technol. 25, 024009 (2010).

[7] N. Begum, A. S. Bhatti, F. Jabeen, S. Rubini, and F. Martelli (2010). Phonon Confinement Effect in III-V Nanowires, Nanowires, Paola Prete (Ed.), ISBN: 978-953-7619-79-4. Available from: http://www.intechopen.com/articles/show/title/phonon-confinement-effect-in-iii-v-nanowires.

[8] D. Spirkoska, G. Abstreiter, and A. Fontcuberta i Morral, Nanotechnology 19, 435704 (2008).

[9] G. D. Mahan, R. Gupta, Q. Xiong, C. K. Adu, and P. C. Eklund, Phys. Rev. B 68, 073402 (2003).

[10] J. H. Park, S. Prikhodko, M. Pozuelo, V. Gambin, and S. Kodambaka, submitted for review (2012).

[11] S. O. Mariager, S. L. Lauridsen, C. B. Sørensen, A. Dohn, P. R. Willmott, J. Nygård, and Robert Feidenhans'l, Nanotechnology 21, 115603 (2010).

[12] A. A. Bonapasta and F. Buda, Phys. Rev. B 65, 045308 (2002).

[13] J. B. Hannon, S. Kodambaka, F.M. Ross, and R. M. Tromp, Nature 440, 69 (2006).

[14] J. Tersoff, D. E. Jesson, and W. X. Tang, Science 324, 236 (2009).

[15] T.A. Bryantseva, D.V. Lioubtchenko, and V.V. Lopatin, Appl. Surf. Sci. 100/101, 169 (1996).

[16] M. Tchernycheva, J. C. Harmand, G. Patriarche, L. Travers, and G. E. Cirlin, Nanotechnology 17, 4025 (2006).

[17] Y. Du, S. Han, W. Jin, C. Zhou, and A. F. J. Levi, Appl. Phys. Lett. 83, 996 (2003).

[18] Q. Xiong, R. Gupta, K. W. Adu., E. C. Dickey, G. D. Lian, D. Tham, J. E. Fischer, and P. C. Eklund, J. Nanosci. Nanotech. 3, 335 (2003).

[19] J. C. Harmand, G. Patriarche, Péré-Laperne, M-N. Mérat-Combes, L. Travers, and F. Glas, Appl. Phys. Lett. 87, 203101 (2005).

[20] P. Mohan, R. Bag, S. Singh, A. Kumar, and R. Tyagi, Nanotechnology 23, 025601 (2012).

[21] T. Yanagida, K. Nagashima, H. Tanaka, and T. Kawai, J. Appl. Phys. 104, 016101 (2008).

[22] C. Soci, X.-Y. Bao, D. P. R. Aplin, and D. Wang, Nano Lett. 8, 4275 (2008).

[23] M. T. Borgström, G. Immink, B. Ketelaars, R. Algra, and E. P.A.M. Bakkers, Nature Nanotechol. 2, 541 (2007).

[24] I. H. Campbell and P. M. Fauchet, Solid State Commun. 58, 739 (1986).

[25] W. S. Shi, Y. F. Zheng, N. Wang, C. S. Lee, and S. T. Lee, Appl. Phys. Lett. 78, 3304 (2001).

[26] A. J. Lohn, T. Onishi, N. P. Kobayashi, Nanotechnology 21, 355702 (2010).

[27] M. Touffela, P. Puech, R. Carles, E. Beddel, C. Fontaine, A. Claverie, and G. Benassyag, J. Appl. Phys. 85, 2929 (1999).

[28] T. A. Gant, H. Shen, J. R. Flemish, L. Fotiadis, and M. Dutta, Appl. Phys. Lett. 60, 1453 (1992).

[29] J.-A. Huang, Y.-Q. Zhao, X.-J. Zhang, L.-B. Luo, Y.-K. Liu, J. A. Zapien, C. Surya, and S.-T. Lee, Appl. Phys. Lett. 98, 183108 (2011).

CHAPTER 5

DENSITY AND DIAMTETER DEPENDENT SURFACE OPTICAL PHONON MODE CHANGES IN GaAs NANOWIRE ARRAYS

5.1 Introduction

One-dimensional structures represent interesting physical phenomena with unique geometry arising from quantum confinement and the large surface-to-volume ratio [1,2]. Comparative studies of Raman scattering experiments between bulk and nanostructure materials have been extensively examined [3,4]. The enhancement of Raman scattering intensity from nanostructure materials is reported to the count part of bulk materials [5]. The highly anisotropic shape of nanowire has shown the angular dependencies of the phonon modes [6]. The breaking crystal symmetry of nanowires leads to unexpected results from selection rule; it is known as surface phonon mode [7]. Surface phonon mode can be activated by the presence of roughness, saw tooth faceting on the nanowire sidewall, or a diameter oscillation along the nanowire [8]. The surface optic (SO) phonon modes are blue shifted with the increase of dielectric constant of the surrounding medium [9], and the decrease with the nanowire diameter [10]. The frequency of the SO modes at Γ point appears at those of between E1(LO) and E1(TO) and the long-range dipolar interaction gives rise to an additional SO splitting of the TO and LO mode in a large aspect ratio [11]. Raman spectroscopy is a useful tool to provide qualitative information from nanostructure semiconductor by probing SO modes due to comparably weak interaction of photons with medium [12].

In this chapter, we present a systematic study of SO modes of GaAs nanowires as function of NW density and diameters by means of micro Raman spectroscopy. The strong

downshift and splitting of SO modes from first order phonon peaks are observed. The dielectric continuum model is employed to interpret observed SO phenomena. From the comparison between isolated nanowire with various diameters and dielectric function approximation with various nanowire densities, it is found that dielectric function approximation can provide a better insight to understand the downshift and splitting of SO modes in GaAs nanowires. The optical anisotropy and strong polarity of GaAs nanowires favor the dipolar coupling of neighboring nanowires and result in the spitting of the SO modes.

5.2 Experimental Details

GaAs nanowires were synthesized via the VLS growth mechanism based on a solid-source molecular beam epitaxy technique. Detailed growth conditions were described elsewhere [13]. Catalyst patterning conditions with e-beam dose variations are included in Fig. S1. The base diameter and density of nanowires were investigated by a scanning electron microcopy (SEM, FEI Nova 600 FIB/SEM). Raman spectra were performed in a conventional backscattering geometry with Renishaw 1000 micro-Raman spectrometer using an argon laser (514 nm) as an excitation source. The laser output power was 5 mW with a spot size of 1 μm and a spatial resolution of 0.5 cm^{-1}. All spectra were collected in ambient conditions at room temperature, and are calibrated to the reference Si peak arising from a reference substrate (520.1 cm^{-1}).

5.3 Results and Discussion

Figure 5.1 shows SEM images of Au catalyzed GaAs nanowires grown on GaAs(111)B substrate. There were thirty-one rows of nano-scale dots patterned by e-beam lithography at 50

keV. Each pattern was made up of 250×150 ordered arrays of dots which have identical nominal sizes of 100nm with inter-dot spacings of 150 nm. As increasing the e-beam dose Q from 145 $\mu C/cm^2$ to 595 $\mu C/cm^2$, nanowire size and density increases. Detailed statistical studies of base diameter and fill factor of nanowires for different Qs will be compared to the frequency of SO phonon modes. The fill factor, as known as coverage, determines the relative concentration of nanowires over the substrate [14].

Figure 5.2 shows the density change of GaAs nanowires. The nanowire density increase linearly from 380 $\mu C/cm^2$ to 475 $\mu C/ cm^2$ and then is saturated at a rate of ~ 80%. When the e-beam dose is smaller than 380 $\mu C/cm^2$, very low densities of nanowires are observed with fill factors as low as 0.05.

Figure 5.3 illustrates the micro Raman spectra as a function of electron beam dose. By analogy to bulk data, the spectra of GaAs nanowires exhibit strong scattering at the E_1(TO) and E_1(LO) modes allowed in backscattering geometry. From the nanowire samples ($Q > 385$ $\mu C/cm^2$), weak features related to forbidden E_{2h} are observed which may be attributed to crystal lattice disorder and to deviation from the true backscattering geometry. An additional feature in the nanowire spectrum, not seen in no-growth area, is observed due to surface optic phonon scattering. Clear peak shift and splitting between SO and E_1(LO) modes are observed in the spectra.

The peak position and line shapes in Raman-active SO phonon modes are known to be very sensitive to the real part of the dielectric function of the materials surrounded by the dielectric medium [7,9]. Crystal symmetry breaking and rough surface of nanowires give rise to SO phonon mode [9]. The SO phonon modes are found between E_1(TO) and E_1(LO) bands and appeared to be downshift with increasing e-beam dose. A dielectric continuum model for a

cylindrical wire was employed to understand the nanowire diameter contribution to the SO mode dispersion [15,16].

$$\omega_{SO} = \omega_{TO}\sqrt{\frac{\varepsilon_S+\rho\varepsilon_m}{\varepsilon_\infty+\rho\varepsilon_m}} \quad \cdots\cdots (1)$$

$$\rho = \frac{K_1\ (qr)I_0\ (qr)}{K_0\ (qr)I_1\ (qr)} \quad \cdots\cdots (2)$$

Here K_i and I_n are i and n kind modified Bessel functions, respectively. Raman spectroscopy was measured in ambient condition ($\varepsilon_m^{air} = 1$) at Room Temperature (300 K). For bulk GaAs (300 K), the frequencies of polar phonon modes are $\omega_{\mathrm{E1(TO)}} = 268.7\ \mathrm{cm^{-1}}$ and $\omega_{\mathrm{E1(LO)}} = 292.2\ \mathrm{cm^{-1}}$. The static and high frequency dielectric constants of GaAs are taken to be isotropic and equivalent to $\varepsilon_S = 12.9$, and $\varepsilon_\infty = 10.89$, respectively [17]. The equation (1) and (2) are modified using the following relationship: $q = 2k = \frac{4\pi n_{\mathrm{GaAs}}}{\lambda_{ex}}$, $\lambda_{ex} = 514\ \mathrm{nm}$, $d = 2r, n_{\mathrm{GaAs}} = 3.3$. Solutions of equation are indicative of the phonon dispersion relation (See Figure 5.S3).

Figure 5.4 shows the SO phonon dispersion considering various dielectric media which surround GaAs nanowires with $\varepsilon_m = 1, 2.5, 5, 7.5, 10, 15$. The SO mode frequency increases from $\omega_{\mathrm{E1(TO)}} = 268.7\ \mathrm{cm^{-1}}$ and reaches an almost constant value for diameter larger than 100 nm. A theoretical calculation is failed to reproduce the experimental trend because the measured SO frequencies are 5 ~ 6 $\mathrm{cm^{-1}}$ below the dielectric continuum model. The frequency shift of the SO mode depends strongly on the dielectric constant of surrounding medium (ε_m), rather than diameter of nanowires, suggesting that size effect of nanowires (diameter > 150 nm) is negligibly small to cause the frequency shift of the SO mode.

Here the effect of nanowire density f was examined using effective medium theory [18]. Taking into consideration of the optical anisotropy of GaAs nanowires, the effective dielectric function of E_1 vibration mode in the nanowire-air system is given by [19]:

$$\omega_{SO}^2(f) = \frac{(1-f)\varepsilon_\infty \omega_{E1(LO)}^2 + (1+f)\varepsilon_m \omega_{E1(TO)}^2}{(1-f)\varepsilon_\infty + (1+f)\varepsilon_m} \qquad (3)$$

Since GaAs is a uniaxial crystal, ordinary and extraordinary excitations exist. The excitations are dependent on the angle between exciting wave vector and the c-axis of GaAs bulk [20]. Mata *et al*. [19] found that ordinary phonon excitation occurs under the interactions between the wave vector of incoming wave and a component perpendicular to the c axis. In other words, SO Raman-active mode with E_1 symmetry will be provided when the wave vector component of the excitation to the c-axis is not zero. The evolution of SO frequencies with fill factor is shown in Fig. 5.5. With increasing *f*, its frequency decreases from $\omega_{\mathrm{LO}} = 292.2\ \mathrm{cm}^{-1}$ toward $\omega_{\mathrm{TO}} = 268.7\ \mathrm{cm}^{-1}$. The Raman measurement is performed at normal incidence, but the nanowires are not grown along <111> axis. Therefore, the wave vector of the exciting light will be mostly scattered with non-vertical component to the c-axis, showing that the intensity of E_1 symmetry component will present highest intensity with the presence of nanowires. The evolution of SO phonons with *f* explains that the dipolar interaction between neighboring nanowires, represented by the effective dielectric function, is the most relevant effect in the determination of SO frequencies. However, the discrepancy between theoretical calculation and experimental measurement indicates that the size effect of GaAs nanowire cannot be completely ignored. The finite size of nanowires further lowers the SO frequency, evidenced by Fig. 5.4.

5.4 Conclusion

In conclusion, we have studied the dependence of the SO modes of GaAS nanowire with base diameter and fill factors. The evolution of the experimental frequencies with these two parameters has been analyzed in comparison with these two theoretical models based on the

continuum dielectric function. The results indicate that the frequency of the SO mode depends on strongly on the fill factor or mean diameter. A similar dependence from GaN nanowire was reported [19]. The dependence of the SO frequency with fill factor can be understood by evaluating the effective dielectric functions. Furthermore, the polar semiconducting nanowire can expect SO mode splitting and shift between LO and TO phonon modes in which these effects will be more pronounced by fill factor. The dipolar interaction of neighboring nanowires is found to be physical mechanism to generate the splitting and downshift of the SO modes. The splitting and the density dependence of nanowires provide useful information to probe the dielectric environment and the orientation of nanowires using Raman Spectroscopy.

Figures

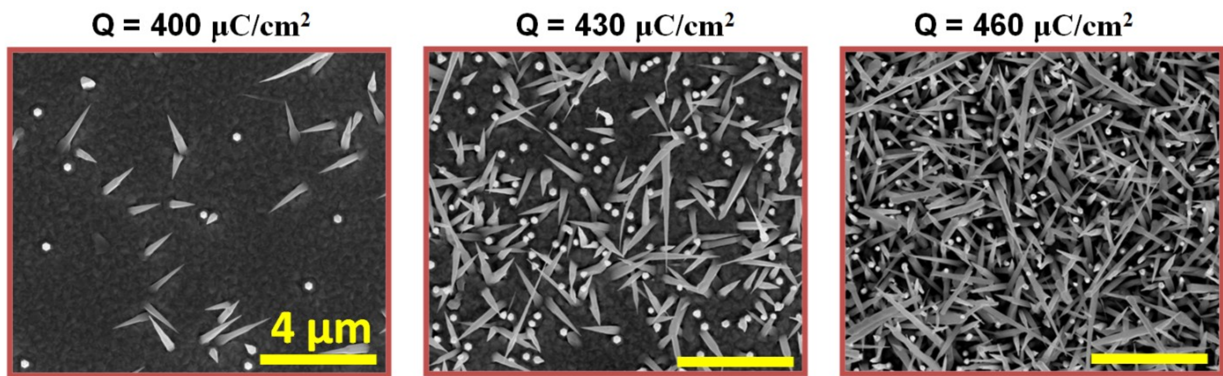

Figure 5.1 SEM micrographs of the GaAs nanowire samples as a function of electron beam dose.

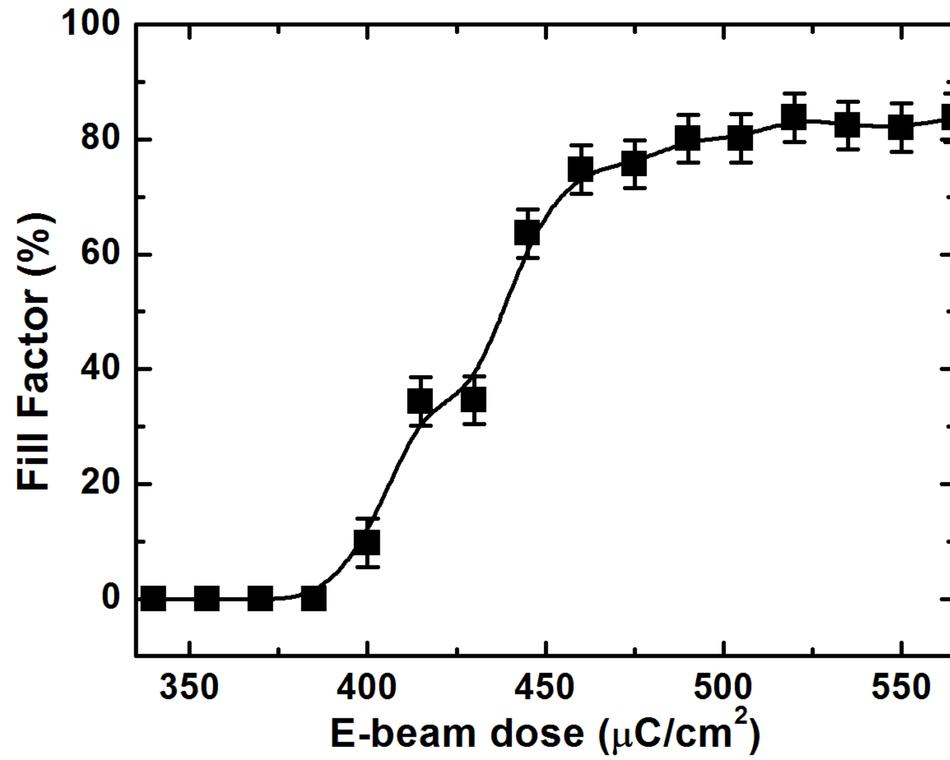

Figure 5.2 Variation of the fill factor of GaAs nanowires as a function of e-beam dose.

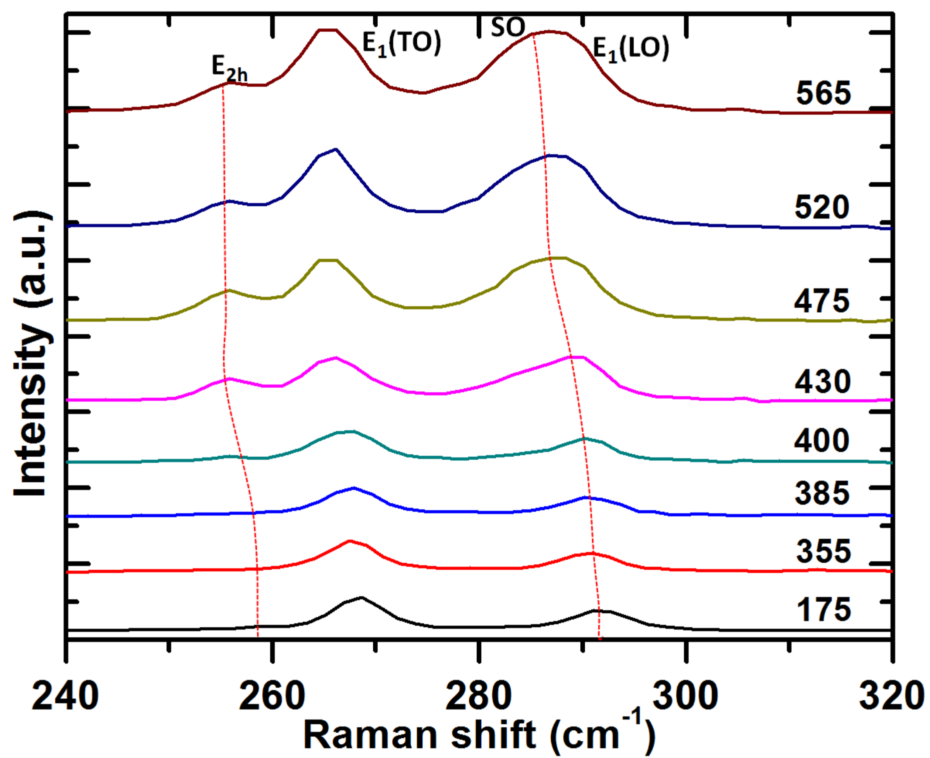

Figure 5.3 Raman spectra for different e-beam doses from 175 μC/cm^2 to 565 μC/cm^2.

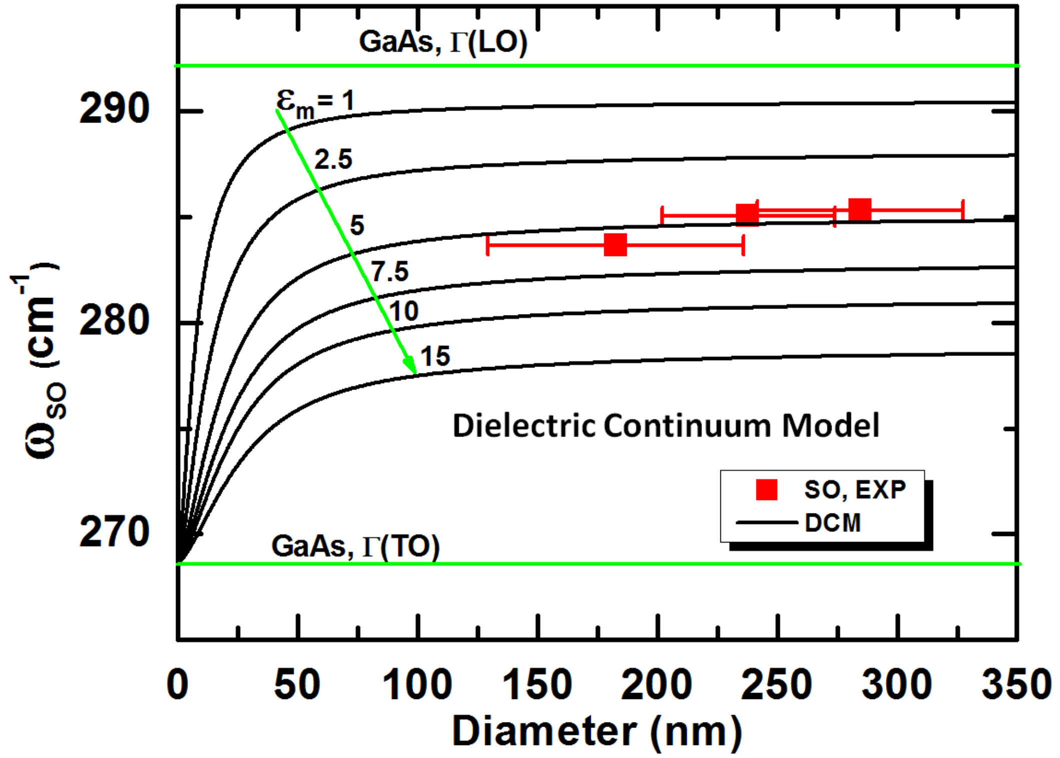

Figure 5.4 Frequency of the SO mode as a function of nanowire diameter for various surrounding media (i.e. $\varepsilon_m^{air} = 1$). The full red squares correspond to the experimental SO mode observation.

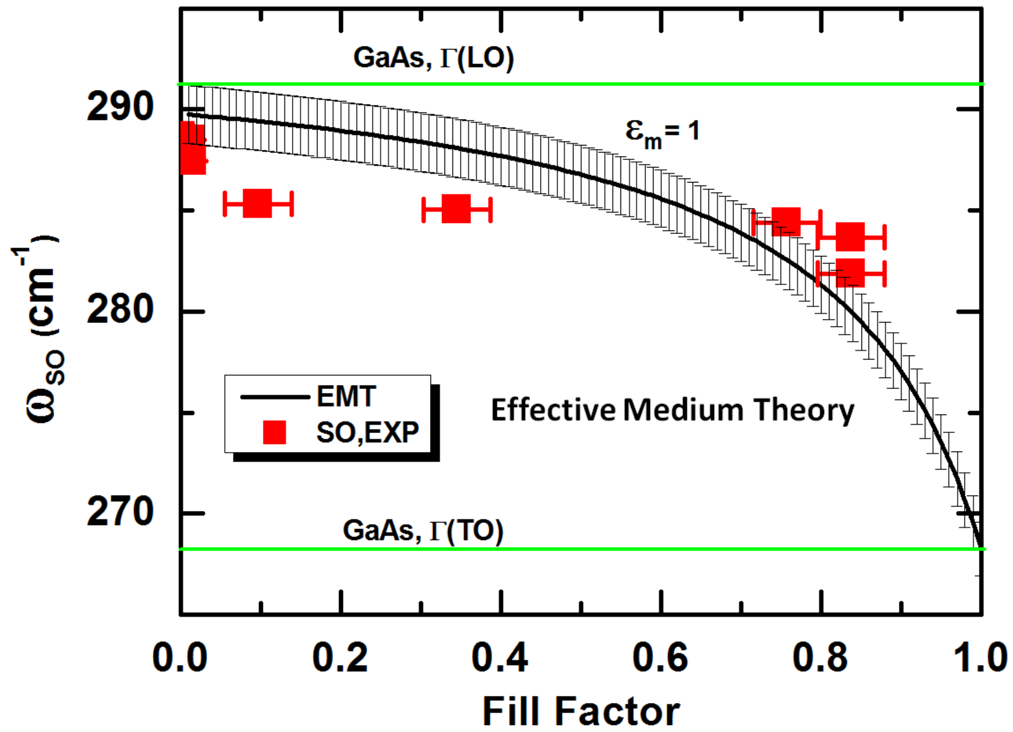

Figure 5.5 Frequency of the different phonon modes obtained within the effective dielectric function approximation with the experiment results. Full red squares correspond to the SO mode.

Supporting Information

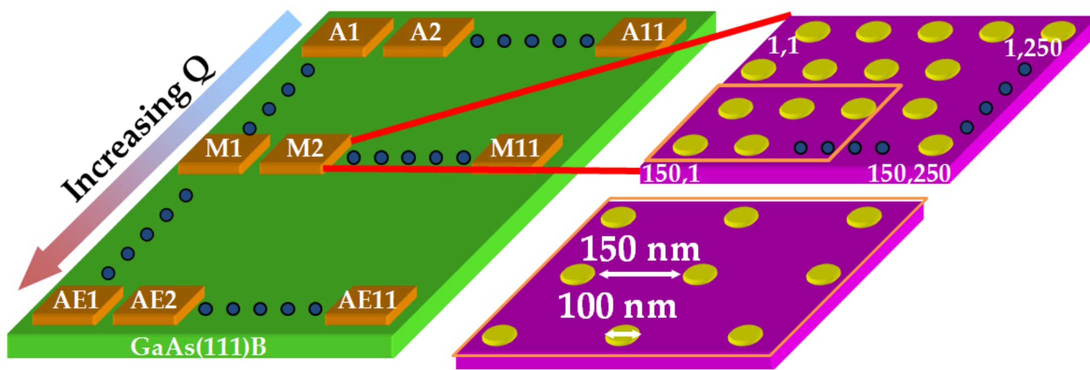

Figure 5.S1 Au catalyst layer patterning condition on GaAs(111)B wafer.

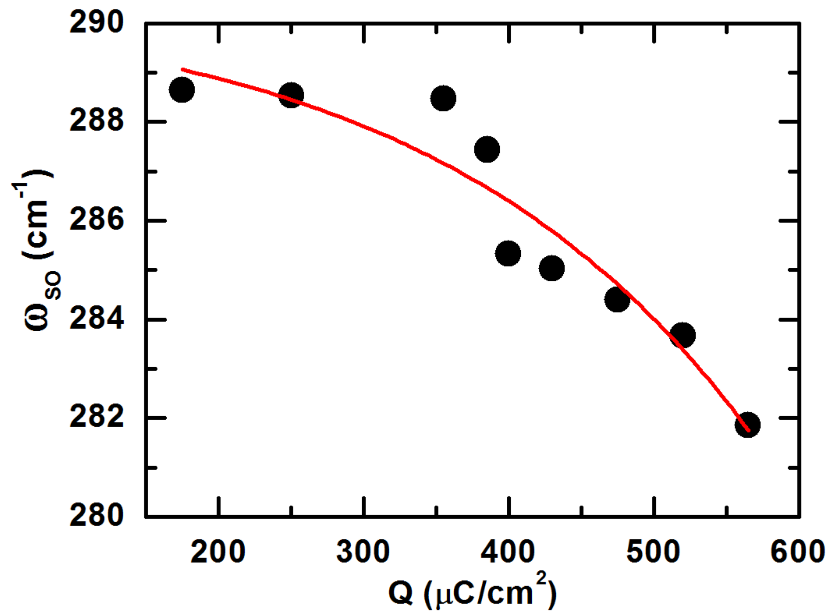

Figure 5.S2 Surface Phonon Frequency as a function of electron beam dose.

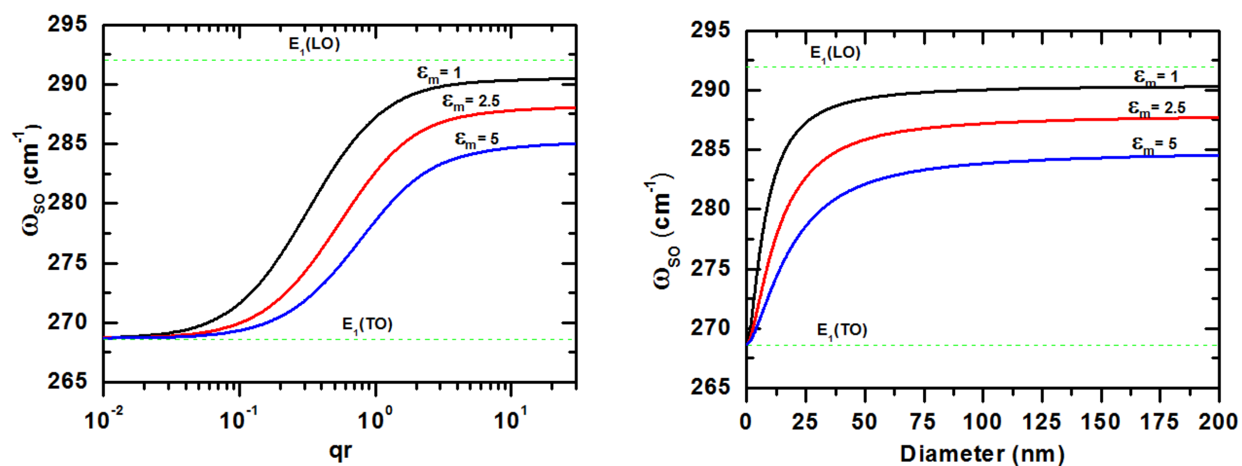

Figure 5.S3 SO phonon calculation of GaAs nanowires using Dielectric Continuum Model

References

[1] M. Law, J. Goldberger, and P. Yang, Annu. Rev. Mater. Res. 34, 83 (2004).

[2] P. Prete, Ed. Nanowires (InTech, Croatia, 2010), Chapter 12-13. ISBN 978-953-7619-79-4.

[3] K. W. Adu, M. D. Williams, M. Reber, R. Jayasingha, H. R. Gutierrez, and G. U. Sumanasekera, Journal of Nanotechnology 2012, Article ID 264198, 18 (2012). doi:10.1155/2012/264198

[4] M. Becker, V. Sivakov, U. Gösele, T. Stelzer, G. Andrä, H. J. Reich, S. Hoffmann, J. Michler, and S. H. Christiansen, Small 4, 398 (2008).

[5] L. Cao, B. Nabet, and J. E. Spanier, Phys. Rev. Lett. 96, 157402 (2006).

[6] M. Möller, M. M. de Lima Jr., A. Cantarero, L. C. O. Dacal, J. R. Madureira, F. Iikawa, T. Chiaramonte, and M. A. Cotta, Phys. Rev. B 84, 085318 (2011).

[7] Q. Xiong, J. Wang, O. Reese, L. C. Lew Yan Voon, and P. C. Eklund, Nano Lett. 4, 1991 (2004).

[8] I. Zardo, S. Conesa-Boj, F. Peiro, J. R. Morante, J. Arbiol, E. Uccelli, G. Abstreiter, and A. Fontcuberta i Morral, Phys. Rev. B 80, 245324 (2009).

[9] R. Gupta, Q. Xiong, G. D. Mahan, and P. C. Eklund, Nano Lett. 3, 1745 (2003).

[10] S. Sahoo, S. Dhara, A. K. Arora, R. Krishnan, P. Chandramohan, and M. P. Srinivasan, Appl. Phys. Lett. 96, 103113 (2010).

[11] G. D. Mahan, R. Gupta, X. Xiong, C. K. Adu, and P. C. Eklund, Phys. Rev. B 68, 073401 (2003).

[12] P. J. Pauzauskie, D. Talaga, K.-Y. Seo, P. Yang, and F. Lagugné-Labarthet, J. Am. Chem. Soc. 127, 17146 (2005).

[13] J. H. Park, S. Prikhodko, M. Pozuelo, V. Gambin, and S. Kodambaka, submitted for review (2012).

[14] F. J. García-Vidal, J. M. Pitarke, and J. B. Pendry, Phys. Rev. Lett. 78, 4289 (1997).

[15] M. Watt, C. M. Sotomayor Torres, H. E. G. Arnot, and S. P. Beaumont, Semicond. Sci. Technol. 5, 295 (1990).

[16] K. W. Adu, Q. Xiong, H. R. Gutierrez, G. Chen, and P. C. Eklund, Appl. Phys. A 85, 287 (2006).

[17] http://www.ioffe.rssi.ru/SVA/NSM/Semicond/GaAs/basic.html

[18] J. J. C. Garnett, Philo. Trans. R. Soc. 203, 385 (1904).

[19] R. Mata, A. Cros, K. Hestroffer, and B. Daudin, Phys. Rev. B 85, 035322 (2012).

[20] R. Loudon, Adv. Phys. 13, 423 (1964).

CHAPTER 6

RAMAN SCATTERING IN SELF-CATALYZED InP NANOSTRUCTURE: MORPHOLOGY AND SUBSTRATE EFFECTS

6.1 Introduction

The compatibility of group III-V nanowires with homo- and hetero- substrates has been gained much attention for monolithic integration of current silicon technologies [1,2]. Fundamental understanding of morphology, crystal structure, and substrate orientation effect of III-V nanowire growth are highly desirable to successfully integrate its superior electronic and optoelectronic properties with Si technology [3,4,5,6,7]. Indium phosphide (InP) is a promising semiconductor material for potential applications in light emitting diodes, laser diodes, single photon and electron sources, photo detectors, heterojunction transistors, sensors, solar cells and battery anodes due to its band gap tunability, high carrier mobility, and large breakdown field [8,9,10]. Such nanowires are prepared by the vapor-liquid-solid process using gold catalyst [11], resulting in the unintentional incorporation into the pure crystalline nanowires [12]. For the combination with Si technology, it is problematic due to Au forming deep trap level in Si [13]. Indium is compatible with silicon integrated catalyst and In droplet can be deposited in situ before nanostructure growth [14]. Self-catalyzed growth of InP nanostructures is desirable to avoid foreign metal seed incorporation.

Micro Raman spectroscopy is a time efficient and noninvasive experimental technique to evaluate the purity of crystals and microstructures from vibration mode analysis [15]. Phonon frequencies and scattering intensities are dependent on the perfection of crystal structure and impurity of foreign agents. In general, the presence of defects in nanostructures is usually

characterized using transmission electron microscopy. TEM measurement can be challenging to examine lager numbers of nanostructures to obtain statistically meaningful data which will provide overall insights of as-grown nanostructure quality. Recently Raman scattering characterization of InP quantum dots [16], nanowire [17], and epilayer [18] structures have been extensively studied to get insight on an individual nanostructure such as phonon confinement [19,20], surface optical phonon modes [21], and aspect ratio effects [22]. However, very little is known concerning substrate and morphology induced optical properties of self-catalyzed InP nanostructures.

In this chapter, we present results from Raman spectroscopic studies of catalyst-free InP nanopillar and nanocone bundles using metal organic chemical vapor epitaxy. We examined morphology, crystal structure induced Raman scattering on the self-catalyzed InP nanostructures grown on InP and Si substrates. The lattice vibration modes of InP nanostructures are investigated using micro Raman spectroscopy. The effect of nanostructure shapes on the mode changes of longitudinal optical (LO), transverse optical (TO), and surface optical (SO) phonons are studied. Size effect induced LO mode variations are observed and discussed.

6. 2 Experimental Details

The experiments were carried out in a Veeco D125 metalorganic vapor-phase epitaxy reactor using trimethylindium (TMIn) and tertiarybutylphosphine (TBP). For the nanostructures grown on InP (111)B substrates [23], the samples were placed in the reactor and annealed at 550 $^{\circ}$C in 1.0 mmol/min of TBP for 5 min. Then the temperature was lowered to between 350 and 400 $^{\circ}$C, and the indium droplets were deposited by feeding 20 - 50 μmol/min of TMIn for 0.2 – 0.5 min. Next, the InP nanostructures were deposited by feeding TBP and TMIn at P/In

mole ratios between 29 and 200. A constant TBP mole fraction of 7.2×10^{-4} was maintained in the hydrogen gas flow at 60 Torr total pressure. Following 5 to 15 min of growth, the samples were cooled down in H_2 over 10 min to 30 $^{\circ}$C.

For InP nanostructure growth on silicon substrate [14], two different types of substrates, Si (111) and Si (100) with 0.5° miscut angles, were used. They both were boron doped with resistivity of 0.002-0.008 and 1932-2110 Ω•cm, respectively. The Si wafers were cleaned in 5% hydrofluoric acid solution for 30 seconds and loaded immediately into the MOVPE reactor. The wafers were annealed at 600°C in 1.0 mmol/min of flowing TBP for 5 min. Then the temperature was lowered to 350°C, and indium droplets were deposited by feeding 5.4 μmol/min of TMIn for 5 sec. The sample was annealed for 30 sec to form uniform distribution of In droplets. Next, the InP nanowires were deposited by feeding TBP and TMIn at a P/In mole ratio between 54 and 200. Following 5 to 15 min of growth, the samples were cooled down in flowing H_2 for 10 min to 30 $^{\circ}$C. A constant TBP mole fraction of 7.2×10^{-4} was used in a hydrogen gas flow at 60 Torr total pressure. After deposition, the nanowires are examined using a FEI NOVA 230 field emission scanning electron microscope.

Two Raman systems (Renishaw 1000 and InVia) are used in this experiment [24]. Raman spectra of the ensembles of InP nanopillars or nanocones on either Si or InP(111)B substrate, as a grown sample, were measured in backscattering geometry with confocal configuration using a Renishaw InVia Raman spectrometer coupled with a laser wavelength of 514.5 nm and a excitation power from 0.1 mW to 25 mW. The laser beam was focused through a microscope to a spot size of approximately 1 μm in diameter. The spectra were characterized with a resolution of 0.5 cm^{-1}. All spectra are collected in ambient conditions, at room temperature, and are calibrated to the reference Si peak arising from the substrate (520.1 cm^{-1}). All Raman spectra are

fitted with symmetric Gussian-Lorentzian function mixture to extract the quantities of the information of interest.

6.3 Results and Discussion

Figure 6.1 shows the SEM images of InP nanostructures grown on InP(111)B substrate. It is observed that vertical and uniform InP nanostructure with hexagonal cross sections are obtained from both nanopillars and nanocones. All nanostructures are grown along the <111> direction, which is perpendicular to InP(111)B substrate surface. No large base islands are observed at the base area surrounding nanostructure root, which are usually observable from the catalyst-assisted or high temperature growth (See Fig. 6.S1). From high magnification SEM images over 30 individual InP nanostructures for each materials system, we measured the average heights, base diameters, and aspect ratio of heights over base diameters. The statistical size information of InP nanostructures for five samples are summarized in Table I.

Figure 6.1a and 1c show a SEM image of nanopillars acquired at 400 $^{\circ}$C and a P/In mole ratio of 89. The indium droplets were initially formed by feeding 50 μmol/min of TMIn for 12 s. A base diameter of nanopillars is observed with average size of 53 ± 4 nm, as shown in Fig. 6.1a. The nanopillars show nearly identical base diameter with narrow distribution and good for Raman scatting experiment. Upon introducing the TMIn and TBP, InP nanopillars with hexagonal bases grow up as shown in Fig. 6.1a. With continued deposition, the In droplet becomes indiscernible and facets form along the {110} and {112} sidewalls of the pillars as shown in Fig. 6.1c. The pillar height increases during the first 2 min of growth, and thereafter remains constant. The average height of nanopillars is measured for 146 ± 9 nm. On the other hand, the pillar base width continuously increases throughout the process due to sidewall

deposition of InP [23]. The above results show that vertical growth of the nanopillars occurs with consumption of the indium droplets and ceases after they are gone. It follows then that broadening of the pillar bases occurs via lateral deposition along the sidewalls from the vapor, i.e., by vapor-phase epitaxy of indium phosphide on the exposed {110} and {112} planes [23]. Detailed characterization of crystal structures are discussed for InP nanocones and nanopillars [25].

Figure 6.1b and 1d show SEM images of InP nanocones acquired at 385 $^{\circ}$C and a P/In mole ratio of 30. Prior to introducing the TBP, indium droplets were deposited by feeding 20 μmol/min of TMIn for 30 s. Upon feeding 1.0 mmol/min TBP along with the TMIn, the nanostructures begin growing with the indium catalyst at the top. For VLS growth, the liquid indium catalyzes the decomposition reaction and results in dissolution of the indium and phosphorus into the droplet. Incorporation of the In and P atoms from the droplet at the liquid-solid interface results in the formation of the indium phosphide nanowire. The average base diameter of nanocones is 49 ± 10 nm. The wire width and catalyst remain constant throughout the process, while the average wire length increases linearly at a rate of ~ 110 nm/min. The as-grown nanocones are homogeneous both in width and height (See the inset of Fig. 6.1b). The nanocones used in the Raman scattering measurement exhibits the average height of 586 ± 35 nm.

Figure 6.2 shows Raman spectra of InP nanostructures grown on InP(111)B. InP(111)B single crystal wafer was included as a reference and similar spectrum can be found from Chen *et al.* report [26]. All spectra from two samples clearly show two phonon modes which can be assigned with the transverse optical mode (TO) at 304 cm^{-1} and longitudinal-optical mode (LO) at 344 cm^{-1} at the Brillouin zone center. The two phonon modes are expected to be characterized

in a backscattering geometry [27]. Due to polar nature of Group III-V nanostructures, for Raman scattering by (111) crystal plane, both TO and the LO phonons are allowed in the selection rule but only the LO phonon is allowed for scattering by (100) crystal plane, and only TO phonon is allowed for (110) crystal plane [28]. However, LO and TO phonons appeared in the back scattered geometry, due to the crystal symmetry break in one-dimensional nanostructures [29]. Here the selection rules for backscattering are prominent particularly TO phonons due to surface-to-volume ratio of (110) face increase in InP nanocones over nanopillars. In spite of identification of both TO and LO modes, the intensity ratio of TO over LO (I_{TO}/I_{LO}) much different from InP single crystal wafer, indicating that the intensity of LO mode in InP nanocones is much higher than that in nanopillars. It is also attributed to the large surface-to-volume ratio of InP nanocones over InP nanopillars. Additionally, surface optical (SO) phonon modes are found at 273 cm^{-1}, implying a crystal symmetry breaking in InP(110) plane [30]. All assigned peaks from Raman spectra are summarized in Table 6.II.

We also grow InP nanostructures (nanocone or nanopillars) on silicon substrates (111 or 100). Upon increasing growth temperature above 400 ^{o}C, nanopillar structures become dominant rather than nanocones. Increasing the growth temperature at a fixed P/In mole ratio causes the formation of conical and pillar-shaped InP nanostructures rather than wires. Figure 6.3a & 3d show a top-view and tilted view of InP nanopillars with hexagonal bases that are acquired at 400 ^{o}C and V/III ratio of 200. The pillar bases are 91 ± 13 nm. The height variation of pillars is observed with the average of 122 ± 17 nm. The InP thin film with rough surface is observed, indicating that heterogeneous nucleation of In on the silicon matrix prefers lateral growth than vertical growth [14].

The SEM images of InP nanocones deposited on Si(111) are shown in Figs. 6.3b, 3e. The process conditions were 370 ^{o}C and V/III ratio of 200. The growth time was 6 min. The length of the nanocones is 751 ± 33 nm. The wire diameters are 74 ± 4 nm. Growth temperature is the most important parameter for the growth of vertically aligned InP nanocones on Si substrate. The growth orientation and crystal studies of self-catalyzed InP nanostructures on silicon substrate can be found in our previous publication [14]. All InP nanocones are vertically aligned along <111> direction, respected to Si(111) substrate.

Figure 6.4 shows Raman scattering measurement from InP nanostructures (nanocone, nanopillar on Si(111) or Si(100) substrate. All three samples clearly show Si Raman spectra at 520.1 cm^{-1}, indicating that nanostructures on Si substrates have good crystallinity. The Raman spectra of TO and LO modes obtained from InP nanostructures on Si(111) substrates are very similar to that from the results from InP(111)B substrates but show relevant differences with respect to the spectrum from Si(100) substrate. Both TO and LO singles in the InP nanocones are downshifted and broadened with respect to the InP bulk, not shown in the graph. Two additional phonon modes at acoustic branch and at optical branch are found at 254 cm^{-1} and 274 cm^{-1}, respectively. It is also found that the intensity of LO is more sensitively changed than that of TO, respect to their nanostructures (bulk, nanopillars, nanocones).

Figure 6.5 shows deconvoluted Raman spectra of TO and LO phonon modes from InP nanostructures on InP(111)B. Campbell *et al.* material size and shape can affect the Raman scattering by LO phonons [31]. Nanosized materials (i.e. sub nanometers) leads to a downshift and broadening of the LO Raman line due to the relaxation at Γ (q=0) point governed by the selection rule [32]. In this work, however, the base diameters of nanostructures on InP(111)B and Si(111) substrates are at least 10 times larger than Campbell's material system [31]. The

downshift and broadening cannot be explained by the phonon confinement effect (few nanometer scales) [33]. Instead, it can be explained by the surface-to-volume ratio of {110} and {111} planes with the increasing the defect density in the nanostructures [32]. High resolution TEM images with electron diffraction pattern of InP nanocone on InP(111)B substrate indicate coexistence of both ZB and WZ stacking faults within the nanocone (See Fig. 6.S2 and the supplemental in [25]). On the other hand, WZ crystal structures are dominant in the InP nanopillars, confirmed by TEM and electron back-scattered diffraction [25]. The presence of E_2^{high} around 254 cm^{-1} is indicative of the existence of WZ phase for both nanocones and nanopillars as shown in Fig. 6.2 and 6.4. Due to the increase of surface-to-volume ratio of InP nanocones over nanopillars, the {110} crystal planes and defect density in InP nanocones are larger than those in nanocones. It is believed that enhanced LO intensity in InP nanocones is attributed to the differences in {110} area and defect density. Therefore, the intensity ratio (I_{TO}/I_{LO}) for InP nanocone shows lower value than that of InP nanocones and InP(111)B bulk substrate.

Figure 6.6 shows deconvoluted Raman spectra of TO and LO phonon modes from InP nanostructures on Si(111). Both InP nanopillar and nanocones show substantial broadening and slight downshift compared to InP(111) substrate. Similar to InP nanocones on InP(111)B, TO phonon appears much more intense than LO phonon. The intensity ratio (I_{TO}/I_{LO}) strongly depends on not only on the crystal orientation but also surface electric field [32,34]. It is found that Raman scattering of InP nanocone grown on Si(100) is much different from InP nanostructures on Si(111) substrate. The spectrum of InP nancone on Si(100) shows substantial broadening and intensity ratio difference (See Fig. 6.S3). The larger surface-to-volume ratio with scattering volume and surface electric fields are contributed to increasing TO and LO line

intensity, resulting in decrease of the intensity ratio. Additionally, SO phonon mode was only observed at 274 cm^{-1} from InP nancones on Si(111) (see Figs. 6.4 & 6.6c), indicating that large surface-to-volume ratio of nanostructures are characterized and the SO modes are dependent on the nanostructure base diameters [35]. It is known that SO phonon is also sensitive to the crystal structure and surface roughness [36].

We further examined morphology dependent phonon vibration using different micro Raman system. It is noted that all results are consistent with previous measurements. Raman spectra were performed in a conventional backscattering geometry with Renishaw 1000 micro-Raman spectrometer using an argon laser (514 nm) as an excitation source. The laser output power was changed from 0.1mW to 10 mW with a spot size of 1 μm and a spatial resolution of 0.5 cm^{-1}. Figure 6.7 shows laser power dependence of InP nanocones grown on Si(111) substrate. Two TO and LO phonon peaks are clearly resolved. Asymmetric broadening and downshift for TO and LO phonons were also found in this measurement. In particular, SO phonon mode was identified at 274 cm^{-1}, which is consistent with theoretical prediction [30].

6.4 Conclusion

In conclusion, highly crystalline vertically aligned InP nanostructures with hexagonal cross-sections have been synthesized on various substrates (i.e. InP(111)B, Si(111), Si(100)) by self-catalyzed MOCVD growth. Systematic studies of micro Raman scattering from these nanostructures at room temperature in air have resolved strong first order LO, TO, and SO modes. The presence of E_2^{high} mode confirms that our nanostructures have a mixture of WZ and ZB phases or pure WZ phase. The SO mode is only identified from high surface-volume ratio structure (i.e. nanocones). The LO modes excited by surface electrical fields are suppressed with

the decreases of surface-to-volume ratio and defect density in InP nanostructures. These results indicated that Raman scatterings on well aligned nanostructures thinner than 100 nm in base diameter are governed by surface-to-volume ratio and defect density, which modify the selection rules for the bulk crystal. Furthermore, the Raman scattering will provide further statistical insight on the quality of as-grown nanostructures (i.e. growth orientation, crystal structures, and the presence of structural defects) without destroying samples.

Substrate	**InP (111)B**		**Si (111)**		**Si (100)**
Morphology	InP NPs	InP NCs	InP NPs	InP NCs	InP NCs
Length L	152 ± 10 nm	586 ± 35 nm	122 ± 17	751 ± 33	469 ± 64
Diameter D	53 ± 4 nm	49 ± 10 nm	91 ± 13	74 ± 4	18 ± 3
Aspect Ratio L/D	2.9	11.9	1.3	10.2	26.1

Table 6.I Summary of average InP nanostructure dimensions. Note: Length of InP NCs grown on Si (100) sample is only measured for 15 individual wires due to geometrical limitation with random orientations.

Material	**Branch**	**Mode**	**Position**
InP	Γ	E_1(TO)	305.0
InP	X, L, Γ	A_1(LO)	336, 341, 345
InP	L	E_2^{high}	254
InP	Γ	SO	274
Si	Γ	-	520.1

Table 6.II Raman vibration modes of InP nanostructures and Si bulk substrate

Figures

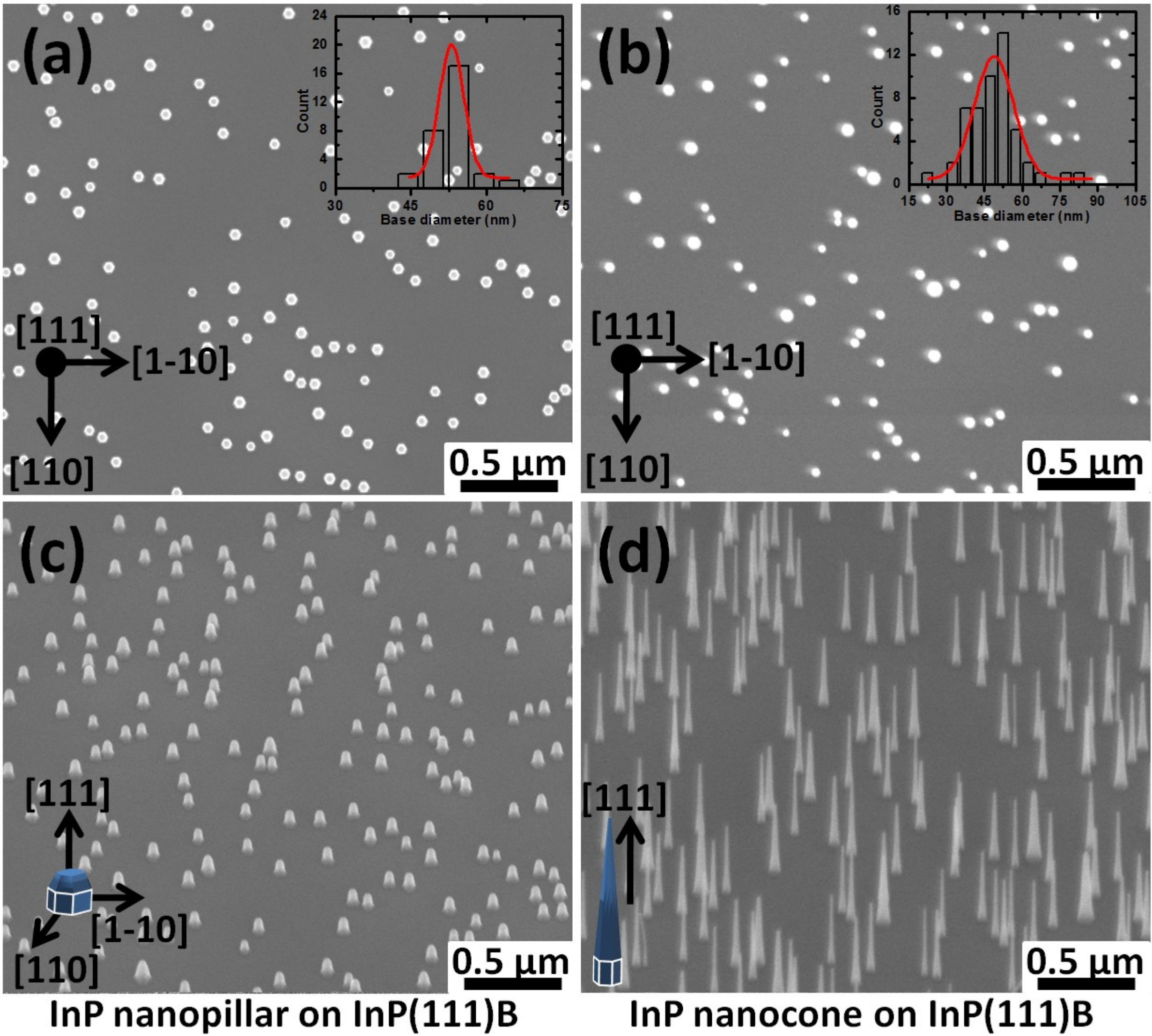

Figure 6.1 Scanning Electron Micrographs of self-catalyzed InP nanostructures grown on InP(111)B substrate. Top view: (a) InP nanopillar on InP(111)B, (b) InP nanocone on InP(111)B. Tilted view with 40 degree: (c) InP nanopillar on InP(111)B, (d) InP nanocone on InP(111)B.

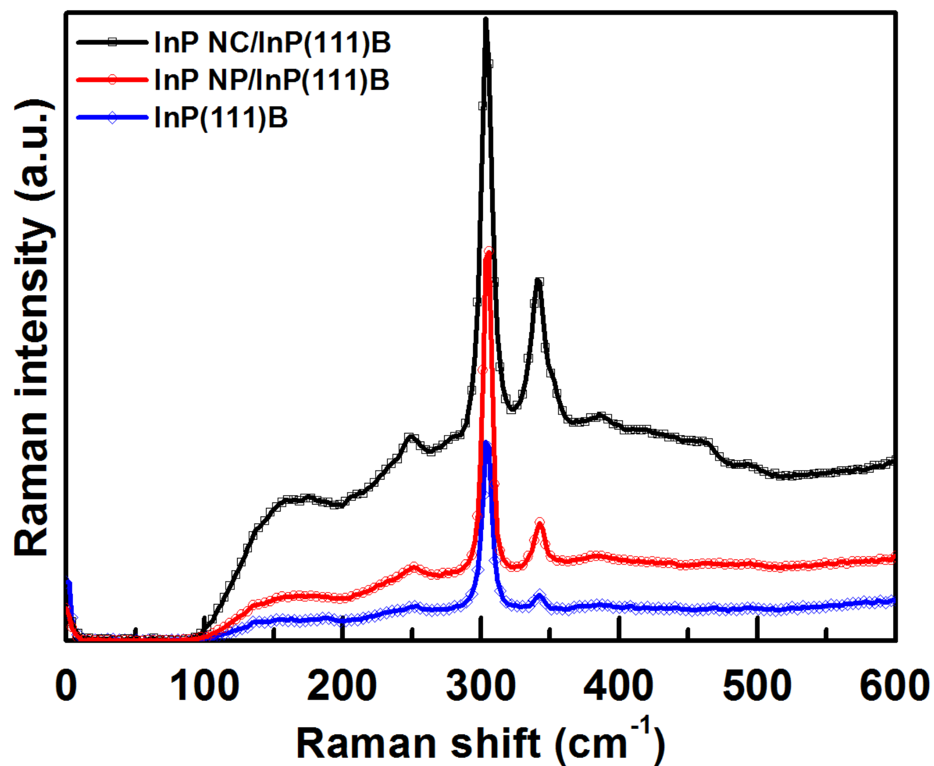

Figure 6.2 Raman spectra of InP nanostructures grown on InP(111)B substrate. The laser with wavelength of 513.6 nm excitation was used as the excitation source.

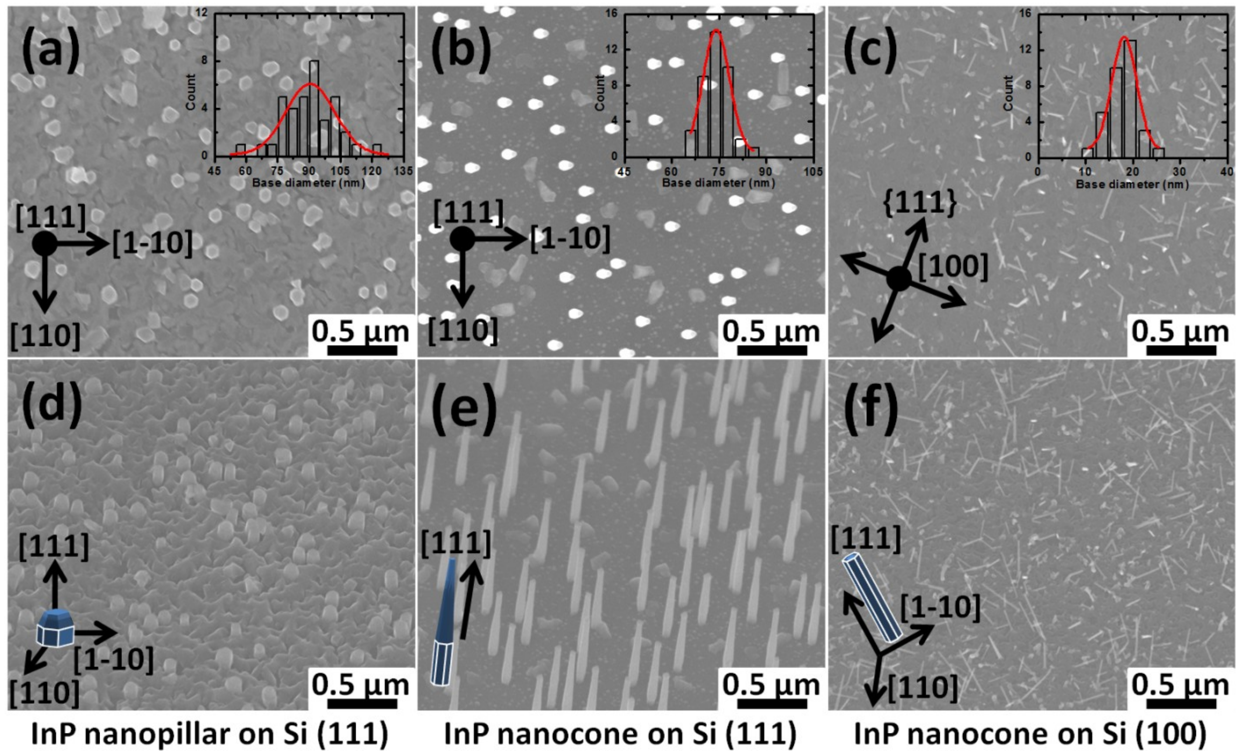

Figure 6.3 Scanning Electron Micrographs of self-catalyzed InP nanostructures grown on silicon single crystal substrate. Top view: (a) InP nanopillar on Si(111), (b) InP nanocone on Si(111), (c) InP nanocone on Si(100). Tilted view with 40 degree: (d) InP nanopillar on Si(111), (e) InP nanocone on Si(111), (f) InP nanocone on Si(100).

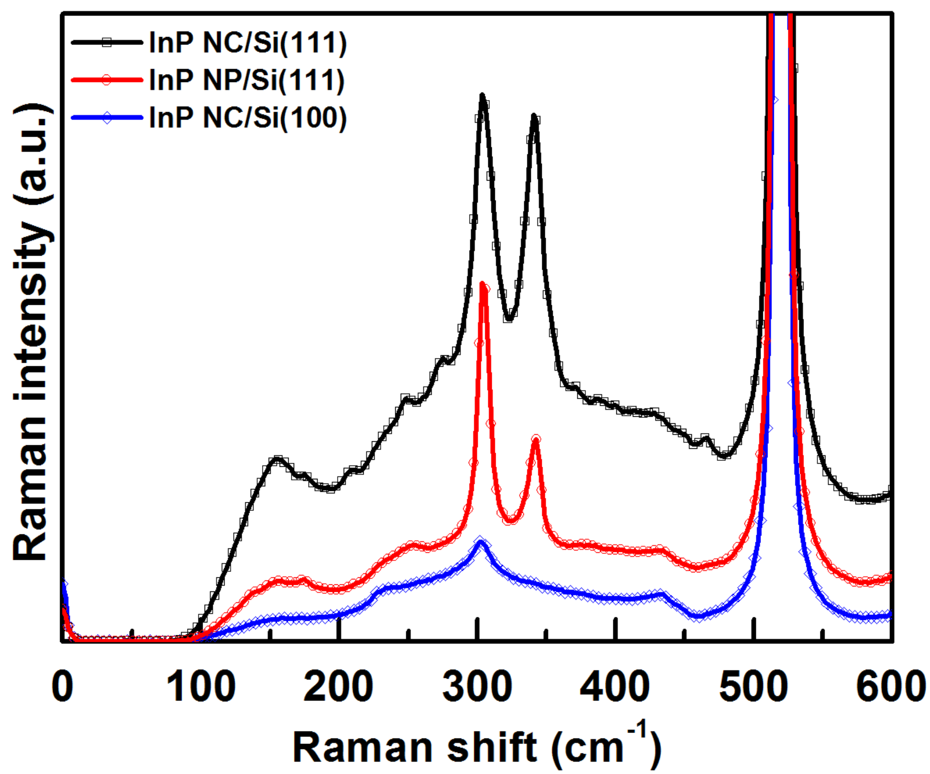

Figure 6.4 Raman spectra of self-catalyzed InP nanostructures grown on Si(111) and Si(100) substrates.

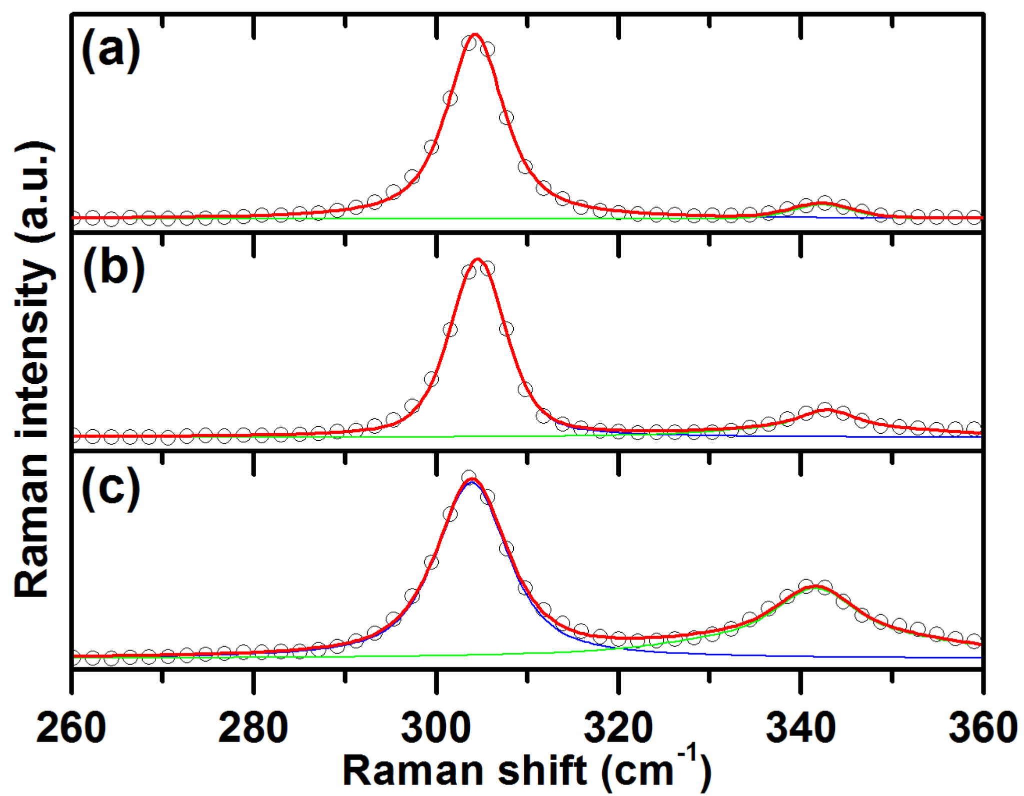

Figure 6.5 Raman spectra of (a) InP(111)B single crystal substrate, (b) self-catalyzed InP nanopillars grown on InP(111)B, (c) self-catalyzed InP nanocones grown on InP(111)B.

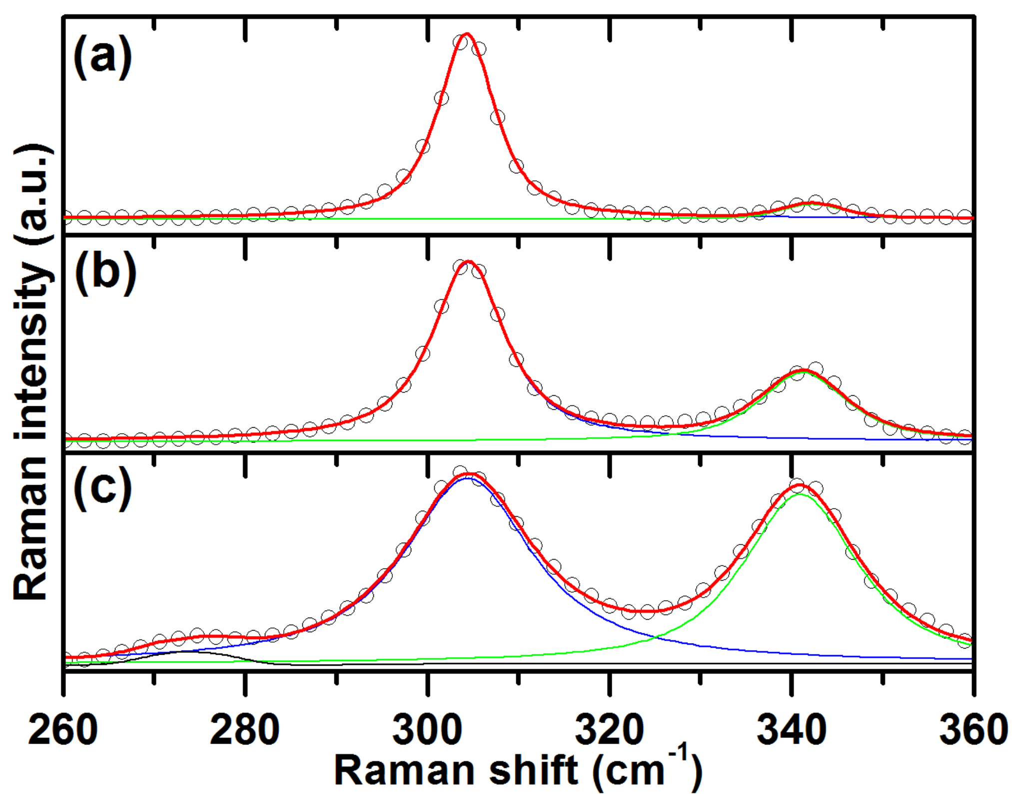

Figure 6.6 Raman spectra of (a) InP(111)B single crystal substrate, (b) self-catalyzed InP nanopillars grown on Si(111), (c) self-catalyzed InP nanocones grown on Si(111).

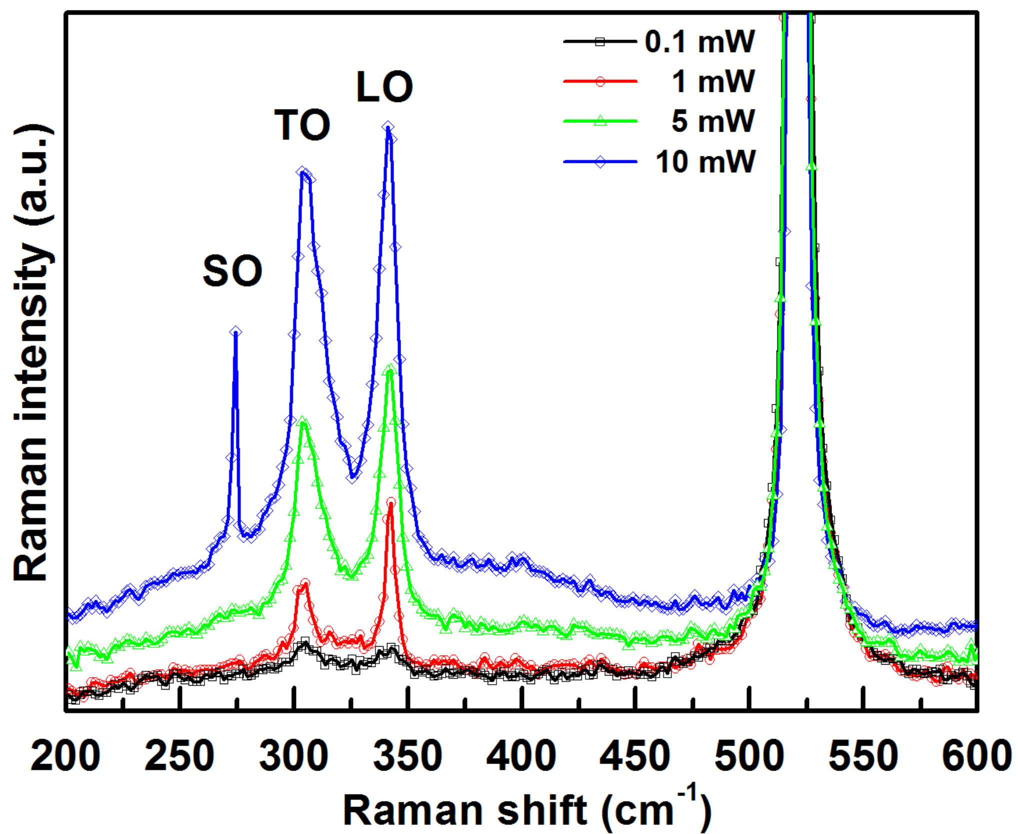

Figure 6.7 Raman scattering spectra of InP nanocones on Si(111) substrate as a function of laser out-put power.

Supporting Information

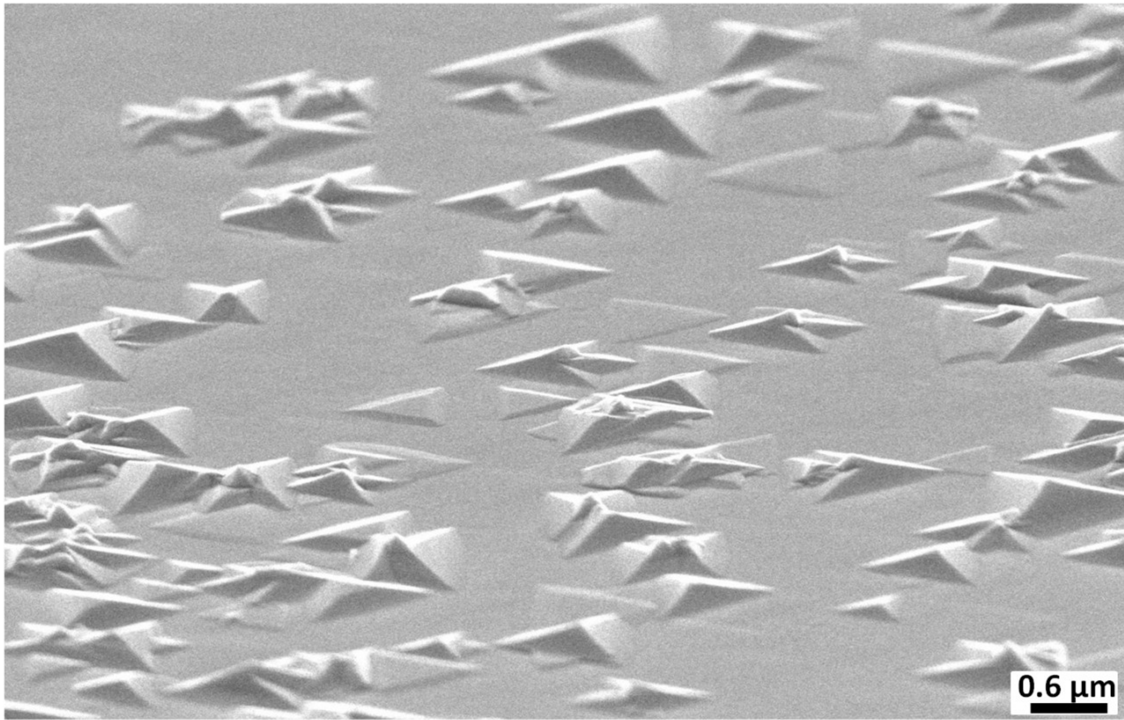

Figure 6.S1 High temperature deposition of InP nanostructure, exhibiting preferred lateral growth to vertical growth.

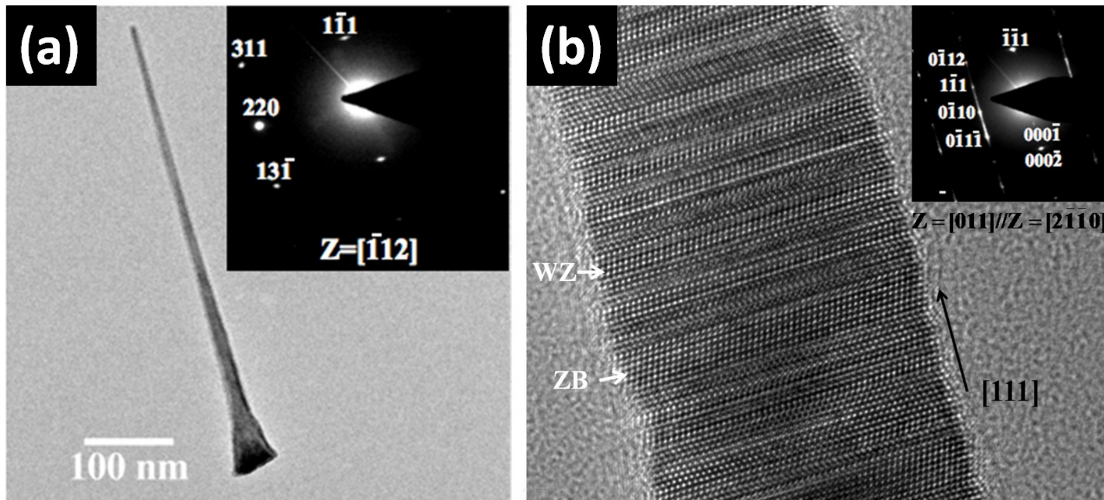

Figure 6.S2 (a) Bright field image of homogeneous InP nanocones grown on InP(111)B with electron diffraction pattern of the wire viewed along the $[\bar{1}12]$ axis. (b) High resolution transmission electron micrograph of InP nanocones with electron diffraction pattern viewed along $[011]_{WZ}$ and $[2\bar{1}\bar{1}0]_{ZB}$ axis.

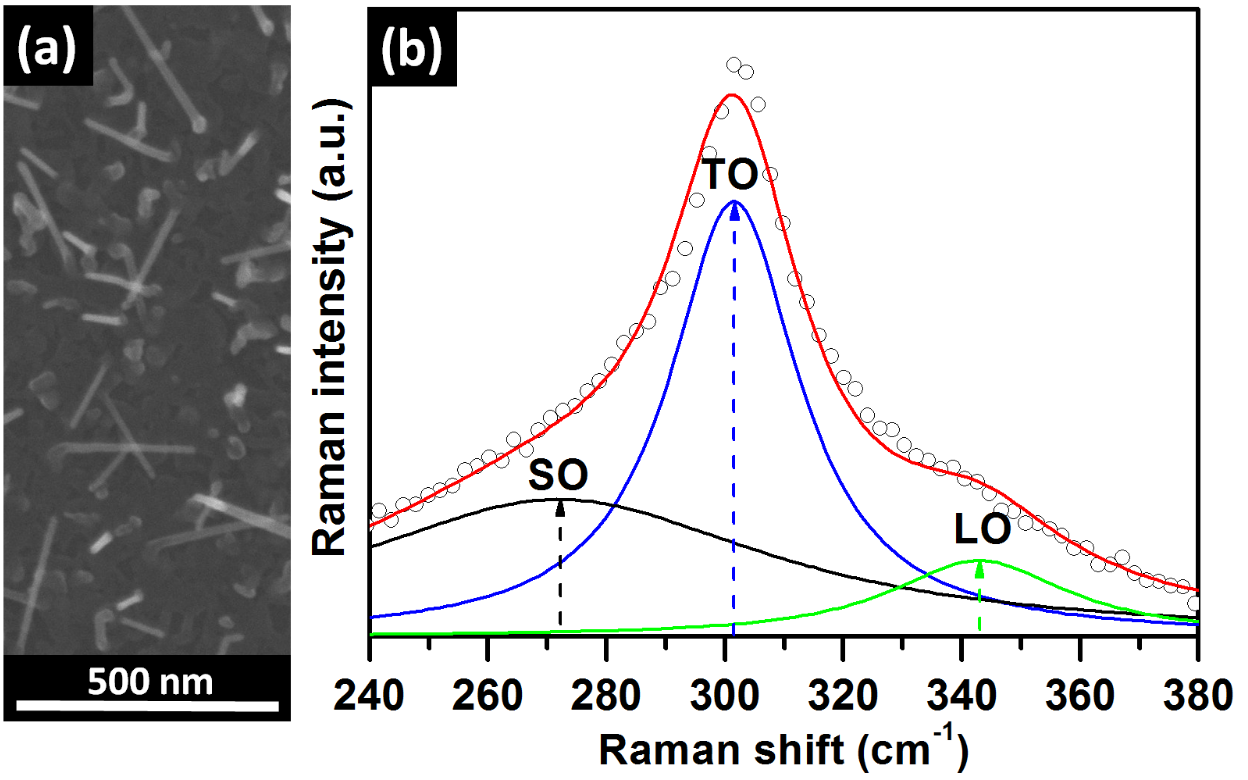

Figure 6.S3 (a) SEM image of randomly oriented InP nanowires grown on Si(100) substrate, (b) the corresponding a Raman spectrum.

References

[1] R.S. Wagner, Whisker Technology, Wiley, New York (1970).

[2] E.W. Wong, P.E. Sheehan, and C.M. Lieber, Science 277, 1971 (1997).

[3] M.P. Persson, and H.Q. Xu, Appl. Phys. Lett. 81, 1309 (2002).

[4] J. Bao, D.C. Bell, F. Capasso, J.B. Wagner, T. Martensson, J. Tragardh, and L. Samuelson, Nano Lett. 8, 3, 836 (2008).

[5] L.C. Chuang, M. Moewe, S. Crankshaw, and C. Chang-Hasnain, Appl. Phys. Lett. 92, 013121 (2008).

[6] A. Fuhrer, L. E. Fr1oberg, J. N. Pedersen, M. W. Larsson, A. Wacker, M.-E. Pistol, and L. Samuelson, Nano Lett. 7, 243 (2007).

[7] S. A. Dayeh, Semicond. Sci. Technol. 25, 024004 (2010).

[8] N. Sköld, L. S. Karlsson, M. W. Larsson, M.-E. Pistol, W. Seifert, J. Trägårdh, and L. Samuelson, Nano Lett. 5, 1943 (2005).

[9] M. Liu, X. Li, H. Imrane, Y. Chen, T. Goodrich, Z. Cai, K. S. Ziemer, and J. Y. Huang, Appl. Phys. Lett. 90, 152501 (2007).

[10] P. Mohan, J. Motohisa, and T. Fukui, Appl. Phys. Lett. 88, 133105 (2006).

[11] R.S. Wagner and W.C. Ellis, Applied Physics Letters 4, 89-90 (1964).

[12] C.J. Novotny and P.K.L. Yu, Applied Physics Letters 87, 203111 (2005).

[13] B. Mandl, J. Stangl, E. Hilner, A.A. Zakharov, K. Hillerich, A.W. Dey, L. Samuelson, G. Bauer, K. Deppert, and A. Mikkelsen, Nano Letters 10, 4443 (2010).

[14] L. Gao, R.L. Woo, B. Liang, M. Pozuelo, S. Prikhodko, M. Jackson, N. Goel, M.K. Hudait, D. L. Huffaker, M.S. Goorsky, S. Kodambaka, and R.F. Hicks, Nano Lett. 9, 2223 (2009).

[15] D. Spirkoska, G. Abstreiter, and A. F. i Morral, Nanotechnology 19, 435704 (2008).

[16] M. J. Seong, O.I. Mićić, A. J. Nozik, A. Mascarenhas, and H. M. Cheong, Appl. Phys. Lett. 82, 185 (2003).

[17] J. Chen, G. Conache, M.-E. Pistol, S. M. Gray, M. T. Borgstrom, H. Xu, H. Q. Xu, L. Samuleson, and U. Hakanson, Nano Lett. 10, 1280 (2010).

[18] A. Mooradia and G. B. Wright, Solid State Comm. 4, 431 (1966).

[19] A. K. Arora, M. Rajalakshmi, T. R. Ravindran, and V. Sivasubramanian, J. Raman Spectroscopy 38, 604 (2007).

[20] M. I. Vasilevskiy, A. G. Rolo, N. P. Gaponik, D. V. Talapin, A. L. Rogach, and M. J. M. Gomes, Physica B 316/317, 452 (2002).

[21] R. Gupta, Q. Xiong, G. D. Mahan, and P. C. Eklund, Nano Lett. 3, 1745 (2003).

[22] G. D. Mahan, R. Gupta, Q. Xiong, C. K. Adu, and P. C. Eklund, Phys. Rev. B 68, 073402 (2003).

[23] R L. Woo, N. Goel, M.K. Hudait, K.L. Wang, S. Kodambaka, and R.F. Hicks, Nano Lett. 9, 2207 (2009).

[24] C.-H. Chung, B. Lei, B. Bob, S.-H. Li, W. W. Hou, H.-S. Duan, and Y. Yang. Chem. Mater. 23, 4941 (2011).

[25] M. Pozuelo, S. V. Prikhodko, R. Grantab, H. Zhou, L. Gao, S. D. Sitzman, V. Gambin, V. B. Shenoy, R. F. Hicks, and S. Kodambaka, J. Cryst. Growth 312, 2305 (2010).

[26] J. Chen, G. Conache, M.-E. Pistol, S. M. Gray, M. T. Borgström, H. Xu, H. Q. Xu, L. Samuelson, and U. Håkanson, Nano Lett. 10, 1280 (2010).

[27] M. Chashnikova, A. Mogilatenko, O. Fedosenko, V. Brykas, A. Petrov, S. Machulik, M.P. Semtsiv, W. Neumann, W.T. Masselink, J. Cryst. Growth 323, 319 (2011).

[28] I. Zardo, S. Conesa-Boj, F. Peiro, J. R. Morante, J. Arbiol, E. Uccelli, G. Abstreiter, and A. Fontcuberta i Morral, Phys. Rev. B 80, 245324 (2009).

[29] J. K. Panda, A. Roy, A. Singha, M. Gemmi, D. Ercolani, V. Pellegrini, and L. Sorba, arXiv:1112.5726v1 (2011).

[30] K. Hinrichs, A. Schierhorn, P. Haier, N. Esser, W. Richter, and J. Sahm, Phys. Rev. Lett. 79, 1094 (1997)

[31] I. H. Campbell and P. M. Fauchet, Solid State Commun. 58, 739 (1986).

[32] N. Begum, M. Piccin, F. Jabeen, G. Bais, S. Rubini, F. Martelli, and A. S. Bhatti, J. Appl. Phys. 104, 104311 (2008).

[33] K. W. Adu, H. R. Gutiérrez, U. J. Kim, G. U. Sumanasekera, and P. C. Eklund, Nano Lett. 5, 409 (2005).

[34] H. Brugger, F. Schäffler, and G. Abstreiter, Phys. Rev. Lett. 52, 141 (1984).

[35] R. Ruppin and R. Englman, Rev. Prog. Phys. 33, 149 (1970).

[36] N. Begum, A. S. Bhatti, F. Jabeen, S. Rubini, and F. Martelli, J. Appl. Phys 106, 114317 (2009).

CHAPTER 7

MULTI PHONON RAMAN SCATTERING IN SELF CATALZYED InP/InAs/InP NANOPILLARS AND NANOCONES

7.1 Introduction

Heterostructure compound semiconductors have been reported for different materials combinations both in coreshell structure [1,2,3] or superlattice nanowires [4,5,6]. InP/InAs heterostructure nanowire [7,8] is a promising semiconductor material for potential applications in light emitting diodes, laser diodes, single photon and electron sources, photo detectors, heterojunction transistors, sensors, solar cells and battery anodes due to its band gap tunability, high carrier mobility, and large breakdown field [9,10,11]. The crystalline and electronic properties of nanowires are critically important for the performance of such devices [12]. Thus, Raman spectroscopy was fully employed to get an insight on semiconductor nanowires properties such as phonon confinement, surface optical phonon modes, and aspect ratio effects inherited from morphology dependent Raman scattering effects. Recently InP quantum dots [13], nanowire [14], and epilayer [15] structures have been extensively studied in previous decades by means of Raman spectroscopy. However, very little is known concerning InP based core-shell nanowires.

In this chapter, we present results from Raman spectroscopic studies of self catalyzed InP/InAs/InP core-shell-shell nanopillar and nanocone bundles with average diameters of 150 nm and 50 nm, respectively, which exhibited a strong dependency on the scattering intensity of excitation light and on scattering geometry.

7.2 Experimental Details

The nanostructures were grown catalyst-free or self-catalyzed on InP(111)B substrate by a Veeco D125 MOVPE reactor using trimethylindium (TMIn), tertiarybutylphosphine (TBP), and tertiarybutylarsine (TBA) as precursors. Depending on nanopillar or nanocone, the substrate temperature was ramped to between 350 ^{o}C and 400 ^{o}C. Indium droplets were deposited by feeding 5.06 × 10^{-5} mol/min of TMIn for 12s. Then TMIn and TBP were introduced into the reactor at flow rates of 3.74 × 10^{-6} and 3.37 × 10^{-4} mol/min (V/III ratio = 90), respectively, to grow the InP nanostructure. After a 540 sec deposition, the reactor was purged with H_2 for 10 s and then with TBA for 180 sec while the temperature was ramped up to 420 ^{o}C. Following the temperature ramp, the InAs shell was deposited onto the InP nanostructure by flowing TBA at 9.82 × 10^{-3} mol/min with a TMIn flow of 8.18 × 10^{-5} mol/min (V/III ratio = 120). The InAs growth time was 10 s. The reactor was purged with H_2 for 10 s and with TBP for 60 sec, and an InP cap layer was deposited by feeding 3.73 × 10^{-6} mol/min of TMIn and 3.37 × 10^{-3} mol/min of TBP (V/III ratio = 90) for 60 sec. Finally, the sample was cooled down and removed from the reactor for characterization. The total pressure in the reactor was maintained at 60 Torr. A reference sample of pure InP nanostructures was prepared by the same procedure given above, except that the InAs shell deposition step was omitted.

The samples analyzed in this experiment were comprised of vertically arrayed nanowires, epitaxially grown on (111)B oriented InP substrate. Raman spectra of the as grown samples, ensembles of InP-InAs-InP nanopillars or nanocones, were measured in backscattering geometry with confocal configuration using a Renishaw InVia Raman spectrometer coupled with a laser wavelength of 514.5 nm and a variable excitation power from 5 mW to 25 mW. The laser beam

was focused through a microscope to a spot size of approximately 1μm in diameter. The spectra were characterized with a resolution of 0.5 cm^{-1}. All spectra are collected in ambient conditions, at room temperature, and are calibrated to the reference Si peak arising from the substrate (520.1 cm^{-1}). All Raman spectra are fitted with symmetric Gussian-Lorentzian function mixture to extract the quantities of the information of interest.

7.3 Results and Discussion

Figure 7.1 shows InP nanopillars, InP/InAs/InP nanopillars, and InP/InAs/InP nanocones grown on different InP(111)B substrates. The growth InP(As) core-shell nanostructures are observed in the temperature range of 320 ^{o}C to 400 ^{o}C. All nanostructures grow epitaxially and straight in the <111>B direction with slight tapering. The pillars are low profile due to the two competitive growth modes, vapor-liquid-solid and vapor phase epitaxy, that are active at a relatively high growth temperature of 400 ^{o}C by [16]. The nanopillars are single crystalline, 150 nm in diameter and up to 250 nm in height while the nanocones are single crystalline, 50 nm in diameter and up to 2 μm in height. Detailed structural characterizations are described in our previous paper [17].

Figure 7.2 shows Raman spectra from nanowire bundles. Since the nanowires predominantly grow perpendicular to the InP(111)B substrate, the crystal axis is oriented to the optical axis. In other words, the nanowire growth direction is parallel to the incident laser beam. All spectra from InP(111)B substrate and InP/InAs/InP nanocones exhibit two clear phonon modes of zinc blende InP structures, which can be associated with the transverse optical mode (TO) at 303.7 cm^{-1} and the longitudinal optical (LO) mode at 344.5 cm^{-1}. Since bulk InP crystal

has a zinc blende structure with T_d^2 space group, there is one Raman active mode of F_2 representation that splits into TO and LO modes in polar nature of InP and InAs [18].

Wurtzite crystal structure belongs to C_{6v}^4 space group and Raman allowed modes are A_1, E_1, E_{2H} and E_{2L}. The polarity of the vibrations causes the degenerate energies of A_1 and E_1 modes to split into LO and TO components [19]. The Raman spectra for InP nanopillars in backscattering geometry mode revealed the two phonon modes at 303.8 cm^{-1} and 343.0 cm^{-1}, which are consistent with the InP E_1(TO) and InP E_1(LO) modes for wurtzite structures, respectively. Interestingly, InP/InAs/InP nanopillars exhibit a noticeable enhancement and broadening of the LO band, which is not seen from InP bulk. The Raman spectra of InP/InAs/InP nanopillars at 303.8 cm^{-1} and 341.7 cm^{-1} are identified to be InP E_1(TO) and InP A_1(LO) modes, respectively. It is known that the LO modes are more sensitive to the Raman resonance due to the Frölich interaction [20].

The Raman peaks located at 218 cm^{-1} and 241 cm^{-1} are assigned to the first order E_1(TO) and E_1(LO) modes of zinc blende InAs [21,22]. In Fig. 7.2, Raman intensity of InAs peaks in InP/InAs/InP nanostructures is lower than that of the intensity of the InAs(111)B reference, indicating that both nanopillar and nanocones are either core-shell or InPAs alloy structures [17]. Interestingly, the red-shift of InAs E_1(LO) or InAs A_1(LO) with significant broadening are found in InP/InAs/InP nanopillars (See Fig. S1). Campbell *et al.* material size and shape can affect the Raman scattering by LO phonons [23]. Nanosized materials (i.e. sub nanometers) leads to a downshift and broadening of the LO Raman line due to the relaxation at Γ (q=0) point governed by the selection rule [24]. In particular, the Raman shift of InAs A_1(LO) confirms that WZ crystal phases are dominant in the InP/InAs/InP nanopillars [17] and results are consistent with others [25].

Besides to 1st order Raman modes, 2nd order Raman modes (2TO, TO+LO, 2LO) from nanopillars and nanocones can be detected in the region between 600 cm^{-1} and 700 cm^{-1}. This feature in the 2nd order Raman spectrum correspond to singularities in the two-phonon density of states which occur when the dispersion curves are parallel or one is horizontal, particularly at the critical points of the Brillouin zone [26]. Under the same measuring conditions, reference InP(111)B single crystal wafer doesn't show distinct 2nd order phonon vibration modes. For InP/InAs/InP nanopillars, the peaks measured at 616 cm^{-1} and 649 cm^{-1} are in good agreement with the expected 2TO(Γ) and TO(Γ)+LO(Γ) phonon modes, but the peak measured at 2LO(Γ) is slightly blue shifted from the expected position. According to the phonon-dispersion measurement [27], the longitudinal branch at point L is located only 4.5 cm^{-1} below the frequency we found at point Γ; thus, contributions from both points presumably occur in the measured 2LO peak. For InP/InAs/InP nanocones, the peaks at 649 cm^{-1} and 684 cm^{-1} are consistent with TO(Γ)+LO(Γ) and 2LO(Γ) phonon modes, but the peak of 2TO(Γ) at 619 cm^{-1} is slightly deviated from its expected position. The deviation is believed to be derived from the high aspect ratio of one-dimensional nanocones [28]. All detected Raman peaks are summarized in Table 7.I.

Material	Crystal Phase	Critical Point	Mode	Frequency	Reference
InP	ZB	Γ	E_1(TO)	304.0	13, 14
InP	ZB	X, L, Γ	A_1(LO), E_1(LO)	339, 344.5	29
InP	ZB	L	E_1(2TO)	617	13, 30
InP	ZB	Γ, X	E_1(TO+LO)	650	13, 30
InP	ZB	Γ	E_1(2LO)	682	13, 30
InAs	ZB	Γ	E_1(TO)	218	31
InAs	ZB	Γ	E_1(LO)	241	25
InAs	WZ	L	A_1(TO), E_1(TO)	225.5, 226.0	25
InAs	WZ	L	A_1(LO), E_1(LO)	246.3, 246.8	25

Table 7.I Raman vibration modes of InP and InAs nanowire in the literature

Figure 7.3 shows Raman spectra of InP/InAs/InP cones, measured by varying the substrate angle from 0 to 30 degree. As the substrate tilt angle increased, the peak intensity corresponding to TO modes for InP and InAs is noticeably enhanced. Due to crystal symmetry between zinc blende and wurtzite [32], the TO phonon is allowed in backscattering from the (110) and (111) surfaces whereas LO phonon is allowed from the (100) and (111) surfaces [33]. In Raman scattering configuration with normal incidence, the laser excitation is linearly polarized in the (111) substrate plane and the incident and backscattered vectors are orthogonal. Since nanocones and nanopillars grow along (111) surface, both TO and LO modes are allowed as shown in Fig. 7.2. However, due to the presence of substrate tilt, additional contribution from the (110) and (100) surface will be added into the TO and LO phonons, respectively. In our previous report [17], it was determined that the nanopillars have wurtzite crystal structure oriented parallel to the [0001] zone axis. The set of {1-100} planes are the side facets to the nanopillars. In fact, from the crystallographic point of view, zinc blende and wurtzite structure differ only in the stacking periodicity of the InP (or InAs) bilayers in which a bilayer consists of two stacked In and P (or As) layers; the stacking order is ABCABC for zinc blende and ABAB for wurtzite structure. Zinc blende (111) plane is parallel to wurtzite (0001) oriented planes. As the unit cell of wurzite structure along [0001] axis is double with respect to the zinc blende along the [111], the wurtzite phonon dispersion can be approximately by folding that of the zinc blende structure along the [111] direction [33]. Both nanocones and nanopillars in this experiment have hexagonal cross section with (110) sidewall facets. The reflections from (110) sidewall facets are contributed to TO mode enhancements for both InP and InAs spectra and thus LO mode is relatively suppressed.

Figure 7.4 shows an excitation power dependence of InP TO and LO peaks on Raman spectra for different substrate tilts and their relative intensity ratios I(LO, InP)/I(TO, InP). For nanopillars, a red shift (2 - 3 cm^{-1}) of the E_1(TO, InAs), A_1(LO, InAs) with the broadening effect are found when the laser intensity was increased from 5 mW to 25mW (See Fig. 7.S1). For nanocones, no substantial red shift or broadening effect are identified. The laser heating induced Raman redshift of nanopillars was much less significant under our measuring conditions. As can be seen in Fig. 7.4a and 4b, strong Raman resonance can be found from InP/InAs/InP nanopillars due to the larger effective scattering cross section respective to incident laser beam. All of the integrated Raman intensities linearly increase with respect to the excitation power that confirms no laser heating effect under this experimental condition. Due to the substrate tilt, TO reflection from both nanocones and nanopillars overwhelms LO reflection. In Fig. 7.4c, however, the relative integrated intensity ratio of I(TO, InP) over I(LO, InP) exhibits TO vibration of nanocones that is much more enhanced than that of nanopillars. The ratio of nanocones is approximately 2.3, whereas the ratio of nanopillars is close to 1.3. Tilt angle and powder dependence of Raman resonance behavior can be explained by nanowire orientation induced cross section changes between photons and lattice [34,35].

7.4 Conclusion

In conclusion, we have presented the results of Raman spectroscopy performed on self catalyzed InP/InAs/InP multi core-shell nanopillars and nanocones. The measurements are performed by varying laser power and substrate tilts under fixed backscattered geometry of micro Raman system. Contrary to two reference single crystal wafers InAs(111)B and InP(111)B, the Raman spectra of nanostructure bundles revealed unique 2nd harmonic Raman interaction

modes: E_1(2TO), E_1(LO+TO), E_1(2LO). The InP and InP/InAs/InP nanopillars showed the red shift and broadening of LO modes. In particular strong splitting between InAs E_1(TO) and InAs A_1(LO) are observed in InP/InAs/InP nanopillars. Tilting with respect to the substrate normal revealed a strong low frequency branch of the InAs LO and InP LO phonon suppression from the InP/InAs/InP nanocone bundles. The intensities of LO and TO modes are found to be dependent linearly on an excitation power but the changes in the integrated intensity ratio of TO over LO modes are almost constant.

Figures

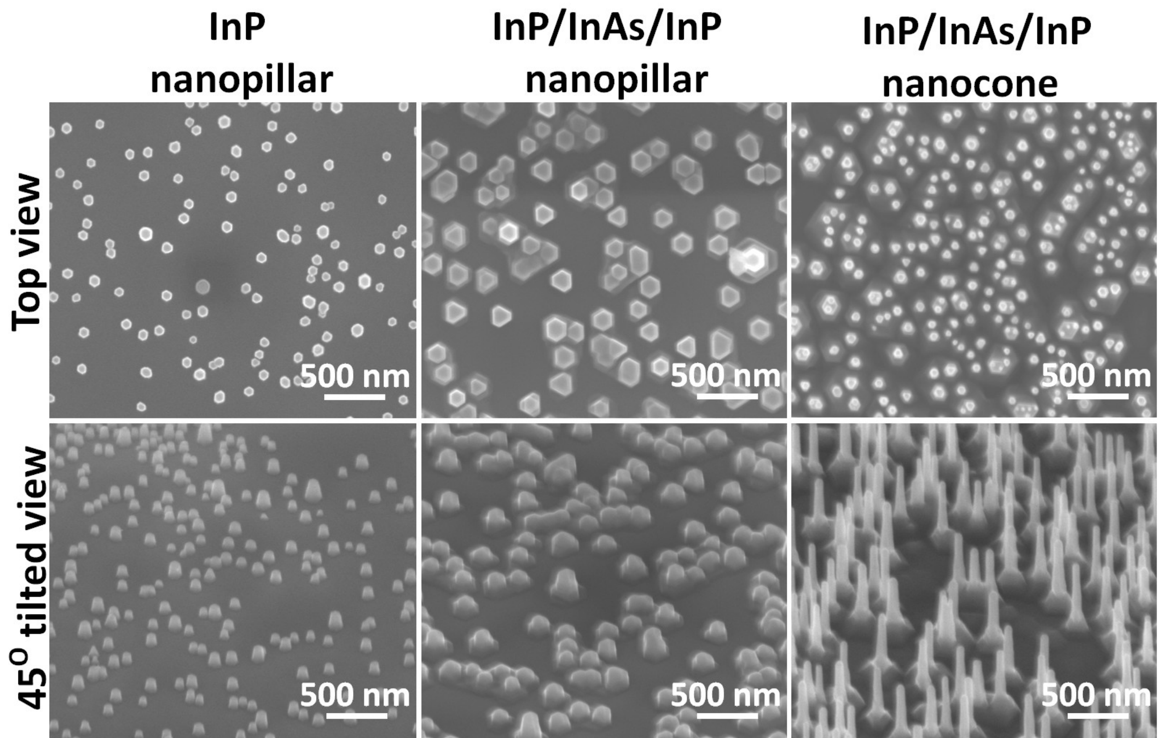

Figure 7.1 SEM images of top view (upper row) and 45 degree tilted view (lower row) of InP nanopillars, InP/InAs/InP nanopillars, and InP/InAs/InP nanocones grown on (111)B oriented InP single crystal wafer.

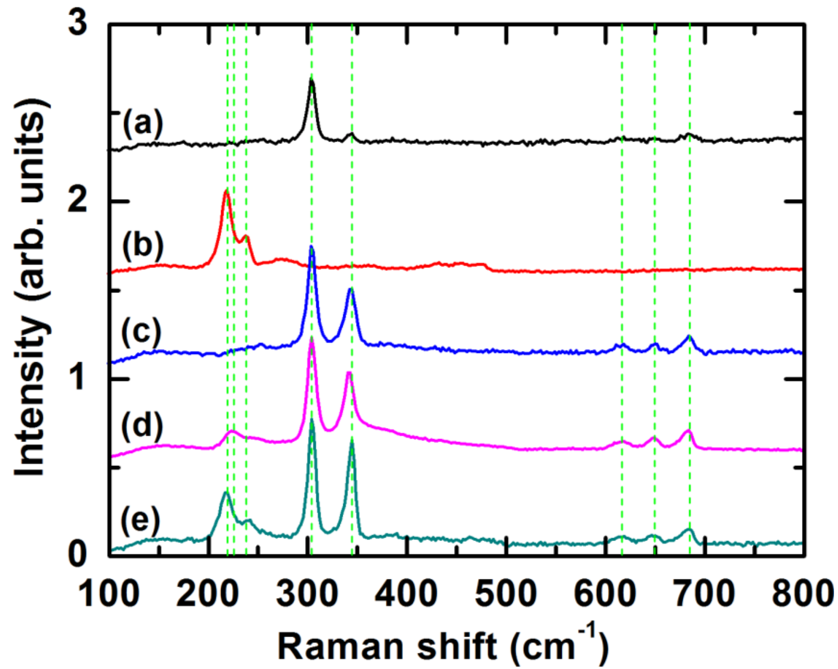

Figure 7.2 Raman spectra of (a) InP(111)B crystal, (b) InAs(111)B crystal, (c) InP nanopillar, (d) InP/InAs/InP nanopillar, and (e) InP/InAs/InP nanocones. The green dot lines are corresponded to InAs E_1(TO, ZB), InAs A_1(TO, WZ), InAs E_1(LO, ZB), InP E_1(TO, ZB), InP E_1(LO, ZB), InP E_1(2TO, ZB), InP E_1(TO+LO, ZB), and InP E_1(2LO, ZB) in sequence. ZB and WZ denote zinc blende and wurtzite crystal structure, respectively.

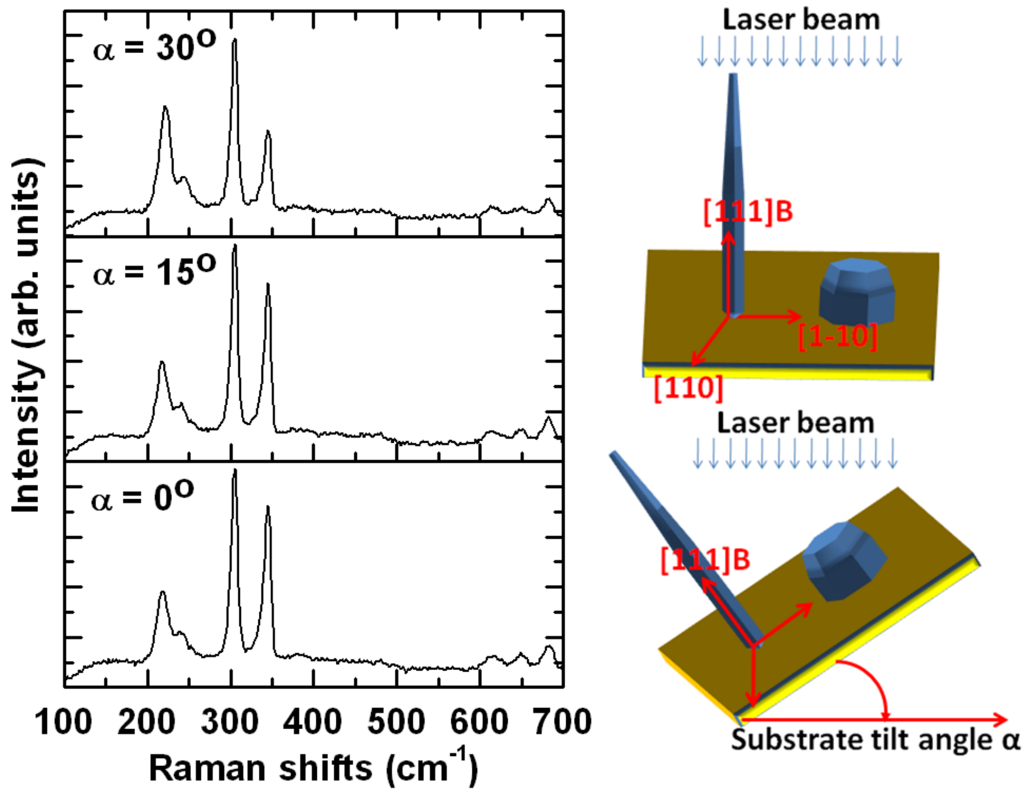

Figure 7.3 Effect of substrate tilting on Raman spectra of InP/InAs/InP nanocones.

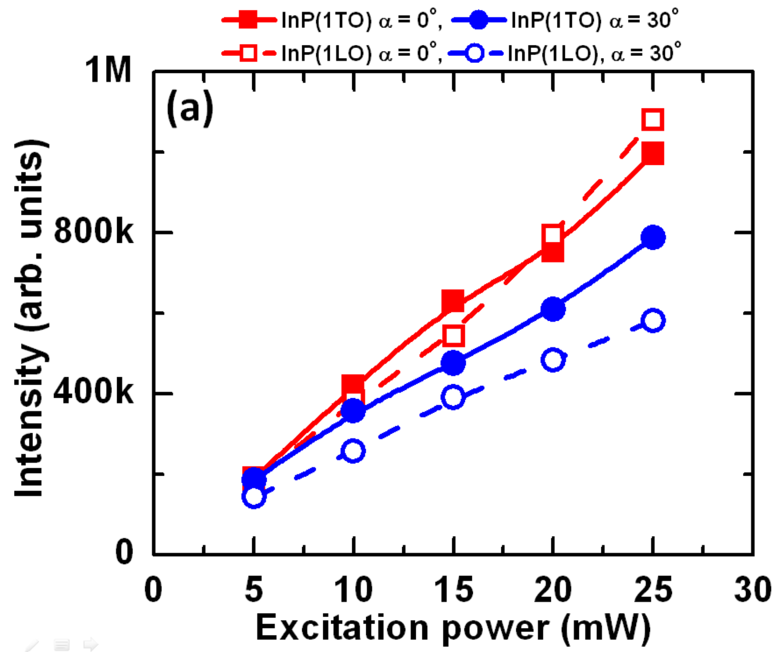
InP(1TO) α = 0°,
InP(1TO) α = 30°
InP(1LO) α = 0°,
InP(1LO), α = 30°
(a)
1M
800k
400k
0
0
5
10
15
20
25
30
Intensity (arb. units)
Excitation power (mW)

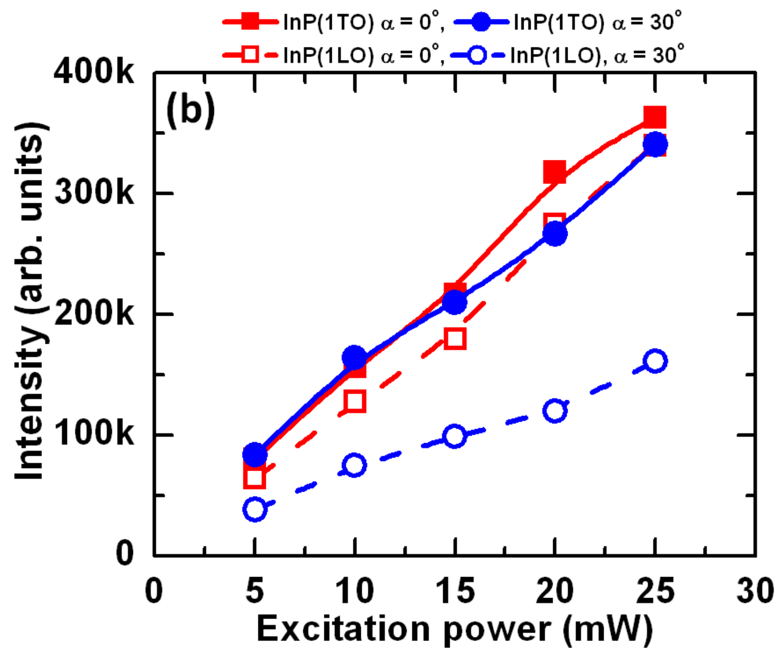
InP(1TO) α = 0°,
InP(1TO) α = 30°
InP(1LO) α = 0°,
InP(1LO), α = 30°
(b)
400k
300k
200k
100k
0
0
5
10
15
20
25
30
Intensity (arb. units)
Excitation power (mW)

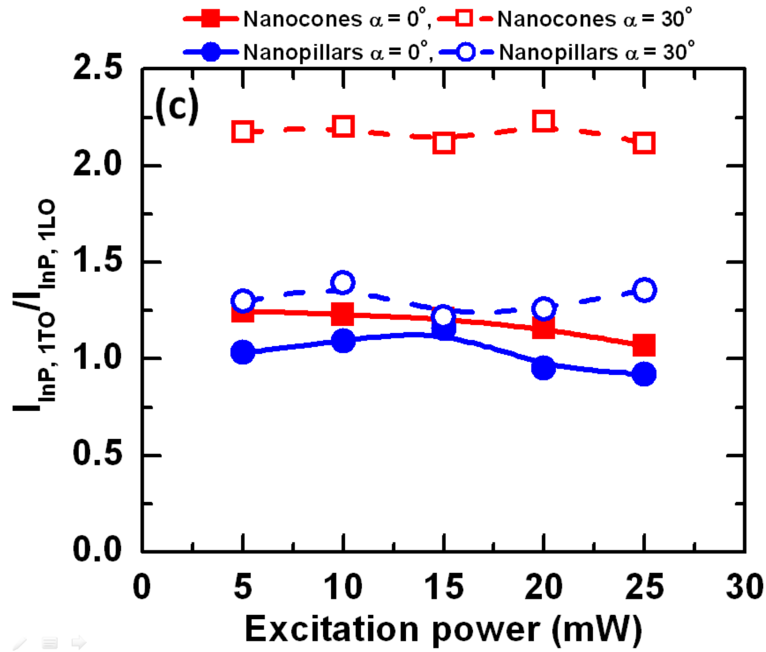

Figure 7.4 An excitation power dependence on Raman spectra of InP 1TO and InP 1LO peaks for different substrate tilts; (a) InP/InAs/InP nanopillars, (b) InP/InAs/In nanocones. (c) Integrated intensity ratio of InP 1TO over InP 1LO excitations

Supporting Information

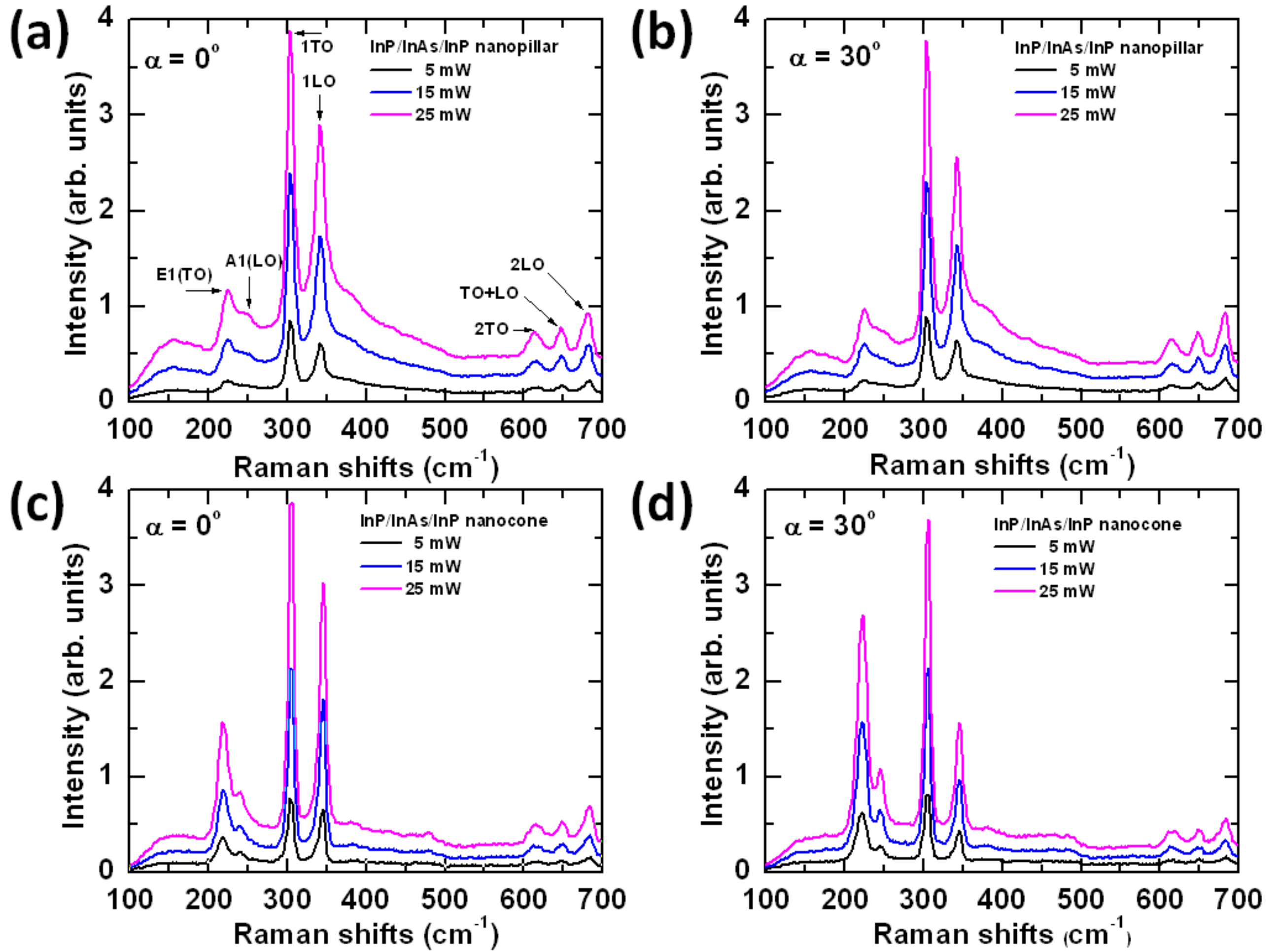

Figure 7.S1 Power spectral density dependence of (a) InP/InAs/InP nanopillar, (b) the nanopillar with 30 degree tilt, (c) InP/InAs/InP nanocone, and (d) the nanocone with 30 degree tilt.

References

[1] J. Xiang, W. Lu, Y. Wu, H. Yan, and C. M. Lieber, Nature 441, 1038 (2006).

[2] Q. Gao, H. H. Tan, H. E. Jackson, L. M. Smith, J. M. Yarrison-Rice, Jin Zou, and C. Jadadish, Semicond. Sci. Technol. 26, 014035 (2011).

[3] J. Lauhon, M. S. Gudiksen, D. Wang, and C. M. Lieber, Nature 420, 57 (2002).

[4] M. T. Björk, C. Thelander, A. E. Hansen, L. E. Jensen, M. W. Larsson, L. R. Wallenberg, and L. Samuelson, Nano Lett. 4, 1621 (2004).

[5] K. Hiruma, H. Murakoshi, and T. Katsuyama, J. Cryst. Growth 163, 226 (1996).

[6] C. Thelander, H. A. Nilsson, L. E. Jensen, and L. Samuelson, Nano Lett. 5, 635 (2005).

[7] B. Pal, K. Goto, M. Ikezawa, Y. Masumot, P. Mohan, J. Motohisa, and T. Fukui, Appl. Phys. Lett. 93, 073103 (2008).

[8] J. Wallentin, M. E. Messing, E. Trygg, L. Samuelson, K. Deppert, and M. T. Borgström, J. Cryst.. Growth 331, 8 (2011).

[9] N. Sköld, L. S. Karlsson, M. W. Larsson, M.-E. Pistol, W. Seifert, J. Trägårdh, and L. Samuelson, Nano Lett. 5, 1943 (2005).

[10] M. Liu, X. Li, H. Imrane, Y. Chen, T. Goodrich, Z. Cai, K. S. Ziemer, and J. Y. Huang, Appl. Phys. Lett. 90, 152501 (2007).

[11] P. Mohan, J. Motohisa, and T. Fukui, Appl. Phys. Lett. 88, 133105 (2006).

[12] A. Fuhrer, L. E. Fr1oberg, J. N. Pedersen, M. W. Larsson, A. Wacker, M.-E. Pistol, and L. Samuelson, Nano Lett. 7, 243 (2007).

[13] M. J. Seong, O.I. Mićić, A. J. Nozik, A. Mascarenhas, and H. M. Cheong, Appl. Phys. Lett. 82, 185 (2003).

[14] J. Chen, G. Conache, M.-E. Pistol, S. M. Gray, M. T. Borgstrom, H. Xu, H. Q. Xu, L. Samuleson, and U. Hakanson, Nano Lett. 10, 1280 (2010).

[15] A. Mooradia and G. B. Wright, Solid State Comm. 4, 431 (1966).

[16] R. Woo, L. Gao, N. Goel, M. Hudait, K.L. Wang, S. Kodambaka, and R.F. Hicks, Nano Lett. 9, 2207 (2009).

[17] V. Evoen, H. Zhou, L. Gao, M. Pozuelo, B. Liang, J. Tatebeyashi, S. Kodambaka, D. L. Huffaker, and R. F. Hicks, J. Cryst. Growth 314, 34 (2011).

[18] A. J. Lohn, T. Onishi, and N. P. Kobayashi, Nanotechnology 21, 355702 (2010).

[19] W. H. Weber and R. Merlin, Raman Scattering in Material Science (Springer: Berlin, 2000; Vol. 42).

[20] P. Y. Yu and M. Cardona, Fundamentals of Semiconductors (Springer, Berlin, New York, 2005).

[21] R. Carles, N. Saint-Cricq, J. B. Renucci, M. A. Renucci, and A. Zwick, Phys. Rev. B 22, 4804 (1980).

[22] J. Groenen, A. Mlayah, R. Carles, A. Ponchet, A. Le Corre, and S. Salaun, Appl. Phys. Lett. 69, 943 (1996)

[23] I. H. Campbell and P. M. Fauchet, Solid State Commun. 58, 739 (1986).

[24] N. Begum, M. Piccin, F. Jabeen, G. Bais, S. Rubini, F. Martelli, and A. S. Bhatti, J. Appl. Phys. 104, 104311 (2008).

[25] M. Möller, M. M. de Lima Jr., A. Cantarero, L. C. O. Dacal, J. R. Madureira, F. Iikawa, T. Chiaramonte, and M. A. Cotta, Phys. Rev. B 84, 085318 (2011).

[26] R. Trommer, H. Muller, M. Cardona, and P. Vogl, Phys. Rev. B 21, 4869 (1980).

[27] P. H. Borcherds, G. F. Alfrey, D. H. Saunderson, and A. D. B. Woods, J. Phys. C 8, 2022 (1975).

[28] G. D. Mahan, R. Gupta, Q. Xiong, C. K. Adu, and P. C. Eklund, Phys. Rev. B 68, 073402 (2003).

[29] D. Spirkoska, G. Abstreiter, and A. F. i Morral, Nanotechnology 19, 435704 (2008).

[30] L. Artus, R. Cusco, J. M. Martin, and G. Gonzalez-Diaz, Phy. Rev. B 50, 11552 (1994).

[31] X. X. Xu, K. H. Yu, W. Wei, B. Peng, S. H. Huang, Z. H. Chen, and X. S. Shen, Appl. Phys. Lett. 89, 253117 (2006).

[32] C.-Y. Yeh, Z. W. Lu, S. Froyen, and A. Zunger, Phys. Rev. B 46, 10086 (1992).

[33] I. Zardo, S. Conesa-Boj, F. Peiro, J. R. Morante, J. Arbiol, E. Uccelli, G. Abstreiter, A. F. i Morral, Phys. Rev. B 80, 245324 (2009).

[34] H. Brugger, F. Schäffler, and G. Abstreiter, Phys. Rev. Lett. 52, 141 (1984).

[35] N. Begum, M. Piccin, F. Jabeen, G. Bais, S. Rubini, F. Martelli, and A. S. Bhatti, J. Appl. Phys. 104, 104311 (2008).

CHAPTER 8

SUMMARY AND FUTURE WORK

8.1 Summary

In the Part I, We synthesized the Au-catalyzed GaAs nanowires using solid Ga and As sources on GaAs(111)B wafer. We investigated the correlation between predeposited catalyst layers and nanowire density, varying electron beam dose, patterned dot size, and inter-dot spacing. From the measurements of the fraction surface coverage of nanowire in the patterns, we found that higher electron beam doses, larger dot sizes, and shorter inter-dot spacings promote nanowire growth. Our results help identify the key electron beam lithography parameters that are desirable for large-scale, high-density, growth of nanowires.

Moreover, we showed that Raman spectra were dependent on initial pattern sizes (100 nm and 150 nm) and thickness of Au layers by varying e-beam dose. The initial catalyst thickness and pattering size were strongly related to overall nanowire morphology variations, i.e. base diameter, shapes, and densities, resulting in strong dependence of Raman spectra. The present understanding of the Raman spectroscopy on the nanowire bundles will benefit the design and development of GaAs nanoscale optoelectronic devices.

Furthermore, we studied the dependence of the SO modes of GaAS nanowire with base diameter and fill factors. The evolution of the experimental frequencies with these two parameters was analyzed in comparison with these two theoretical models based on the continuum dielectric function. The dependence of the SO frequency with fill factor was studied by evaluating the effective dielectric functions. The dipolar interaction of neighboring nanowires was found to be physical mechanism to generate the splitting and downshift of the SO modes.

The splitting and the density dependence of nanowires will provide useful information to probe the dielectric environment and the orientation of nanowires using Raman Spectroscopy.

In the Part II, we grew InP and InP/InAs core-shell nanostructures. Highly crystalline vertically aligned InP nanostructures with hexagonal cross-sections were synthesized on various substrates (i.e. InP(111)B, Si(111), Si(100)) by self-catalyzed MOCVD growth. Systematic studies of micro Raman scattering from these nanostructures at room temperature in air showed strong first order LO, TO, and SO modes. The presence of E_2^{high} mode confirmed that our nanostructures have a mixture of WZ and ZB phases or pure WZ phase. The LO modes excited by surface electrical fields were suppressed with the decreases of surface-to-volume ratio and defect density in InP nanostructures. The Raman scattering will provide further statistical insight on the quality of as-grown nanostructures (i.e. growth orientation, crystal structures, and the presence of structural defects) without destroying samples.

Finally, we showed the results of Raman spectroscopy performed on self catalyzed InP/InAs/InP multi core-shell nanopillars and nanocones. The Raman spectra of nanostructure bundles revealed unique 2nd harmonic Raman interaction modes: E_1(2TO), E_1(LO+TO), E_1(2LO). The InP and InP/InAs/InP nanopillars showed the red shift and broadening of LO modes. Strong splitting of Raman spectra between InAs E_1(TO) and InAs A_1(LO) were observed in InP/InAs/InP nanopillars. Tilting with respect to the substrate normal revealed a strong low frequency branch of the InAs LO and InP LO phonon suppression from the InP/InAs/InP nanocone bundles. The intensities of LO and TO modes were found to be dependent linearly on an excitation power but the changes in the integrated intensity ratio of TO over LO modes were almost constant.

8.2 Future Work

The In-catalyst of $InAs_xP_{1-x}$ nanowires have the promising ability to adjust the composition and the tunability of the band gap hence opens up new opportunities for controlled band gap engineering for high-speed device fabrication. The formation of In catalyzed $In_{57}As_5P_{38}$ grown on InP(111)B substrate using metalorganic vapor phase epitaxy is demonstrated. As-grown InAsP nanowires will be characterized by scanning electron microscopy, transmission electron microscopy, energy dispersive spectroscopy, X-ray photoelectron spectroscopy, and Raman spectroscopy. The composition and tunability of $InAs_xP_{1-x}$ nanowires will be studied as a function of arsenic composition in the wire.

The phenomenon of InP nanowire bridge formation under the electron beam illumination is observed using *in situ* scanning electron microscope. The model equation between mechanical energy and electrostatic energy for polar nanowires will be developed to support the experimental observation of InP nanowire bridge formation. The kinetic analysis of the phenomenon with simple mathematical modeling will provide general guidelines for the design of dense arrays of vertical nanowires.